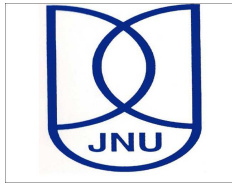


A Study of Multiple Probes of the Circumgalactic Medium

by
Priyanka Singh

This thesis is submitted for the degree of
Doctor of Philosophy



Jawaharlal Nehru University, New Delhi



Department of Astronomy and Astrophysics
Raman Research Institute

July, 2017

I dedicate this thesis to my loving grandparents Banwari Singh Medatia, Manori Medatia,
Banne Chauhan, and Santosh Chauhan.

Certificate

This is to certify that the thesis entitled 'A Study of Multiple Probes of the Circumgalactic Medium' submitted by Priyanka Singh for the award of the degree of Doctor of Philosophy of Jawaharlal Nehru University is her original work. This has not been published or submitted to any other University for any other Degree or Diploma.



Prof. Prof. Ravi Subrahmanyan
Director



Prof. Biman B. Nath
Thesis Supervisor

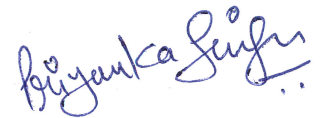
Raman Research Institute,
Bangalore 560080
INDIA

Declaration

I, Priyanka Singh, hereby declare that the work reported in this thesis titled 'A Study of Multiple Probes of the Circumgalactic Medium', is entirely original. This thesis is composed independently by me at the Raman Research Institute under the supervision of Prof. Biman B. Nath. I further declare that the subject matter presented in this thesis has not previously formed the basis for the award of any degree, diploma, membership, associateship, fellowship or any other similar title of any university or institution.

Prof. Biman B. Nath

Astronomy and Astrophysics Department,
Raman Research Institute,
Bangalore 560080
INDIA



Priyanka Singh

Acknowledgements

First, I would like to thank my supervisor Prof. Biman B. Nath for being my guiding light for last five years. You have always lead me towards the right direction and taught me what research really is. This thesis wouldn't have been possible without your encouragement and patience. I thank Prof. Subhabrata Majumdar for shaping my research career and providing a welcoming environment at TIFR. I am grateful to Prof. Alexandre Refregier for his constructive inputs and suggestions. I thank Prof. Jasjeet Singh Bagla, Prof. Joseph Silk, and Sandeep Rana for being a part my Ph.D. journey. Special thanks to Prof. Shiv K. Sethi and Prof. Biswajit Paul for answering my numerous questions. Prof. Sridhar and Prof. Udayashankar, your energy, and your stories inspired me to be more adventurous and live life to its fullest.

I thank the RRI administrative staff (Harini, Marisa, Radha, Shailaja, CSR, Krishna, and others) for providing a supportive and hassle-free atmosphere. Special thanks to Vidya. You always had a solution for my problems. I am thankful to the RRI library staff for their help and promptness.

Coming to my gang, I thank Karam, Nafisa, Sreeja, and Meera for being my support system. I am grateful to Mayuri and Sathyanna. Because of your presence, I never felt homesick. I thank Nazma for helping me personally and professionally and pampering me like a sister. Thanks to Lijo, who always had answers to my questions like, why my code isn't working? Thanks to Gayathri, Janki, Varun, Nomaan, Raju, Chaitanya, Aditi, and Sanhita for making this journey, an incredible one. I will always remember our amazing trips to different corners of the country. I enjoyed all those engaging academic as well as non-academic discussions with Saurabh, Naveen, Siddharth, Kartick, and Akash. Thank you Bhargavi for our post-dinner relaxing walks. Thanks Pinku, Pragati, Annwasha and Bidisha di for your precious friendship. Though I met you guys only once or twice a year; it used to be the best time of the year. I am thankful to Renu, Chandreyee and Nikhel for creating a homely environment for me in a foreign country, and of course for the amazing food. Special thanks to Prof. T. R. Seshadri for his valuable advice during the first year of my Ph.D.

I am grateful to my grandparents for their unconditional love and care. Preeti, Priyanshu, and Krishna, you are not only my siblings but also my minions. Thanks for co-operating with your captain. Mumma and bhaia, I have achieved this milestone because of your constant support and faith in me. Bhaia, you went against all odds so that I can pursue my dreams. Your hardships and achievements taught me that 'where there is a will, there is a way'. Mumma, I have learned from you, how to face any problem with a positive attitude, which helped me a lot in my research career. You (and your non-stop jokes) are the best.

Synopsis

The circumgalactic medium (CGM) is, arguably, the next frontier of studying the physics of galactic halo gas and holds key information about galactic evolution, energetics and cosmology. Observation and physical interpretation of the CGM, which is the gaseous medium lying between the interstellar medium (ISM) and the intergalactic medium (IGM), is poised to be one of the thrust areas of extragalactic astrophysics in coming years. During my Ph.D., I have focused on multiple potential probes of the CGM and on the prospects of constraining its properties by combining these probes. Additionally, I have studied X-ray emission from the active galactic nuclei (AGN), which plays a crucial role in extracting the X-ray signal from the CGM. I have also explored the impact of the CGM on infalling IGM as well as the outflowing gas.

Standard cosmology (Λ -CDM) predicts that when a galaxy is formed, the baryons comprise approximately 16% of the total galactic mass. However, more than half of these baryons are observationally missing, thus giving rise to the missing baryon problem. Recent detections of X-ray emission from nearby massive spiral galaxies out to large galactocentric radii and the stripping of satellites of the Milky-way suggest the presence of a significant amount of gas occupying much larger volume than the central, optically visible part of the galaxy. This gaseous medium is called the CGM or the halo gas. Additionally, simulations suggest that the feedback processes taking place near the central part of the galaxy considerably change the density and temperature profiles of the CGM. Therefore, constraining the amount, distribution and energetics of the CGM has the potential to play an important role in the missing baryon problem and in constraining the feedback processes.

Sunyaev-Zel'dovich (SZ) effect

When the low energy cosmic microwave background (CMB) photons pass through a medium containing high energy electrons, the photons gain energy from the electrons. This process distorts the black-body spectrum of the CMB and is termed the SZ effect. If the energy of the intervening medium is primarily due to its temperature, the SZ effect is called thermal

SZ (tSZ) effect, whereas, if the energy of the intervening medium mainly comes from its bulk motion, the resulting distortion is called kinetic SZ (kSZ) effect. The SZ effect is well studied in the case of galaxy clusters, which are the largest and easiest to observe, followed by the studies of galaxy groups. We have computed tSZ and kSZ angular power spectrum for the CGM and examined the possibility of constraining its distribution and energetics with current and future SZ surveys. We have shown that the galaxies with a halo mass more than $10^{12}M_{\odot}$ give a significant contribution to the SZ signal. The kSZ power spectrum is larger than the tSZ power spectrum from the CGM and it can even be larger than the ICM SZ power spectrum at large multipoles ($l > 10^4$).

Cross-correlation of multiple probes of the CGM

The other signature for the CGM could be X-rays because the CGM in massive galaxies remains mostly at a high temperature ($T > 10^6$ K) thus emitting in X-rays. However, low density of the CGM means that detecting the CGM of an individual galaxy through the SZ effect or X-ray observations is difficult. Fortunately, the detectability of these signals can be increased by cross-correlating it with some other strong signal. We chose to cross-correlate these signals with the distribution of galaxies. We have forecasted the detectability of tSZ-galaxy distribution and X-ray-galaxy distribution cross-correlation signals by the South Pole Telescope (SPT), extended Röntgen Survey with an Imaging Telescope Array (eROSITA) and Dark Energy Survey (DES)/Large Synoptic Survey Telescope (LSST), which look at the Universe in radio, X-ray and optical wavelengths respectively. We have found that these cross-correlation signals for the CGM can be detected with sufficient signal-to-noise ratio (i.e. $\text{SNR} \sim 3-9$) using the above survey combinations.

X-ray emission is more sensitive to the CGM density profile ($\propto n_e^2$) than the tSZ effect ($\propto n_e$) and this difference is manifested in the cross power spectrum. To show this effect, we modelled the density profile as $n_e(r) \propto [1 + (r/R_s)^{\gamma_{\text{gas}}}]^{-1}$, where R_s is the scale radius. Increasing the value of γ_{gas} , i.e. steepening the density profile results in increased signal at large l in the case of tSZ-galaxy cross power spectrum. The variation in the density profile leaves strong imprints on the X-ray-galaxy cross power spectrum even at low l values. We have used the Fisher matrix analysis to estimate the constraints on the CGM gas fraction, its temperature and the value of γ_{gas} . We found that these parameters can be constrained to better than a few percent with SPT-DES and eROSITA-DES/LSST survey combinations.

Outflows, infall and the CGM

The presence of galactic-scale winds due to feedback processes like supernovae (SNe) explosions is evident in both simulations and observations. These winds are responsible for carrying metals from the centremost part of the galaxy to the IGM. Therefore, it is important to understand the processes affecting the propagation of these outflows to understand the evolution of the galaxy as well as the metal enrichment history of the universe. We have studied the relative suppression of the outflowing gas due to the presence of infalling gas from the IGM and the CGM. Together, the hot CGM and infall give a mass limit separating the galaxies with and without suppressed outflows which is close to $\sim 5 \times 10^{11} - 10^{12} M_{\odot}$ (depending on the redshift) with the hot CGM being more effective than the infall at $z < 3.5$. We have shown that at low redshifts ($z < 1 - 2$), galaxies with suppressed outflows constitute a large fraction (40-50%) of the total galaxy population.

The X-ray AGNs

Our work on cross-correlating X-ray emission from the CGM with the distribution of the galaxies showed that it is a powerful tracer of the underlying gas distribution. However, AGNs dominate the X-ray sky and it is essential to model the unresolved AGN emission to get the X-ray signal from the CGM. Therefore, we looked into the detailed X-ray AGN modelling which required dealing with the AGN X-ray luminosity function and their halo occupation distribution (HOD) model. We have verified that these two inputs are in agreement with the AGN observations as well as with each other in a wide range of redshift (especially at $z \sim 0.5 - 3.5$). We have computed the auto power spectrum of the AGNs expected to be resolved by eROSITA and well as the unresolved AGN background and X-ray-lensing cross power spectrum for eROSITA-LSST survey combination. The present uncertainties in the HOD model parameters are large. This is mainly due to the small sky coverage of currently available X-ray telescopes. This situation is expected to improve with the launch of eROSITA. Therefore, we forecasted the ability of eROSITA (X-ray auto power spectrum) and eROSITA-LSST combination (X-ray-lensing cross power spectrum) to constrain the HOD model parameters. We have shown that these uncertainties can be reduced by an order of magnitude by including lensing in the analysis.

Conclusions

There is an enormous amount of effort going on in the determination of the properties of the CGM as it is linked to the galaxy physics as well as cosmology. In my thesis, I have focused on the hot phase of the CGM. The SZ effect and the X-ray emission are two prime signatures of the hot gas. I started my work by estimating the tSZ and kSZ power spectra for the hot CGM. The weak nature of the signal led us to explore the potential of cross-correlation of large sky surveys. I forecasted the detectability of tSZ-galaxy cross power spectrum with SPT-DES survey combination. I also forecasted the constraints on the CGM properties that this survey combination can impose. I then computed the X-ray-galaxy cross power spectrum and forecasted the detectability as well as the constraints on CGM properties keeping eROSITA-DES/LSST in mind. I found that the X-ray-galaxy cross power spectrum can put stringent constraints on gas properties. However, the X-ray sky is dominated by AGNs. Therefore, I built a halo model for the AGNs. I computed the X-ray auto power spectrum for resolved as well as the unresolved AGNs. I also included the weak lensing signal in the cross-correlation analysis to improve the constraints on the AGN halo model. In addition, I explored the effect of the presence of CGM on outflowing as well as infalling gas. I am certain that combining all these probes, with the availability of data from surveys such as SPT, eROSITA, DES etc, will enhance our understanding of the CGM.

List of Publications

- “CMB distortion from circumgalactic gas”
Singh, P., Nath, B. B., Majumdar, S., Silk, J. 2015, MNRAS[†], 448, 2384
- “Probing the circumgalactic baryons through cross-correlations”
Singh, P., Majumdar, S., Nath, B. B., Refregier, A., Silk, J. 2016, MNRAS, 456, 1495
- “Suppression of galactic outflows by cosmological infall and circumgalactic medium”
Singh, P., Rana, S., Bagla, J. S., Nath, B. B. 2016, MNRAS, 459, 2
- “Constraining the X-ray AGN halo occupation distribution: implications for eROSITA”
Singh, P., Refregier, A., Majumdar, S., Nath, B. B. 2017, MNRAS, 466, 3961

[†]MNRAS : Monthly Notices of Royal Astronomical Society

Table of contents

List of figures	xxi
List of tables	xxiii
1 Introduction	1
1.1 What is circumgalactic medium?	1
1.2 Theoretical background	1
1.3 Link to the missing baryon problem	3
1.3.1 Baryon census at high redshifts	3
1.3.2 Baryon census at low redshifts	5
1.4 Link to the feedback processes	8
1.5 Different phases of the CGM	11
1.5.1 Hot CGM	11
1.5.2 Warm CGM	14
1.5.3 Cool CGM	15
1.6 Motivation of the thesis	16
1.6.1 Detection of tSZ/kSZ effect from CGM	16
1.6.2 Advantage of cross-correlations	16
1.6.3 X-ray emission from the CGM	16
1.6.4 Can we quantify the role of the CGM in galaxy evolution?	17
1.6.5 The AGN foreground	17
1.7 Plan of the thesis	18
2 CMB distortion from circumgalactic gas	21
2.1 Introduction	23
2.2 SZ distortion from hot galactic halo gas	24
2.2.1 tSZ effect	24
2.2.2 kSZ effect	25

2.3	The SZ Power Spectrum	26
2.3.1	tSZ C_ℓ	26
2.3.2	Mass and redshift range	27
2.3.3	kSZ C_ℓ	29
2.3.4	SZ from CGM -vs- SZ from ICM	31
2.3.5	Redshift distribution of the angular power spectrum	31
2.3.6	Mass distribution	32
2.3.7	Dependence of SZ angular power spectrum on cosmological parameters	33
2.4	Detectability in future surveys and constraining gas physics	34
2.4.1	Integrated Comptonization parameter \tilde{Y}_{500}	34
2.4.2	Signal to noise ratio in future surveys	35
2.5	Forecasting	38
2.5.1	Formalism	38
2.5.2	Results	40
2.6	SZ effect from warm CGM	45
2.7	Conclusions	47
3	Probing the circumgalactic baryons through cross-correlations	49
3.1	Introduction	51
3.2	SZ distortion from hot galactic halo gas	52
3.2.1	tSZ effect	53
3.3	SZ-galaxy cross-correlation	54
3.3.1	The angular power spectrum for tSZ	54
3.3.2	The angular power spectrum for the distribution of galaxies	55
3.3.3	SZ-galaxy cross-correlation power spectrum	56
3.3.4	CGM density profile and the cross-power spectrum	56
3.3.5	Detectability of the SZ-galaxy cross-correlation signal	59
3.4	X-ray-galaxy cross-correlation	61
3.4.1	The X-ray angular power spectrum	63
3.4.2	Detectability of the X-ray-galaxy cross-correlation signal	65
3.4.3	X-ray survey	66
3.5	X-ray-SZ cross-correlation	67
3.6	Forecasting of CGM constraints	69
3.6.1	Results	70
3.7	Probing the energetics of the CGM	73
3.8	Conclusions	75

4	Suppression of galactic outflows by cosmological infall and circumgalactic medium	77
4.1	Introduction	79
4.2	Formalism	81
4.2.1	Outflow velocity	81
4.2.2	Infall velocity	82
4.3	Suppression of outflows	83
4.3.1	Suppression by infall	83
4.3.2	Suppression by hot CGM	85
4.3.3	Relative importance of infall versus hot CGM in suppressing outflows	87
4.4	Fraction of galaxies affected by the suppression of outflows	88
4.5	Caveats	90
4.6	Conclusions	91
5	Constraining the X-ray AGN halo occupation distribution: implications for eROSITA	93
5.1	Introduction	95
5.2	Auto-correlation power spectrum of the resolved AGNs	97
5.2.1	Poisson term	98
5.2.2	AGN XLF	98
5.2.3	Clustering term	100
5.2.4	Redshift and mass dependence	105
5.3	Forecast for constraining HOD parameter using auto-correlation power spectrum	107
5.4	Cross-correlating X-ray AGN with lensing	109
5.4.1	X-ray-lensing cross-correlation power spectrum	110
5.4.2	Forecast using the cross-correlation power spectrum	112
5.5	Unresolved AGNs	113
5.5.1	Flux weighted angular auto-correlation power spectrum	114
5.5.2	Redshift and mass dependence	116
5.6	Conclusions	116
6	Conclusion	119
	References	125

List of figures

1.1	Schematic diagram of a spiral galaxy surrounded by the CGM.	2
1.2	Baryon census from Shull, Danforth & Tilton (2014).	8
1.3	Galaxy luminosity function	10
2.1	The ratio of cooling time to destruction time-scales	28
2.2	Angular power spectrum of CMBR at 150 GHz	29
2.3	Angular power spectrum of CMBR at 150 GHz: comparison with observations	32
2.4	Redshift distribution of tSZ and kSZ effects	33
2.5	Moments of the mass function for tSZ and kSZ	34
2.6	Dependence of SZ angular power spectrum on σ_8 , Ω_M , n_s and h	35
2.7	\tilde{Y}_{500} as a function of halo mass for $f_{\text{gas}} = 0.11$ and $f_{\text{gas}} = 0.05$	36
2.8	The cumulative signal to noise ratio (SNR)	38
2.9	1- σ contours for gas physics parameters when α_{gas} is fixed	39
2.10	Fisher matrix analysis	42
2.11	Impact on parameter constraints due to any unknown evolution of the gas fraction with redshift	43
2.12	1- σ contours for gas physics parameters	46
3.1	The cross power spectra of the SZ effect	57
3.2	l_{max} as a function of the mean halo mass for redshift bins	58
3.3	The cross power spectra of the SZ effect for different gas density profiles . .	59
3.4	Contours of the cumulative signal-to-noise (SNR) for SZ-galaxy distribution	62
3.5	The cross power spectra of the X-ray emission from the CGM	64
3.6	The X-ray-galaxy cross power spectra for different gas density profiles . . .	65
3.7	Contours of the cumulative signal to noise for X-ray-galaxy cross power spectrum	67
3.8	SZ-X-ray power spectrum	68
3.9	68% confidence limit contours for f_{gas} , f_{Temp} and α_{gas}	72

3.10	68% confidence limit contours for f_{gas} and γ_{gas}	75
4.1	Wind terminal velocity	82
4.2	Ratio of outflow velocity to $3 \times$ circular speed of the halo	84
4.3	Ratio of net outflow velocity with and without the infall	85
4.4	Comparison between mass limits predictions, relevant to the suppression of galactic outflows	86
4.5	The ratio of mass in haloes hosting unsuppressed outflows to the total mass in all collapsed structures	89
5.1	The observed differential number counts of X-ray AGNs against the prediction of the XLF	100
5.2	The differential redshift and luminosity distribution of the AGNs expected to be resolved by eRASS	101
5.3	The normalized radial distribution of the X-ray AGNs compared with the NFW profile	103
5.4	Comparison between the X-ray AGN number density as predicted by AGN XLF and HOD	104
5.5	Total power spectrum due to the resolved AGNs	105
5.6	Redshift dependence of the resolved AGN auto-correlation power spectrum	106
5.7	Mass dependence of the resolved AGN auto-correlation power spectrum . .	107
5.8	The cross-correlation power spectrum of soft X-ray emission from the AGNs and weak lensing	112
5.9	The forecasted 68% confidence limit contours for the redshift evolution parameters of the HOD model	114
5.10	Same as Figure 5.5 but for the unresolved AGNs.	115
5.11	Same as Figure 5.6 but for the unresolved AGNs.	115
5.12	Same as Figure 5.7 but for the unresolved AGNs.	117

List of tables

2.1	Fiducial values and priors on the parameters	37
2.2	Error on parameters for different surveys and Prior cases with fixed α_{gas} . . .	39
2.3	Error on parameters for different surveys and Prior cases	41
3.1	Specifications of surveys	60
3.2	Fiducial values and priors on the parameters	69
3.3	Error on parameters for different scenarios for SPT-DES combination	70
3.4	Error on parameters for different scenarios for eROSITA-DES combination	70
4.1	The table lists the simulations used in this chapter	83
5.1	LADE model parameters.	99
5.2	Parameters of MOF.	103
5.3	Forecasted constraints on the HOD parameters with eROSITA and eROSITA- LSST combination.	113

Chapter 1

Introduction

1.1 What is circumgalactic medium?

There are two main components of a galaxy: dark matter and baryons. Unlike dark matter, baryons undergo shock heating, cool, condense to the central part of the galaxy and form stars, thus giving a galaxy its spectacular optical appearance. However, a large fraction of these baryons remain too hot to condense and form stars. This gas stays in a hot, diffuse gaseous form and is commonly referred to as the circumgalactic medium (CGM). The CGM surrounds the central, optically visible part of the galaxy and extends up to the virial radius of the galaxy. Figure 1.1 shows a schematic diagram of a spiral galaxy surrounded by the CGM.

The CGM is, arguably, the next frontier of studying the physics of galactic halo gas and holds key information about galactic evolution, energetics and cosmology. Observations and physical interpretations of the CGM, which lies between the metal rich interstellar medium (ISM) and the almost pristine intergalactic medium (IGM), is poised to be one of the thrust areas of extragalactic astrophysics in coming years.

1.2 Theoretical background

The gas cooling time-scale (t_{cool}) is one of the most important parameters in galaxy evolution (Rees & Ostriker 1977; Silk 1977; White & Rees 1978; White & Frenk 1991; Kereš et al. 2005 etc.). Nearly, four decades ago, Rees & Ostriker (1977) and Silk (1977) predicted the existence of a hot gaseous environment in massive galaxies ($M_{\text{h}} > 10^{11.5} M_{\odot}$) based on the comparison of t_{cool} and the gravitational collapse time-scale (t_{grav}). They showed that t_{cool} in massive galaxies is larger than t_{grav} i.e. the thermal pressure of the gas is sufficient to

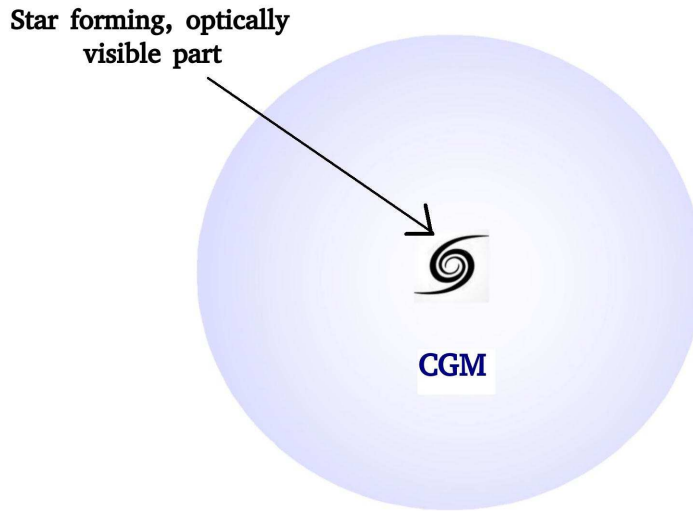


Fig. 1.1 Schematic diagram of a spiral galaxy surrounded by the CGM.

support it against gravitational collapse thus maintaining a hot gaseous environment in the galactic haloes.

Numerical simulations have also supported the presence of such a circumgalactic environment and the potential of the CGM to contain a substantial amount of these missing baryons. Fukugita & Peebles (2006) showed that assuming the halo contains half of the baryons, they could reproduce the observation of galaxy-mass cross-correlation. Birnboim & Dekel (2003) used numerical simulations to check the stability of the virial shocks, responsible for the formation of a hot CGM. They found that haloes with mass $M_h < 10^{11} M_\odot$ never form a stable virial shock even with the extreme assumption that the gas metallicity is zero. Using the gas metallicity as low as $Z \sim 0.05$, this mass estimate changes to $\sim 7 \times 10^{11} M_\odot$. They also studied the impact of the presence of feedback on the stability of the virial shock. This mass limit divides the galaxy population into two categories. The galaxies below this mass limit show the existence of cold flows due to the small gas cooling time-scale. The galaxies above this mass limit retain the CGM as a hot gaseous medium due to the large gas cooling time-scale. Later, Dekel & Birnboim (2006) verified that the above scenario is consistent with the observed bimodality of galaxy population into red and blue sequences.

1.3 Link to the missing baryon problem

At the present epoch, there are two main components of the total energy density in the Universe: dark energy and matter (represented by Ω_Λ and Ω_M *, respectively). According to *Planck* observations (Planck Collaboration et al., 2015a), these numbers are close to $\Omega_\Lambda \sim 0.73$ and $\Omega_M \sim 0.27$, at $z=0$. There is another component of the total energy density of Universe, namely radiation (photons and neutrinos) density, which is negligible at the present epoch. The matter and radiation densities vary as $(1+z)^3$ and $(1+z)^4$, respectively, i.e. these densities are decreasing functions of the redshift, whereas the dark energy density is independent of redshift. Consequently, at high redshifts ($z > 0.3$), the Universe was matter dominated whereas at even higher redshifts ($z > 3000$), the Universe was radiation dominated. The matter component is further divided into dark matter and baryons. The ratio of baryons and total matter is denoted by $f_B (\equiv \Omega_B/\Omega_M)$ and is termed as the cosmic baryon fraction. This number is close to 0.16 as determined by Planck observations (Planck Collaboration et al., 2015a).

This value of f_B corresponds to $\Omega_B \sim 0.022 h^2$ (which corresponds to $\Omega_B \sim 0.044$ for *Planck* observations). Observers have worked hard for many decades for a complete census of baryons. Different epochs have been explored using different techniques to find these baryons. These techniques are described in detail below.

1.3.1 Baryon census at high redshifts

Big bang nucleosynthesis

The first heavier (than hydrogen) elements formed during the initial moments of our Universe were He^4 , deuterium, He^3 and Li^7 . The other stable heavier elements such as carbon were not formed due to the fact that the densities and temperatures required for the formation of these elements are available only in stellar processes (stellar cores and SNe explosions). Among these heavy elements, the first one to be formed was deuterium as almost all the neutrons combined with protons to form deuterium. It was followed by this deuterium fusing to form He^4 , resulting in an overall fraction of He^4 close to 25%, which has been verified by observations. Only a small fraction of deuterium survives this process. Later, as the temperature in the Universe dropped, other elements were formed. All these elements can be fused in stars to form heavier elements. Among these, deuterium is the only element which cannot be formed in the stars. Also, the abundance of deuterium is very sensitive to the

*The density parameter of the i^{th} component is defined as, $\Omega_i \equiv \frac{\rho_i}{\rho_c}$, where ρ_c is the critical density given by, $\rho_c = \frac{3H_0^2}{8\pi G}$. Here H_0 is Hubble constant and G is the gravitational constant.

baryon density in the early Universe. Therefore, it is one of the most unbiased tracers of the baryon density at high redshifts. The cosmic abundances of deuterium as well as other primordial elements, estimated through the observation of highly metal poor gas in the spectra of background quasars tightly constrain the baryon density and it is close to the predicted cosmic baryon fraction (see Copi, Schramm & Turner 1995 and references therein).

Cosmic microwave background (CMB)

Visible photons are formed inside stars. Yet, these photons constitute a negligible fraction of the total number of photons present in the Universe. The CMB contains nearly all the photons. During the early moments of our Universe, the temperature and density were so high that photons continuously interacted with matter. With the continuous expansion of the Universe, the temperature and density kept decreasing with time. At a particular epoch, known as the epoch of recombination, radiation decoupled from matter, forming the CMB radiation. The CMB radiation then moved through space, mostly not interacting with matter. One cannot observe the CMB beyond the recombination epoch as the photons were continuously being scattered by matter, thus smearing out the radiation. Formation of the CMB was accompanied by their last interaction with matter, thus forming the last scattering surface. Therefore, the CMB encodes the conditions of the Universe at last scattering.

The CMB is highly uniform, isotropic and the best black body ever observed. However, there are small anisotropies present in the CMB spectrum at small scales due to various processes before the last scattering (primary anisotropy) as well as due to those during the passage of light from the last scattering surface to us (secondary anisotropy). These temperature fluctuations are close to one part in 10^5 . One of the main causes of primary anisotropy are the gravitational fluctuations which began even before the last scattering surface. These fluctuations are the seeds of structures (galaxies, clusters etc.) that we see today. The fluctuations at the last scattering surface are frozen in the CMB anisotropy and they are being probed through the acoustic oscillation peaks present in the CMB angular power spectrum. The amplitudes of these peaks are extremely sensitive to the baryon density at recombination. Komatsu et al. (2011) showed that the acoustic peaks probed through seven-year data from WMAP survey are in agreement with the cosmic baryon fraction, with $\Omega_B \sim 0.045$, providing additional support to the standard Λ -CDM cosmology.

Lyman α forest

Most of the baryons ($\sim 75\%$) are in the form of hydrogen. After recombination, these hydrogen atoms remain in the neutral state for a long time ($10 < z < 1100$). This era in cosmology

is referred to as the dark age as there was no source of radiation other than the CMB radiation. The formation of stars and galaxies began the process of reionizing the hydrogen. The ionization potential of hydrogen is 13.6 eV. Photons with energy less than 13.6 eV can cause bound-bound transitions in the hydrogen atoms. Lyman α transition ($n=1$ to $n=2$), which corresponds to the wavelength $\lambda \sim 1215 \text{ \AA}$, dominates these transitions. During the reionization era, the passage of light from a background quasar through a neutral hydrogen cloud results in the Lyman α absorption feature in the quasar spectrum. An absorber lying at a smaller redshift than the quasar, absorbs a photon with rest-frame wavelength $< 1215 \text{ \AA}$, as it is redshifted to $\sim 1215 \text{ \AA}$ in the rest-frame of the absorber. The presence of multiple absorbing systems at different redshifts along a quasar line of sight results in a series of such lines in the quasar spectrum, known as the Lyman α forest. Gunn & Peterson (1965) expressed the optical depth, $\tau(z)$, at a given redshift as a function of the baryon density at that redshift. They used this expression to constrain the fraction of neutral hydrogen, f_{HI} , as this quantity was poorly understood compared to Ω_{B} at the time. With the improved knowledge of ionizing radiation field (from simulations as well as observations) and the temperature history of the IGM, the same formalism can be used to constrain Ω_{B} . Weinberg et al. (1997), using Lyman α forest measurements, placed a lower limit on Ω_{B} , according to which the high redshift ($z \sim 2 - 4$) IGM contains $\sim 80\%$ of the total baryonic mass predicted by standard cosmology, with the rest being in stars and galaxies.

1.3.2 Baryon census at low redshifts

In the hierarchical scenario of structure formation, small structures (galaxies, groups) form first, followed by the formation of larger structures (clusters, superclusters). With decreasing redshift, the amount of matter in the collapsed structures increase as the galaxies accrete matter from the ionized plasma around it and in this way baryons are re-distributed in the Universe. However, it has been difficult to observe low redshift baryons, even with the most advanced telescopes. This leads to the famous missing baryon problem. This problem is further divided into the following two parts.

Galactic missing baryon problem

When a galaxy is formed, the total amount of baryons in it is expected to be f_{B} times the total mass of the galaxy. Yet, galaxies seem to have less than half of these baryons. This represents the galactic missing baryon problem. The fraction of baryons in galaxy clusters appears to be close to the cosmic baryon fraction. As the halo mass decreases, the amount of missing baryons increases. Klypin, Zhao & Somerville (2002) showed that at the maximum,

25% to 50% of the cosmic baryon fraction can be accommodated in the central disk and bulge component of the MilkyWay and Andromeda galaxies to explain the observations. Bell et al. (2003) used the SDSS and 2MASS surveys to determine the stellar and gaseous component of galaxies in the Universe. They found that, together, the mass present in the cold gas and stars can account only for $8_{-5}^{+4}\%$ of the expected amount of baryons. Flynn et al. (2006) showed that the observed baryons in the MilkyWay represent only (approximately) half of the total expected mass in baryons.

The missing baryons are either lying unobserved in the galactic halo or they have been expelled through strong galactic winds. Davé (2009) explored the second possibility using numerical simulations. This work predicted that such outflows can potentially throw half the baryons out of MilkyWay type galaxies. It showed that lower mass galaxies can severely lose much more baryons, whereas, with the increase of galactic mass, the depletion of baryons decreases.

On the other hand, theoretical calculation as well as numerical simulations predicted the existence of the hot gaseous medium retaining a large amount of baryons in the halo (see Section 1.2). White & Frenk (1991) showed that such a hot corona, if present in the galactic halo, should be easily visible in its soft X-ray emission, assuming that the gas follows the dark matter distribution. However, the predicted emission remained undetected in X-ray observations. Crain et al. (2010) used hydrodynamical simulations to show that the gas distribution is less concentrated than the dark matter distribution, resulting in a much lower X-ray emission. They included SNe driven feedback causing a flatter distribution of the gas. Enormous effort has been spent into nailing down these missing baryons. Recently, the X-ray observations of a few nearby galaxies indicated the presence of a significant amount of gas locked in the CGM (Anderson & Bregman, 2011; Dai et al., 2012; Anderson, Bregman & Dai, 2013; Bogdán et al., 2013b,a; Walker, Bagchi & Fabian, 2015). Additionally, the ram pressure stripping of satellite galaxies present in the MilkyWay halo supports the presence of a huge gas reservoir, with electron density $\sim 10^{-3} - 10^{-4} \text{ cm}^{-3}$ at large galacto-centric radii ($\sim 100 \text{ kpc}$) (Grcevich & Putman, 2009; Putman, Peek & Joung, 2012; Gatto et al., 2013). These observations indicate towards the potential role of the CGM in the missing baryon problem.

Missing baryons on global scales

Even when one takes into account the CGM as well as the uncollapsed material in the IGM, the observed fraction of baryons appears to fall short of the cosmic baryon fraction. This leads to the second part of the missing baryon problem, the deficit of baryons on global scales. It is difficult to observe Lyman α absorption at low redshifts as it moves into the UV

range below a redshift of 2. It is difficult to observe it in emission due to its low density. Even in galaxies, where the gas density and temperature are relatively high, the baryons seem to be missing.

This deficit of baryons at low redshifts has been known for a long time. Fukugita, Hogan & Peebles (1998) carried out a detailed analysis of baryon content of various components of the Universe at different redshifts. They showed that most of the baryons exist in ionized plasma in groups of galaxies, at $z=0$. They predicted a total baryon density, $\Omega_B \sim 0.021$, i.e. half of the expected value. However, the uncertainty in their prediction was large with the maximum allowed value of Ω_B close to the cosmic baryon fraction. This uncertainty in the baryonic mass at low redshifts is further complicated by processes such as galaxy formation, feedback, radiative background from various sources etc. A large variety of N-body cosmological simulations are in broad agreement with each other, and they predict that collapsed structures hold 10-20% of the cosmic baryon fraction, whereas the rest is expected to lie in the ionized IGM at low z (Cen & Ostriker, 1999; Davé et al., 2001; Smith et al., 2011; Durier & de Freitas Pacheco, 2011; Haider et al., 2016). Studies carried out using many galaxy surveys have indicated that collapsed structures (galaxies, groups, clusters) contain approximately 10% of the total (expected) baryons (Salucci & Persic, 1999; Fukugita & Peebles, 2004; Read & Trentham, 2005). The fraction of baryons in IGM is close to 40-50%. Shull (2003) found that most of the IGM stays in warm-hot phase traced by Lyman α and OVI absorbers, rather than in a cool photoionized phase. Note that, Lyman α absorption is not a direct tracer of the ionized hydrogen. It gives the neutral hydrogen fraction which is then converted to the ionization fraction.

In Figure 1.2, we show the pie-chart taken from more recent work on the baryon census at low z by Shull, Smith & Danforth (2012). They have shown that the IGM contains approximately 60% of the total baryonic mass. This includes the photoionized IGM ($\sim 28\%$), shocked warm-hot IGM traced by Lyman α ($\sim 14\%$) and OVI ($\sim 17\%$). Earlier works (Danforth & Shull, 2005; Tripp et al., 2008) found a lower limit on OVI traced IGM $\sim 5-7\%$, which is half the amount estimated in Shull, Smith & Danforth (2012). This difference is primarily due to a higher value of metallicity assumed in previous works. The amount of hot IGM traced by OVII and OVIII is still debated (Nicastro et al., 2005a,b; Kaastra et al., 2006; Rasmussen et al., 2007; Yao et al., 2012). The lowest fraction of baryons exist in the cold gas ($\sim 1.7\%$) followed by the ICM, which is predicted to contain $\sim 4\%$ of the cosmic baryon fraction. Coming to the galactic baryonic component, Shull, Smith & Danforth (2012) predicted that galaxies contain $\sim 12\%$ baryons, with 7% in stars and ISM, and 5% in the CGM. Even after counting the baryons in all these systems, Shull, Smith & Danforth (2012) were not able to find $\sim 29\%$ of the baryons i.e. one third of the baryons are still missing. The

uncertainties on these missing baryons is about 13%, which is rather large. Also, there are large uncertainties in the baryonic amount of different components of the Universe as shown in the pie-chart. The largest source of error ($\sim 77\%$) on these measurements is the uncertainties in the understanding of the ionizing radiation field as well as the size of the absorbing systems (since most of these observations rely on the absorption spectroscopy techniques). The only solution to this issue is the availability of better measurements with improved UV absorption line spectroscopy.

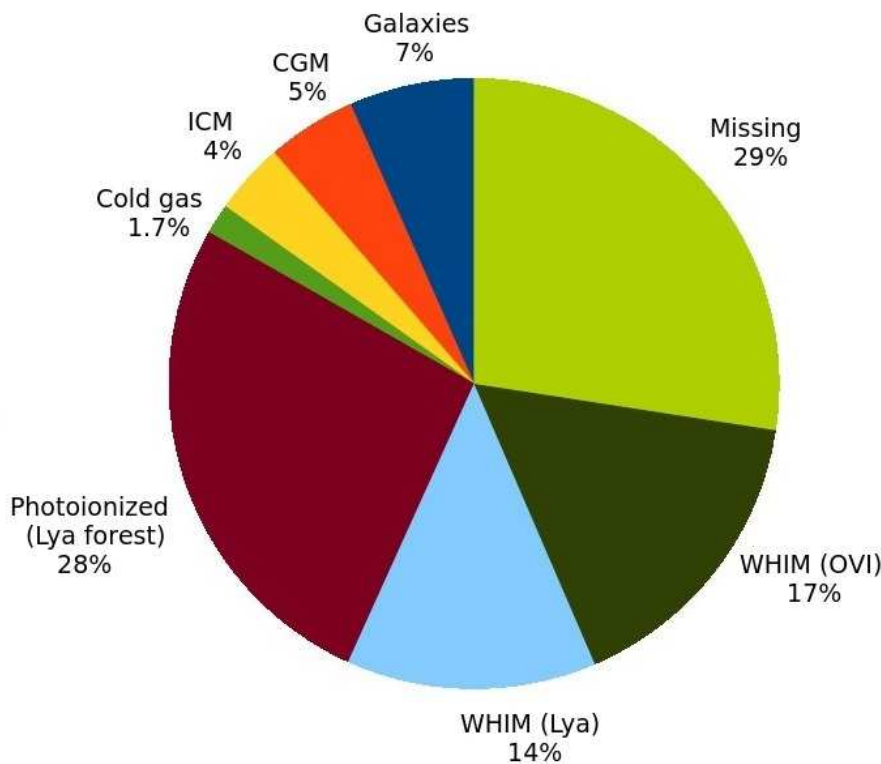


Fig. 1.2 Baryon census from Shull, Danforth & Tilton (2014).

1.4 Link to the feedback processes

The CGM is not a passive leftover from the galaxy formation process but is likely to play a crucial role in the evolution of the galaxy by influencing the feedback processes. The stars present in the central part of the galaxy are formed from the gas which cools out of the surrounding hot CGM or IGM. These stars have finite lifetimes. The massive stars undergo supernovae (SNe) explosion causing galactic scale winds or outflows. At the same time, super massive black holes (SMBH) located at the center of galaxies also enter the active

phase occasionally giving rise to active galactic nucleus (AGN) driven winds. Together, the AGN and SNe driven winds are responsible for throwing gas and metals out of the galaxy thus polluting the IGM and completing the feedback loop.

Theoretical calculations and numerical simulations have shown the need of such feedback mechanisms to explain the observed properties of galaxies (Cole et al. 1994, 2000; Dekel & Woo 2003; Vogelsberger et al. 2013 and references therein). For example, without any feedback, the observed galaxy luminosity function falls below the predicted one at low as well as high luminosity end. To explain this observation, SNe and AGN feedback have been invoked at low and high mass end, respectively. At low masses, the gravitational potential of dark matter haloes is shallow enough for the SNe driven galactic outflows, thus increasing the gas temperature and decreasing the star formation. This enhances the mass-to-light ratio in these systems as observed. On the other hand, at the high mass end, the energy injection due to these SNe is not sufficient against the gravity of these massive galaxies. In this mass range, the central super massive black hole related processes help to drive the feedback. A schematic diagram showing the discrepancy between observed and predicted galaxy luminosity function and the two feedback mechanisms operating in two different mass regimes is shown in Figure 1.3. This broad feedback scenario can also explain other qualitative features of galaxies. Dekel & Silk (1986) explained the observed dwarf galaxies scaling relations qualitatively by including SNe feedback. They showed that SNe driven galactic winds push a significant fraction of the halo gas thus suppressing the star formation in dwarf galaxies. Croton et al. (2006) showed that the AGN mode increases the temperature near the galactic center thus reducing the cooling flows as observed. In addition to the luminosity function, other observables such as Tully-Fisher relation, stellar-to-halo-mass relation, the star formation history etc. require SNe and AGN feedback for their explanation as found by many numerical simulations (eg. Davé, Oppenheimer & Finlator 2011; McCarthy et al. 2012; Vogelsberger et al. 2013).

Simultaneously, the galaxy accretes matter from the surrounding IGM. Earlier, the most accepted mechanism of gas infall was hot mode accretion, where the accreted gas is first shock heated followed by radiative cooling and finally contributing to the star formation in the galactic disk. Later, it was shown that gas can also reach the center via filaments of cold accretion, thus avoiding being shock heated. This accretion mechanism is called cold mode accretion. In higher mass galaxies ($M_h > 10^{11.4} M_\odot$), the preferred mode of accretion is hot, whereas, in lower mass galaxies ($M_h < 10^{11.4} M_\odot$), the cold mode is preferred (Birnboim & Dekel, 2003; Kereš et al., 2005). Assuming that gas accretion is only regulated by the dark matter halo results in the overproduction of stars. Bouché et al. (2010) observed this over-production of stars compared to the observed stellar mass in low mass galaxies at high

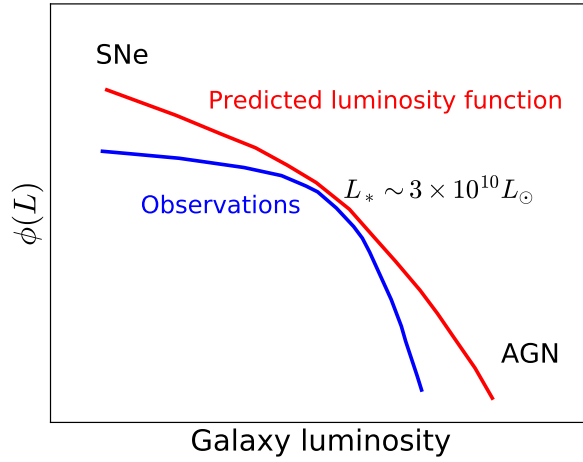


Fig. 1.3 Galaxy luminosity function and the role of feedback (taken from Silk & Mamon 2012).

redshifts. Somerville et al. (2008) also found a similar problem in high mass galaxies at low redshifts. They showed that the observed star formation rate can be explained by including AGN feedback in their model. Davé, Finlator & Oppenheimer (2011) showed that both outflows and infall play a crucial role in determining the gas metallicity.

Together, infall and outflows control the flow of material in and out of the galaxy. However, the hot CGM forms a barrier between the IGM and ISM. The outflowing material has to go through the CGM which can potentially leave the signature of the feedback processes in the CGM. Mathes et al. (2014) used the absorption spectra of intermediate redshift (0.1-0.7) galaxies and found that their cloud escape fraction is a decreasing function of halo mass. The galaxies below the halo mass $10^{11.5}M_{\odot}$ showed a much higher escape fraction ($\sim 55\%$) compared to lower mass galaxies ($\sim 5\%$). The mass limit where there is a sharp transition in the cloud escape fraction is close to the mass limit above which galactic haloes are expected to hold hot CGM (Rees & Ostriker, 1977; Silk, 1977; Birnboim & Dekel, 2003).

Even the infalling matter has to go through the CGM to fuel further star formation in the center. Gabor & Davé (2015) found that star formation is suppressed in massive galaxies ($10^{12} - 10^{13}M_{\odot}$) as a result of quenching of the direct supply of material to the center. This mass range coincides with the mass range where haloes can sustain hot CGM, thus providing a viable explanation for shutting down the supply of gas to fuel star formation. Goerdt & Ceverino (2015) showed using zoom-in hydrodynamic simulations that the gas infall velocity increases with increasing halo mass up to $M_h \sim 10^{12}M_{\odot}$. Beyond this halo mass, they observed a decline in the gas infall velocity. Again, the existence of hot circumgalactic gas in the mass range $10^{12} - 10^{13}M_{\odot}$ can explain the turn-around of the gas infall

velocity. Using cosmological hydrodynamic simulations, Oppenheimer et al. (2010) found that, in addition to the hot and cold modes of gas accretion, there exists a third mode of accretion, namely recycled accretion. When outflows are unable to leave the galaxy, they fall back onto the galaxy thus giving rise to recycled accretion. Oppenheimer et al. (2010) also showed that recycling of gas is more important in high mass galaxies compared to low mass ones. The presence of hot CGM in massive galaxies can decelerate the outflows and even stop them, giving rise to galactic fountains, hence producing mass dependent behavior of recycled accretion.

Recent simulations also indicate that varying the feedback recipe also changes the distribution and dynamics of the CGM (Barai et al., 2013; Suresh et al., 2015; Wang & Loeb, 2015; Fielding et al., 2017; Meiksin, Bolton & Puchwein, 2017). Therefore, the CGM provides an additional tool to constrain the feedback processes originating at the center. The feedback as well as the infalling material is affected by the CGM only when the CGM is hot enough to support against gravitational collapse, thus forming a thermal pressure supported barrier. Therefore, in this thesis, we focus on the hot phase of the circumgalactic gas.

1.5 Different phases of the CGM

The CGM is broadly divided into the following three phases.

1.5.1 Hot CGM

The low density, diffuse gas with temperature $> 10^6$ K represents the hot phase of the CGM. The observations of hot CGM phase are described in detail in following subsections.

X-ray emission

The gas in massive haloes is shock heated to high temperatures (Birnboim & Dekel, 2003; Kereš et al., 2005). Rees & Ostriker (1977); Silk (1977) first predicted the existence of a hot gaseous medium that envelops the stellar component of the galaxy. This was later supported by various numerical simulations. The high temperature of the gas enables it to emit in X-rays. However, galaxies host a smaller gas reservoir compared to galaxy clusters (gas mass \propto total galaxy mass) resulting in the faintness of X-ray emission (Benson et al., 2000). Thus, most of the CGM remains below the present detectability limit of X-ray telescopes. Also, X-ray observations were limited to few parsecs beyonds the center, where the contamination from the starburst driven winds can be a major contaminator. This contamination due to the

X-ray emission from SNe explosions (Wang et al., 2005) must be taken into account while trying to extract the X-ray emission from the CGM.

There have been claims that most of the X-ray emission observed in MilkyWay originates within a few kpc of the galactic center (Yao et al., 2009; Hagihara et al., 2010). However, there is a growing consensus that the hot CGM corona is responsible for the X-ray emission from the MilkyWay. Recently, Anderson & Bregman (2011); Dai et al. (2012); Anderson, Bregman & Dai (2013); Bogdán et al. (2013b,a); Walker, Bagchi & Fabian (2015) detected X-ray emission from the hot corona around a few massive spiral galaxies, out to a large distance (~ 100 kpc) from the central star forming region. Some of these galaxies are non-starburst galaxies which strongly rules out the contribution from SNe driven winds. These observations of the hot CGM suggest a gas density of roughly a few times 10^{-4}cm^{-3} out to 100 kpc. Moreover, Anderson et al. (2015) detected X-ray emission from galaxies down to $M_* \sim 10^{10.8}M_\odot$ by stacking a large number of galaxies using ROSAT (Rontgen Satellite) All-Sky survey and SDSS (Sloan Digital Sky Survey) survey combination. In Fang, Bullock & Boylan-Kolchin (2013), the authors examined X-ray surface brightness and pulsar dispersion measure observations of the hot corona of the MilkyWay for three different density profiles: Navarro-Frank-White (NFW; Navarro, Frenk & White 1997), a local hot disc and Maller & Bullock (2004) density distributions. They showed that the NFW profile is not compatible with these measurements whereas the other two profiles can satisfy them. They favour a flatter density distribution than the dark matter density profile (i.e. NFW profile). They show that the hot gas mass can be larger than $10^{10}M_\odot$, in agreement with Gupta et al. (2012).

Ram pressure stripping of satellite galaxies

Another constraint on the distribution and energetics of the CGM comes from the observed ram pressure stripping of the satellite galaxies as they pass through the hot corona of the MilkyWay. Greveich & Putman (2009) studied the HI content of many dwarf spheroidal satellite galaxies of the MilkyWay and M31. The dwarf satellites lying within 270 kpc were devoid of HI, whereas, the ones beyond 270 kpc were not. The ram pressure stripping due to the existence of a hot corona in their host galaxies lead to a coronal gas density $10^{-3.5}\text{cm}^{-3}$ out to 70 kpc. Gatto et al. (2013) also found the MilkyWay halo gas density close to $1.3 - 3.6 \times 10^{-4}\text{cm}^{-3}$, assuming the ram pressure to be the most dominant mechanism to remove gas from the satellites. They further showed that depending on the temperature profile of the hot halo, the CGM of the MilkyWay can play an important role in solving the missing baryon problem.

Quasar absorption spectroscopy

Another way to observe the CGM is with the help of their absorption features in the spectrum of a background quasar. When the light from a high redshift background quasar passes through the CGM of a foreground galaxy, it leaves the signature of the physical state of the CGM in the quasar spectrum. Such an absorption feature can be used to decode the density, temperature and other properties of the intervening CGM.

Unfortunately, this method is limited to galaxies with a background quasar, which are rare. The database of quasar-galaxy pairs has increased multifold with the installation of COS-halos (Cosmic Origin Spectrograph) onboard Hubble telescope (Tumlinson et al., 2011). In addition, galaxies with multiple quasar sightlines were detected. This has helped in probing the CGM at various impact parameters thus enabling one to infer the gas distribution profile of a galaxy, out to a few hundred kpc.

The quasar absorption spectroscopy studies by Shull, Danforth & Tilton (2014) and Werk et al. (2014) also indicate that the CGM may host a significant fraction of the missing baryons. The observation of various metal lines in the quasar spectrum holds the information about various phases of the CGM. Ford et al. (2013) showed that low ionization ions such as MgII trace the high density CGM, whereas, high ionization ions such as OVI trace the low density, high temperature phase of the CGM. Many simulations (eg. Suresh et al. 2015; Ford et al. 2016) have attempted to differentiate various feedback scenarios by studying the variation in the resultant metal absorption features. In the near future, better statistics of CGM observations and hydrodynamical simulations will improve the present understanding of physical processes shaping the CGM.

Sunyaev-Zel'dovich (SZ) effect

One more way to detect gas is through the SZ effect, which represents the distortion of black body spectrum of the CMB when it passes through the gas. However, the detection of the SZ effect so far has been limited to the ICM due to the sensitivity limit of the CMB surveys. Also, the small gas reservoir of the galaxies makes it difficult to detect the gas through SZ for individual galaxies. Fortunately, the launch of Planck satellite facilitated the study of lower mass systems due to its better sensitivity and all-sky coverage. Planck Collaboration et al. (2013) detected the thermal SZ (tSZ) signal down to galaxies with stellar mass $M_* \sim 2 \times 10^{11} M_\odot$ by stacking the galaxies observed in SDSS. Planck Collaboration et al. (2013) observation is consistent with no missing baryons i.e. the observed stacked tSZ signal agrees well with prediction of standard cosmology.

More recently, Hand et al. (2012) and Planck Collaboration et al. (2016) detected kinetic SZ (kSZ) signal in the data from ACT (Atacama Cosmology Telescope) and Planck missions, respectively. In both the cases, the kSZ signal is consistent with no missing baryons. This is contrary to the X-ray observations where a huge fraction of baryons seems to be missing or a strong feedback is required to explain the observations (Planck Collaboration et al., 2013). There is also an ongoing debate on whether stacked SZ data bears any feedback signature or not. A possible resolution of this problem is explored in Le Brun, McCarthy & Melin (2015), where the effect of large beam size of the Planck telescope and the assumption about the gas pressure profile is shown to be responsible for the discrepancy.

1.5.2 Warm CGM

The warm-hot phase of the CGM with intermediate density and temperature has the temperature range $10^5 - 10^6$ K. It is difficult to detect warm CGM in X-ray emission (with present X-ray telescopes) due to its low temperature, whereas, it is easier to detect this gas via UV absorption (Mulchaey et al., 1996; Mulchaey, 2000). This method has proved successful in detecting the warm CGM in galactic haloes, especially through collisionally ionized OVI (at temperature $\sim 3 \times 10^5$ K), which traces warm-hot CGM (see Stocke et al. (2017) and references therein). Tumlinson et al. (2011) observed the OVI absorption from 42 nearby galaxies using COS-halos. They found the metal lines out to ~ 150 kpc and inferred that this warm-hot phase of the CGM is a huge gas reservoir. They concluded that the amount of gas in this phase might be more than the gas mass in the ISM.

The origin and stability of warm CGM has been, however, questioned and investigated by many scientists. Maller & Bullock (2004) showed that high density, warm clouds can exist in the galactic halo, embedded in the hot, low density gas. Almost all sightlines through the galactic halo encounter OVI absorption lines (eg. Johnson, Chen & Mulchaey 2015; Faerman, Sternberg & McKee 2017; McQuinn & Werk 2017) which indicates 100% covering fraction for OVI. Faerman, Sternberg & McKee (2017), recently showed that warm CGM originates from the cooling tail of the hot CGM. This can also naturally explain the existence of warm gas out to a large galacto-centric distance. These OVI absorption lines represent collisionally ionized gas with a median temperature close to 3×10^5 K rather than a cool, photoionized gas. Faerman, Sternberg & McKee (2017) also reported that the cooling time of the warm gas is shorter than the hot gas with a flat density profile out to large distances from the galactic center. They suggested that, taken together the warm and hot CGM can resolve the missing baryon problem. McQuinn & Werk (2017) contend that the warm gas in low z galaxies can potentially hold all baryons within their virial radii. Contrary to these predictions, the hydrodynamical cosmological simulation by Cen (2013) indicated

that in the low z (< 0.5) galaxies, warm gas is not only sub-dominant compared to hot and cold gas, but its contribution to the total baryonic budget of a galaxy is small. Therefore, there is still room for improvement in the current knowledge and consensus on warm CGM.

1.5.3 Cool CGM

The high density gas with temperature $< 10^5$ K represents the cool phase of the CGM. Cool CGM is generally probed through its absorption lines present in the spectra of the background system. This method has been extensively used to infer cool CGM properties using low ions (the ions with low ionization potential) due to the fact that generally low ions trace the cold phase of the CGM (with some exceptions such as OVI tracing cool CGM due to different mechanisms for the production of the same ion (see Stern et al. 2016 for example), and these ions can be easily observed in quasar absorption spectra with currently available techniques.

In the last few decades, probes ranging from HI to various metal ions have been used to assess the nature and amount of halo gas (see Werk et al. (2014) and references therein). Chen et al. (2010) showed that cool CGM traced by MgII is commonly found in galactic haloes. Thom et al. (2012) observed a sample of early type galaxies with COS-halos and commonly detected HI absorption out to 150 kpc. They predicted the mass of the detected CGM to be $\gtrsim 10^9 - 10^{11} M_{\odot}$, comparable to the gas mass of the ISM of these galaxies. They also showed that cool CGM is not correlated with the star formation of these galaxies. Lehner et al. (2013) also showed that cool CGM contains a significant amount of previously unseen baryons by studying the HI content of $z \lesssim 1$ Lyman limit systems. They found that metal rich CGM traces the outflowing gas, whereas, the metal poor CGM traces the infalling gas. Lan, Ménard & Zhu (2014) extracted some 2000 galaxy-absorber pairs, observed in MgII using SDSS, WISE, and GALEX surveys. They show that cool CGM traced by MgII has a much higher covering fraction within 50 kpc for star forming galaxies than the passive galaxies, whereas, at impact parameters more than 50 kpc, the covering fraction is comparable for the two populations. Werk et al. (2014) studied the photo-ionized (due to the extragalactic UV background), cool CGM ($T \sim 10^4$) using COS-halos sample of $z \sim 0.2$, $L \sim L_*$ galaxies. They detected various low ions (MgII, SiII, CII, SiIII, CIII etc.) in absorption, out to 160 kpc. They predicted a lower limit to the mass of cool CGM, $M_{\text{CGM}}^{\text{cool}} \sim 6.5 \times 10^{10} M_{\odot}$, within the virial radius of the galaxy. This mass estimate, taken together with the estimate of hot CGM mass, can account for at least half of the missing baryons. However, Stern et al. (2016) found a much lower mass in cool CGM ($M_{\text{CGM}}^{\text{cool}} \sim 1.3 \times 10^{10} M_{\odot}$) compared to Werk et al. (2014), which accounts for only 1% of the total halo mass for L_* galaxies.

More recently, Prochaska et al. (2017) studied a COS-halos sample of $L \sim L_*$ Lyman limit systems. They found cool CGM mass to be $M_{\text{CGM}}^{\text{cool}} \sim 9 \times 10^{10} M_{\odot}$, and showed that hot and cool CGM, taken together, may resolve the missing baryon problem. They also suggested that the true problem lies in the inability to understand the physics governing the CGM as well as the limited existing data, due to which a good amount of baryons remain undetected. Although, there is a large scatter in the existing constraints on the CGM properties, the situation will hopefully improve with the availability of more data from independent measurements and our own understanding of CGM physics.

1.6 Motivation of the thesis

1.6.1 Detection of tSZ/kSZ effect from CGM

Large gas reservoirs such as galaxy clusters and groups have long been investigated using the SZ effect. However, it has been difficult to observe the SZ effect from galaxies due to the faintness of the signal as well as the large beam size of radio surveys. Only the high mass end of galaxy population has been detected in tSZ via stacking a large number of galaxies. The situation is improving with ongoing surveys like SPT, which has much better angular resolution and sensitivity, enabling it to resolve smaller systems. Futuristic surveys like PIXIE will perform even better on small scales, where the contribution from galaxies is thought to be important. This motivates us to probe the ability of these ongoing and futuristic radio surveys to detect the tSZ and kSZ power spectra from hot CGM.

1.6.2 Advantage of cross-correlations

One of the most convenient ways of enhancing the detectability of a signal is to cross-correlate it with a stronger signal. This method not only increases the detectability of the signal, but also gives better constraints on model parameters due to different dependences of the two signals on these parameters. This motivated us to check whether the detectability of the SZ effect from the CGM can be enhanced by cross-correlating it with the distribution of galaxies and what the cross-correlation power spectrum may tell us about the physical properties of the CGM.

1.6.3 X-ray emission from the CGM

As explained in the previous section, it is difficult to detect the X-ray emission from individual galaxies due to the faintness of the signal. Fortunately, the X-ray-galaxy cross power

spectrum can be helpful in studying the CGM. Additionally, according to numerical simulations, CGM bears the signature of feedback processes originating near the centres of galaxies (Suresh et al., 2015). The high resolution present generation X-ray telescopes such as Chandra, XMM-Newton are not very useful in dealing with the X-ray power spectrum due to their extremely small sky coverages. However, eROSITA will have a large sky coverage with much better angular resolution than the previous all sky X-ray survey, RASS. It will enable the use of the angular power spectrum to study the hot gas at multiple scales. Analogous to the SZ-galaxy cross power spectrum, the detectability of X-ray signal from hot CGM can be increased by cross-correlating it with the distribution of galaxies. This has inspired us to probe how eROSITA can help to constrain the properties of the CGM as well as the feedback physics.

1.6.4 Can we quantify the role of the CGM in galaxy evolution?

The existence of hot, pressure supported circumgalactic environment is surely going to impact the flow of gas in and out of the galaxy. There are indirect evidences indicating the interference of CGM with the infalling and the outflowing gas. It is also linked to the metallicity evolution of the Universe as the outflowing gas carries the metals from the inner regions of the galaxies to galactic outskirts and IGM. Many authors have used state-of-the-art cosmological hydrodynamical simulations to study the exact details of various modes of outflows/infall and how it affects the galactic evolution. However, the results vary depending on the details of the simulation used. Therefore, it is a good idea to take a step back and use a simpler analytical approach towards the interaction between the CGM, outflows and the IGM, and compare the results with observations as well as simulations. This idea is the basis of our work on the suppression of galactic outflows due to the existence of the CGM and infall.

1.6.5 The AGN foreground

One of the biggest hurdles in extracting the X-ray signal from the CGM is contamination due to the AGNs. Therefore, it is essential to model X-ray emission from the AGNs. Unfortunately, there is lack of a halo model for AGNs, necessary to correctly deal with the AGN contamination in Fourier space. This situation gave us the opportunity to build a framework for the detailed modeling of the AGN power spectrum, required to extract the hot gas contribution. As a byproduct of this exercise, we obtained the halo model for AGNs themselves, which can now be used to study the resolved as well as unresolved X-ray power spectrum to explore AGN physics.

Additionally, there are large uncertainties present in the HOD model parameters, which are crucial in building the halo model. The prime reason for such large uncertainties is the limited sample of X-ray AGNs. This situation is expected to improve with the launch of eROSITA, which will uncover a large population of AGNs. Therefore, eROSITA provides the chance to reduce the ambiguity in the determination of HOD model parameters and that is another motivation for our work on X-ray AGN power spectrum.

1.7 Plan of the thesis

In Chapter 2, we study the SZ effect due to the circumgalactic gas in galaxies (i.e. $M_h \leq 10^{13} M_\odot$). We compute tSZ as well as kSZ angular power spectrum from the galaxies hosting hot CGM. To determine the mass limit separating the galaxies with and without a hot circumgalactic environment, we compare the gas cooling time-scale with the halo destruction time-scale. We include only those haloes in which the gas remains hot for long enough time-scales. To do this, we calculate the gas cooling and halo destruction time-scales as a function of halo mass and redshift, and consider the SZ effect from only those haloes where the gas cooling time-scale is larger than the halo destruction time-scale. For the assumed gas density and temperature, we find that estimated kSZ power spectrum is larger than the tSZ power spectrum and it can be larger than the tSZ power spectrum due to the ICM at small angular scales ($l > 10^4$). Our estimation of the tSZ effect is consistent with marginal detection of the stacked tSZ signal in galaxy mass regime ($M_h \gtrsim 10^{12.5}$) by Planck Collaboration et al. (2013). We predict the detectability of the power spectra with SPT-like survey and a more futuristic cosmic variance limited survey. We also compute the constraints on CGM properties, that can be obtained from these surveys using Fisher matrix analysis.

In Chapter 3, we compute the cross power spectrum between the tSZ effect, X-ray emission from the CGM and the distribution of galaxies. We forecast the detectability of these cross-correlation signals with present and upcoming CMB (SPT), X-ray (eROSITA) and optical (DES, LSST) surveys. We show that tSZ-galaxy and X-ray-galaxy cross power spectra can be detected with sufficient SNR ($\gtrsim 3$) using the above survey combinations. We find that the SNR of both tSZ-galaxy and X-ray-galaxy power spectra peak for high mass and intermediate redshift galaxies, with X-ray cross-correlation peaking at a slightly lower redshift than the tSZ cross-correlation power spectrum. We find that a steeper density distribution of the CGM results in a larger cross power spectra, especially at smaller scales. We use the Fisher matrix analysis to forecast the uncertainties in the CGM density, fraction and temperature and show that these cross-correlation signals can be excellent probes of CGM properties. We also comment on the possibility of differentiating various feedback scenar-

ios giving rise to different CGM distributions, and hence leaving different signatures in the resultant cross power spectra.

In Chapter 4, we investigate the competition between galactic outflows, cosmological infall and hot CGM, which plays a major role in shaping the galaxies. We find that in the absence of a hot circumgalactic environment, the infall can reduce the mass limit beyond which the outflows are suppressed by the gravitational field of the galaxy approximately by a factor of two. However, the presence of hot CGM in massive galaxies creates a barrier between the stellar component of galaxies and the IGM thus interfering with outflows and infall. We show that hot CGM is more effective in suppressing outflows at low redshifts ($z < 3.5$), whereas the infall is more effective at higher redshifts. We also study the impact of outflow suppression on the metal enrichment history of galaxies and the IGM.

In Chapter 5, we study the X-ray emission from AGNs, which are the main source of contamination while extracting the X-ray signal from hot gas in the 0.5-2 keV band. We construct a halo model to compute the AGN power spectrum. To do this, we combine the X-ray luminosity function (XLF) of AGNs and their halo occupation distribution (HOD) model. We also confirm that the two inputs (XLF and HOD) of the AGN halo model are in agreement with each other. We then calculate the X-ray auto power spectrum due to the resolved as well as unresolved AGNs for eROSITA, which is an upcoming all sky X-ray mission. We compare the relative contribution of different components of the total power spectrum (i.e. Poisson and one- and two-halo clustering terms). We note that the uncertainty in the HOD model is one of the largest source of uncertainty in the determination of the power spectrum. Therefore, we include X-ray-lensing cross-correlation in our power spectrum analysis and find that the X-ray-lensing cross power spectrum can reduce the uncertainties in the HOD model parameters by an order of magnitude for eROSITA-LSST survey combination.

In Chapter 6, we present the summary and main conclusions of this thesis. An outline of future research directions is also presented at the end of the chapter.

Chapter 2

CMB distortion from circumgalactic gas

Based on:

Singh, P., Nath, B. B., Majumdar, S., Silk, J. 2015, MNRAS, 448, 2384

We study the SZ distortion of the cosmic microwave background radiation (CMBR) from extensive CGM in massive galactic haloes. Recent observations have shown that galactic haloes contain a large amount of X-ray emitting gas at the virial temperature, as well as a significant amount of warm OVI absorbing gas. We consider the SZ distortion from the hot gas in those galactic haloes in which the gas cooling time is longer than the halo destruction time scale. We also consider the SZ effect from warm circumgalactic gas. Finally, we study the detectability of the SZ signal from circumgalactic gas in two types of surveys, a simple extension of the SPT survey and a more futuristic cosmic variance-limited survey.

Main Results

- We show that SZ distortion signal from the hot gas in these galactic haloes at redshifts $z \approx 1-8$ can be significant at small angular scales ($\ell \sim 10^4$), and dominate over the signal from galaxy clusters.
- The estimated SZ signal for most massive galaxies (halo mass $\geq 10^{12.5} M_\odot$) is consistent with the marginal detection by *Planck* at these mass scales.
- The integrated Compton distortion from the warm OVI absorbing gas is estimated to be $y \sim 10^{-8}$, which could potentially be detected by experiments planned for the near future.
- We find that these surveys can easily detect kSZ signal from the CGM. With the help of Fisher Matrix analysis, we find that it will be possible for these surveys to constrain the gas fraction in CGM, after marginalizing over cosmological parameters, to $\lesssim 33\%$, in case of no redshift evolution of the gas fraction.

2.1 Introduction

The standard scenario of galaxy formation predicts that baryonic gas falls into dark matter potentials and gets heated to the virial temperature (Silk, 1977; White & Rees, 1978; White & Frenk, 1991). This gas then cools radiatively, and if the temperature is low enough ($T \leq 10^6$ K) for significant radiation loss, then most of the galactic halo gas drops to low temperature and no accretion shock develops in the halo (Birnboim & Dekel, 2003). In the case of low mass galaxies, most of the accretion takes place through the infall of cold material from the IGM. However, in massive galaxies, the hot halo gas cools slowly and should remain warm/hot for a considerable period of time. This halo gas, if present, could potentially contain a large fraction of the baryons in the universe which is unaccounted for by collapsed gas and stars in galaxies, and could explain the missing baryon problem (Fukugita, Hogan & Peebles, 1998; Anderson & Bregman, 2010).

Although numerical simulations have shown that disc galaxies should be embedded in a hot gaseous halo, this gas has been difficult to nail down observationally because of faintness of the X-ray emission (Benson et al., 2000; Rasmussen et al., 2009; Crain et al., 2010). Recent observations have finally discovered this hot coronal gas extended over a large region around massive spiral galaxies (Anderson & Bregman, 2011; Dai et al., 2012; Anderson, Bregman & Dai, 2013; Bogdán et al., 2013b,a; Anderson et al., 2015; Walker, Bagchi & Fabian, 2015). The typical densities at galactocentric distances of $\gtrsim 100$ kpc is inferred to be a few times 10^{-4} cm^{-3} (e.g., Bogdán et al. 2013a), at a temperatures of ~ 0.5 keV. The amount of material implied in this extended region is unlikely to come from the star formation process, as shown by Bogdán et al. (2013b). An extended region of CGM has also been observed through OVI absorption lines around massive galaxies at $z \lesssim 1$ (Tumlinson et al., 2011), although these observations probe clouds at $T \sim 10^{5.5}$ K.

At the same time, the presence of hot halo gas around the Milky Way galaxy has been inferred via ram pressure arguments from the motion of satellite galaxies (Grcevich & Putman, 2009; Putman, Peek & Joung, 2012; Gatto et al., 2013). These observations suggest that the density profile of the hot coronal gas in our Galaxy is rather flat out to large radius, with $n \sim 10^{-3.5} \text{ cm}^{-3}$. Theoretically, one can understand this profile from simple modelling of hot, high entropy gas in hydrostatic equilibrium (Maller & Bullock, 2004; Sharma et al., 2012; Fang, Bullock & Boylan-Kolchin, 2013). While in galaxy clusters, the high entropy of the diffuse gas produces a core, for massive galaxies (with implied potential wells shallower than in galaxy clusters), the core size is relatively large and extends to almost the virial radius.

One of the implications of this hot coronal gas in the haloes of massive galaxies is SZ distortion of the CMBR (Planck Collaboration et al., 2013). The average y distortion of the

CMBR from massive galaxies is likely to be small. However, the anisotropy power spectrum could have a substantial contribution from the hot gas in galactic haloes. The SZ distortion from galaxy clusters have been computed with the observed density and temperature profiles of the X-ray emitting gas, or the combined pressure profile (e.g, Majumdar 2001; Komatsu & Seljak 2002; Efstathiou & Migliaccio 2012). In the case of galactic haloes, because of the expected flatter density profile, the resulting y -distortion could be larger than that of galaxy clusters for angular scales that correspond to the virial radii of massive galaxies, i.e., $\ell \sim 10^4$. These angular scales are being probed now and therefore the contribution to SZ signal from galactic haloes is important. In this chapter, we calculate angular power spectrum from both the thermal and kinetic SZ (tSZ and kSZ, respectively) effects, if a fraction $f \sim 0.11$ of the total baryonic content of massive galaxies is in the form of hot or ionized halo gas.

Although such a fraction of gas has been estimated from the observations of NGC 1961 and NGC 6753 (Bogdán et al., 2013b), it remains uncertain whether it is a representative value, or whether it can be as low as 0.05. Recent studies of absorption from halo gas along the lines of sight to background quasars show that roughly half of the missing baryons is contained in the halo as warm (at $\sim 10^4$ and $\sim 10^{5.5}$ K) components. We also discuss the possible SZ signatures from this cool-warm gas in galactic haloes.

2.2 SZ distortion from hot galactic halo gas

For simplicity, we assume that galactic haloes contain a constant fraction of the total halo mass, independently of the galaxy mass. If we consider the total baryon fraction $\Omega_B/\Omega_M \sim 0.16$, and the fraction of the total mass that is likely to be in the disc, which is predicted to be ~ 0.05 (Mo, Mao & White, 1998; Moster et al., 2010; Leauthaud et al., 2012; Dutton et al., 2010), then one can assume a fraction $f_{\text{gas}} = 0.11$ of the total halo mass to be spread throughout the halo. We also assume it to be uniform in density, with a temperature given by the virial temperature of the halo. The uncertainties in gas fraction and temperature are explored later in Section 2.5.1. The cosmological parameters needed for our calculations are taken from the recent Planck results (Table 2 of Planck Collaboration et al. 2014).

2.2.1 tSZ effect

When CMBR photons are inverse Compton scattered by high energy electrons, the CMB spectrum is distorted giving rise to the tSZ effect. This effect is represented in terms of the Compton y -parameter defined as, $y = (k_b T_e n_e \sigma_T L)/(m_e c^2)$ where σ_T is the Thomson scattering cross section, T_e is the temperature ($T_e \gg T_\gamma$) and n_e is the electron density of

the medium, considered to be uniform here, and ℓ is the distance traversed by the photons through the medium. The profile of y can be written in terms of the impact parameter w , or the angle $\theta = w/D_A$ (where D_A is the angular diameter distance) as

$$\begin{aligned} y(w) &= \frac{2k_b T_v n_e \sigma_T}{m_e c^2} \sqrt{R_v^2 - w^2}, \\ y(\theta) &= \frac{2k_b T_v n_e \sigma_T R_v}{m_e c^2} \sqrt{1 - \frac{D_A^2 \theta^2}{R_v^2}}. \end{aligned} \quad (2.1)$$

Here, the electron density $n_e = \frac{\rho_{\text{gas}}}{\mu_e m_p}$ of the hot gas is determined by the requirement that the total hot gas mass within the virial radius is a fraction $f_{\text{gas}} = 0.11$ of the halo mass. The virial radius of a halo of mass M collapsing at redshift z is given by

$$R_{\text{vir}} = 0.784 \left(\frac{M}{10^8 h^{-1}} \right)^{1/3} \left(\frac{\Omega_M}{\Omega_M(z)} \frac{\Delta(z)}{18\pi^2} \right)^{-1/3} \left(\frac{1+z}{10} \right)^{-1} h^{-1} \text{kpc} \quad (2.2)$$

where $\Omega_M(z) = \Omega_M(1+z)^3/E^2(z)$, the critical overdensity $\Delta(z) = 18\pi^2 + 82d - 39d^2$ and $d = \Omega_M(z) - 1$.

Later in this chapter, we will also discuss the effect of varying f_{gas} , including its possible redshift evolution.

2.2.2 kSZ effect

If the scattering medium has bulk velocity with respect to the CMB frame, the CMBR is anisotropic in the rest frame of scattering medium. The scattering makes CMBR isotropic in the rest frame of scattering medium, resulting in the distortion of CMB spectrum with respect to the observer and giving rise to kSZ effect. The kSZ effect is proportional to the line of sight peculiar velocity and optical depth of the scattering medium. In the non-relativistic limit, the Compton y -parameter for the kSZ effect is defined as, $y = (v_{\text{los}} n_e \sigma_T L)/c$, where, v_{los} is the line-of-sight peculiar velocity of the scattering medium. The tSZ effect and kSZ effect have different frequency dependences which makes them easily separable with good multi-frequency data. In contrast to SZ effect, the spectral shape of CMB is unchanged by kSZ effect. In the Rayleigh-Jeans limit, the ratio of change in CMB temperature caused by these two effects is :

$$\begin{aligned} \frac{\Delta T_{\text{kin}}}{\Delta T_{\text{th}}} &\approx \frac{1}{2} \frac{v_{\text{los}}}{c} \left(\frac{k_b T_e}{m_e c^2} \right)^{-1}, \\ &\approx 0.09 \left(\frac{v_{\text{los}}}{1000 \text{ km s}^{-1}} \right) \left(\frac{k_b T_e}{10 \text{ keV}} \right)^{-1} \end{aligned} \quad (2.3)$$

For galaxy clusters, $k_b T_e \sim 10$ keV and $v_{\text{los}} \sim$ few hundred km/sec which makes tSZ \gg kSZ. But for the case of galaxies with virial temperature $T_e \sim 10^6$ K, hence $k_b T_e \sim 0.1$ keV, thus making kSZ $>$ tSZ.

2.3 The SZ Power Spectrum

The SZ power spectrum arises by summing over the contributions from all haloes that would distort the CMB convolved with the template distortion for the haloes, as a function of mass and redshift; the distribution of the haloes can be approximated by fits to outputs from N-body simulations. However, not all dark matter haloes identified in the simulations would contribute to the SZ C_ℓ , and one has to use *only* those galactic haloes where the gas has not cooled substantially. This is discussed in detail in Section 2.3.2.

2.3.1 tSZ C_ℓ

The tSZ template for contribution by a galactic halo is given by the angular Fourier transform of $y(\theta)$ (see Equation 2.1) and is given by

$$\begin{aligned}
 y_l &\approx 2\pi \int_0^\pi \theta y(\theta) J_o[(l+1/2)\theta] d\theta, \\
 &= \frac{4\pi k_b \sigma_T R_v}{m_e c^2} \int_0^\pi \theta T_v n_e \sqrt{1 - \frac{D_A^2 \theta^2}{R_v^2}} J_o[(l+1/2)\theta] d\theta \\
 &= \frac{8k_b T_v n_e \sigma_T R_v^{3/2}}{m_e c^2 D_A^{1/2}} \left(\frac{\pi}{2l+1}\right)^{3/2} J_{3/2}\left[(l+1/2)\frac{R_v}{D_A}\right].
 \end{aligned} \tag{2.4}$$

The last equality follows from Gradshteyn & Ryzhik (1980).

The angular power spectrum due to the tSZ effect by hot diffuse gas in galactic haloes is given by

$$C_l = g^2(x) C_l^{yy} \tag{2.5}$$

Where, $g(x) = x \coth(x/2) - 4$, and C_l^{yy} is frequency independent power spectrum.

$$C_l^{yy} = C_l^{yy(P)} + C_l^{yy(C)} \tag{2.6}$$

where, $C_l^{yy(P)}$ is the Poisson term and $C_l^{yy(C)}$ is clustering or correlation term. These two terms can be written as (Komatsu & Kitayama, 1999)

$$\begin{aligned} C_l^{yy(P)} &= \int_0^{z_{\max}} dz \frac{dV}{dz} \int_{M_{\min}}^{M_{\max}} dM \frac{dn(M, z)}{dM} |y_l(M, z)|^2 \\ C_l^{yy(C)} &= \int_0^{z_{\max}} dz \frac{dV}{dz} P_M(k = \frac{l}{r(z)}, z) \left[\int_{M_{\min}}^{M_{\max}} dM \frac{dn(M, z)}{dM} b(M, z) y_l(M, z) \right]^2. \end{aligned} \quad (2.7)$$

Here $r(z) = (1+z)D_A$ is the comoving distance, $\frac{dV}{dz}$ is differential comoving volume per steradian, $P_M(k, z)$ is matter power spectrum, $b(M, z)$ is the linear bias factor, and $\frac{dn(M, z)}{dM}$ is the differential mass function. We have used the Sheth-Tormen mass function

$$\frac{dn}{dM} dM = A \sqrt{\frac{2\alpha v^2}{\pi}} \frac{\rho_M}{M^2} e^{-\frac{\alpha v^2}{2}} \left[-\frac{d \log \sigma}{d \log M} \right] \left[1 + (\alpha v^2)^{-p} \right] dM, \quad (2.8)$$

where $A = 0.322184$, $\alpha = 0.707$ and $p = 0.3$ (Sheth, Mo & Tormen, 2001). We have used the bias factor from Jing (1999),

$$b(M, z) = \left(1 + \frac{0.5}{v^4} \right)^{(0.06 - 0.02n)} \left(1 + \frac{v^2 - 1}{\delta_c} \right) \quad (2.9)$$

with $v = \frac{\delta_c}{D_g(z)\sigma(M)}$, where $D_g(z)$ is the growth factor, n is the index of primordial power spectrum, $\delta_c = 1.68$ is the critical overdensity and $\sigma(M)$ is the present day smoothed (with top hat filter) variance.

2.3.2 Mass and redshift range

As mentioned earlier, not all the galactic haloes given by ST mass function (i.e Equation 2.8) will contribute to the SZ C_l . For a realistic estimate of the CMB distortion from circumgalactic gas in galaxies, we need to use only those galactic haloes in which the hot halo gas does not cool substantially, so that the hot gas persists for a considerable period of time and can contribute to the anisotropy. The cooling time of the gas is defined as $t_{\text{cool}} = 1.5nkT/(n_e^2\Lambda(T))$, where n is the particle density ($\sim \frac{\mu_e}{\mu} n_e$), μ is mean molecular weight of the gas, v_e is the mean molecular weight per free electron and $\Lambda(T)$ is the cooling function. We assume the galactic halo gas to be of metallicity $0.1 Z_{\odot}$, and use the cooling function from (Sutherland & Dopita, 1993).

This cooling time should be compared with a time scale corresponding to the destruction of these galactic haloes in the merger or accretion processes, which would lead to the formation of larger haloes. Every merging event leads to heating of the halo gas back to the virial temperature. It is therefore reasonable to assume that the halo gas would remain

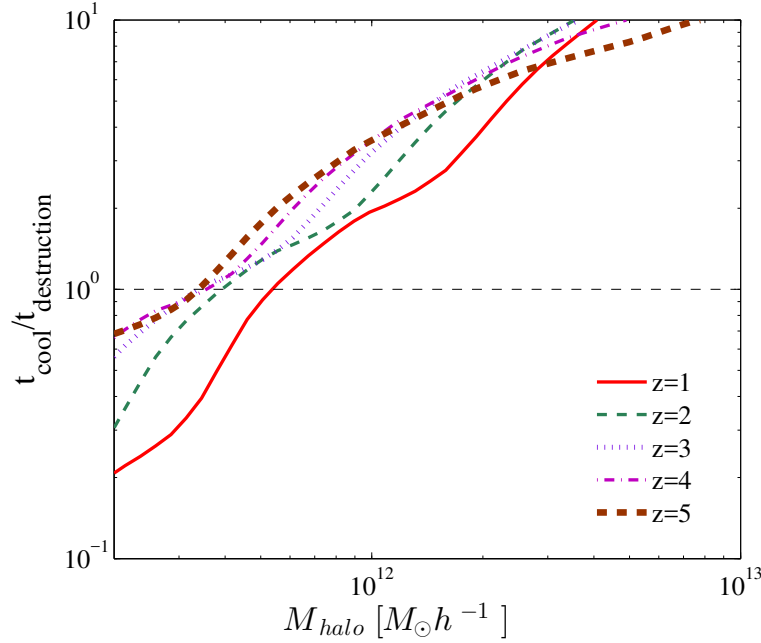


Fig. 2.1 The ratio of cooling time to destruction time scale of haloes is shown as a function of halo mass collapsing at $z = 1$ (red solid line), $z = 2$ (thin green dashed line), $z = 3$ (blue dotted line), $z = 4$ (magenta dot-dashed line) and $z = 5$ (thick brown dashed line).

hot at the virial temperature if the cooling time is longer than the time corresponding to the destruction of haloes.

We have used an excursion set approach to calculate the destruction time (Lacey & Cole, 1993, 1994). For Press-Schechter mass function the destruction time for a galactic halo of mass M at time t is

$$\begin{aligned} t_{\text{dest}}(M, t) &= [\phi(M, t)]^{-1}, \\ &= \left[\int_{M(1+\epsilon)}^{\infty} \tilde{Q}(M, M_1; t) dM_1 \right]^{-1} \end{aligned} \quad (2.10)$$

Where $\tilde{Q}(M, M_1; t)$ is the probability that an object of mass M grows into an object of mass M_1 per unit time through merger or accretion at time t .

$$\begin{aligned} \tilde{Q}(M, M_1; t) dM_1 &= \sqrt{\frac{2\sigma^2(M_1)}{\pi}} \left[\frac{\sigma^2(M)}{\sigma^2(M_1)(\sigma^2(M) - \sigma^2(M_1))} \right]^{\frac{3}{2}} \left| \frac{d\delta}{dt} \right| \exp \left[-\frac{\delta^2(\sigma^2(M) - \sigma^2(M_1))}{2\sigma^2(M)\sigma^2(M_1)} \right] \\ &\times \left| \frac{d\sigma(M_1)}{dM_1} \right| dM_1 \end{aligned} \quad (2.11)$$

Here we have used $\varepsilon = 0.1$. For the mass range considered, the destruction time for Sheth-Tormen mass function and Press-Schechter mass function give similar results (Mitra et al. 2011). For simplicity we have used the Press-Schechter mass function to calculate the destruction time.

We show the ratio of the cooling time to destruction timescale as a function of mass at different redshifts in Figure 2.1. Based on this estimate, we use those galactic haloes in our calculation of CMBR anisotropy for which $t_{\text{cool}}/t_{\text{dest}} \geq 1$, so that gas in these galactic haloes cannot cool quickly. This condition is used to determine the lower mass limit of galactic haloes M_{min} in Equation 2.7. We have used $M_{\text{max}} = 10^{13} h^{-1} M_{\odot}$ for the upper mass limit. For upper redshift limit of integration in Equation 2.7 it is sufficient to take $z_{\text{max}} = 8$ (see Figure 2.4).

2.3.3 kSZ C_{ℓ}

Analogously to the tSZ effect, the angular Fourier transform of Compton y-parameter for the kSZ effect is given by:

$$y_l \approx 8 \frac{v_{\text{los}}}{c} \frac{n_e \sigma_T R_v^{3/2}}{D_A^{1/2}} \left(\frac{\pi}{2l+1} \right)^{3/2} J_{3/2} \left[(l+1/2) \frac{R_v}{D_A} \right]. \quad (2.12)$$

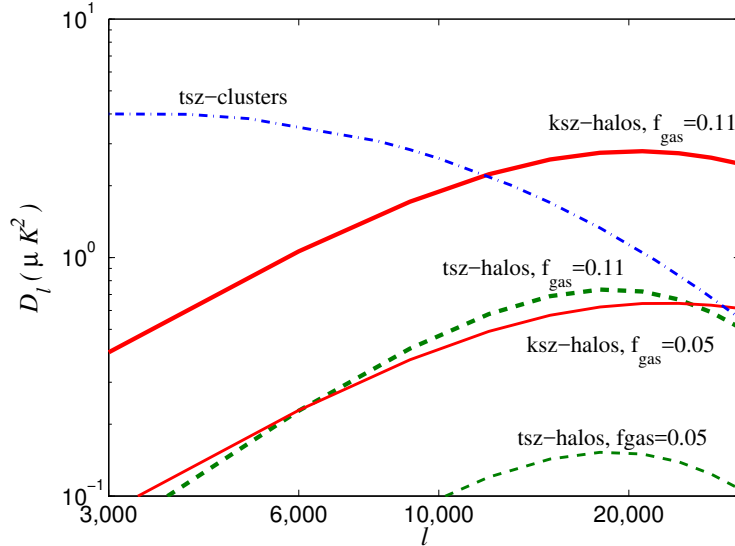


Fig. 2.2 Angular power spectrum of CMBR at 150 GHz over a larger range of ℓ , for tSZ (green dashed line) and kSZ (red solid line) from galactic haloes, compared with tSZ from clusters (blue dot-dashed line). Here the thick and thin lines correspond to $f_{\text{gas}} = 0.11$ and $f_{\text{gas}} = 0.05$ respectively.

A crucial input into the calculation of the kSZ C_ℓ is the line of sight peculiar velocity of the dark matter halo which depends on its mass M , redshift and the overdensity of the environment δ in which the halo is present (Sheth & Diaferio, 2001; Hamana et al., 2003; Bhattacharya & Kosowsky, 2008). The probability distribution function of the line of sight velocity of a halo with mass M located in a region of overdensity δ is

$$p(v_{\text{los}}|M, \delta, a) = \sqrt{\frac{3}{2\pi}} \frac{1}{\sigma_v(M, a)} \exp\left(-\frac{3}{2} \left[\frac{v}{\sigma_v(M, a)}\right]^2\right) \quad (2.13)$$

with the 3D velocity dispersion given by

$$\begin{aligned} \sigma_v(M, a) &= [1 + \delta(R_{\text{local}})]^{\mu(R_{\text{local}})} \sigma_p(M, a), \\ &= [1 + \delta(R_{\text{local}})]^{\mu(R_{\text{local}})} a H(a) D_A \left(\frac{d \ln D_A}{d \ln a} \right) \\ &\quad \times \left(1 - \frac{\sigma_0^4(M)}{\sigma_{-1}^2(M) \sigma_1^2(M)} \right)^{1/2} \sigma_{-1}(M), \end{aligned} \quad (2.14)$$

where $\sigma_p(M, a)$ is the rms peculiar velocity at the peaks of smoothed density field and σ_j 's are the moments of initial mass distribution defined as

$$\sigma_j^2(M) = \frac{1}{2\pi^2} \int_0^\infty dk k^{(2+2j)} P(k) W^2(kR(M)). \quad (2.15)$$

Here, smoothing scale $R(M)$ is given by $\left(\frac{3M}{4\pi\rho_M}\right)^{1/3}$, $W(kR)$ is the top hat filter and ρ_M is the present day mean matter density. The dependence of peculiar velocity on its environment is contained in parameters R_{local} , $\mu(R_{\text{local}})$ and $\delta(R_{\text{local}})$. These parameters are obtained by the conditions (Bhattacharya & Kosowsky, 2008)

$$\mu(R_{\text{local}}) = 0.6 \frac{\sigma_0^2(R_{\text{local}})}{\sigma_0^2(10 \text{ Mpc/h})}. \quad (2.16)$$

with $\sigma_0(R_{\text{local}}) = 0.5/\sqrt{(1+z)}$ and $\delta(R_{\text{local}}) = \sqrt{\sigma_0(R_{\text{local}})}$.

The angular power spectrum due to kSZ effect by this hot diffuse gas is independent of frequency, and is given by

$$C_l^{yy} = C_l^{yy(\text{P})} + C_l^{yy(\text{C})} \quad (2.17)$$

Where, $C_l^{yy(\text{P})}$ and $C_l^{yy(\text{C})}$ are Poisson and clustering terms given by Equation 2.7.

2.3.4 SZ from CGM -vs- SZ from ICM

We plot the multipole dependence of both tSZ and kSZ C_ℓ from the CGM, in Figure 2.2, in terms of $D_\ell \equiv \frac{l(l+1)}{2\pi} C_\ell \bar{T}_{\text{CMB}}^2$, where, \bar{T}_{CMB} is present day mean CMB temperature in units of micro-Kelvin. In the same figure, we plot the tSZ C_ℓ from hot gas in clusters of galaxies. We find that SZ C_ℓ 's from the CGM peak above $\ell \sim 15000$, whereas the tSZ from ICM peaks at $\ell \sim 3000$ and then falls at higher ℓ -values.; the tSZ signal from CGM dominates that from ICM over $\ell > 30000$, whereas the kSZ from galactic haloes overtakes tSZ from clusters earlier at $\ell > 10000$.

We have over-plotted South Pole Telescope (SPT) and Atacama Cosmology Telescope (ACT) data, with grey and black bars, respectively, and auto correlation lines from Figure 4 of Addison, Dunkley & Spergel (2012) on top of SZ C_ℓ from galactic haloes for a smaller range $3000 < \ell < 10000$ in Figure 2.3. This figure shows the contribution from tSZ and kSZ from galactic haloes with red solid (thick) and blue solid (thick) lines. For comparison, the tSZ and kSZ signals from galaxy clusters are shown as red and blue solid (thin) lines. Also, the contribution from sources responsible for Cosmic Infrared Background (CIB) are shown, for both poisson (brown dashed line) and the clustered case (brown dot-dashed line). The contribution from clustering of radio sources is shown in green dotted line. The lensed primary signal is shown as black dashed line. The comparison of tSZ and kSZ signals from galactic haloes and galaxy clusters shows that kSZ signal from galactic haloes becomes comparable to galaxy cluster signal at $\ell \sim 10000$. This is because of the fact that kSZ is more important for lower mass haloes, which correspond to smaller angles and larger ℓ values.

2.3.5 Redshift distribution of the angular power spectrum

The redshift distribution of C_ℓ can be determined using

$$\frac{d \ln C_\ell}{d \ln z} = \frac{z \frac{dV}{dz} \int dM \frac{dn(M,z)}{dM} |y_\ell(M,z)|^2}{\int dz \frac{dV}{dz} \int dM \frac{dn(M,z)}{dM} |y_\ell(M,z)|^2} \quad (2.18)$$

We show the redshift distribution of C_ℓ for $\ell = 3000, 6000, 10000$ and 20000 for tSZ and kSZ effect in Figure 2.4. For tSZ effect (shown in thin lines), for $\ell = 3000$, C_ℓ has a peak at $z \sim 2$. This peak shifts to higher redshifts with increasing value of ℓ . For all ℓ values ($\ell > 3000$), there is non-negligible contribution to C_ℓ coming from $z > 5$.

In case of kSZ effect (thick lines), for $\ell = 3000$ there is a broad peak around $z \sim 1-2$, and the contribution to C_ℓ is significant even below $z = 1$. The peak shifts to higher redshifts with increasing value of ℓ . The contribution from higher redshift becomes more important

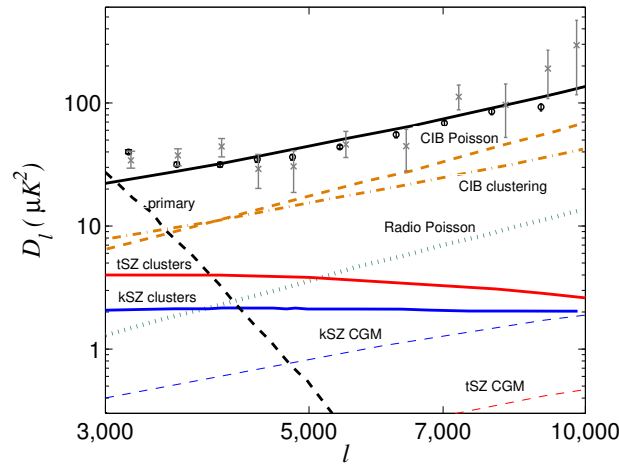


Fig. 2.3 Angular power spectrum of CMBR at 150 GHz from different processes and compared with data points from ACT (grey bars) and SPT (black bars). The tSZ from galactic haloes calculated here is shown in red (thick solid line), and the kSZ from galactic haloes is shown in blue (thick solid line). tSZ from galaxy clusters (Efstathiou & Migliaccio, 2012) is shown in red (thin solid line), the kSZ from galaxy clusters is shown in blue (thin solid line), the radio poisson and CIB poisson signals in green dotted and brown dashed lines, respectively, and CIB clustering signal is shown in brown dot-dashed line. The lensed primary signal is shown in black and the total signal is shown by grey line.

for larger ℓ values. Note that, C_ℓ scales as the square of the fraction of hot gas in galactic haloes, and the plotted values assume the fraction to be 0.11. If the fraction is smaller, the values of C_ℓ for kSZ and tSZ are correspondingly lower. For example, if the hot halo gas constitutes only half of the missing baryons, with a fraction ~ 0.05 (instead of 0.1), then SZ signal from the galactic haloes would dominate at $\ell \gtrsim 30000$ (instead of 10^4).

2.3.6 Mass distribution

We can estimate the range of masses which contribute most to the tSZ and kSZ effects by computing appropriate moments of the mass function, for pressure and peculiar velocity. Figure 2.5 shows the moment of y -parameters for tSZ and kSZ in the top and bottom panels, respectively, for the mass range $10^{10}-10^{13}h^{-1}M_\odot$, corresponding to the l -range $\sim 7 \times 10^4-7 \times 10^3$ for $z = 1$, and l -range $\sim 1.4 \times 10^5-1.4 \times 10^4$ for $z = 4$. The moments of tSZ ($\nu_{\text{tSZ}} \times \frac{dN}{d\log M}$) show that the dominant mass range decreases with increasing redshift, from being $\sim 10^{13} h^{-1} M_\odot$ at $z \sim 1$, to haloes of $\sim 5 \times 10^{11} h^{-1} M_\odot$ at $z \sim 2-3$ to lower masses at higher redshift. From the redshift distribution information in Figure 2.4, we can infer that

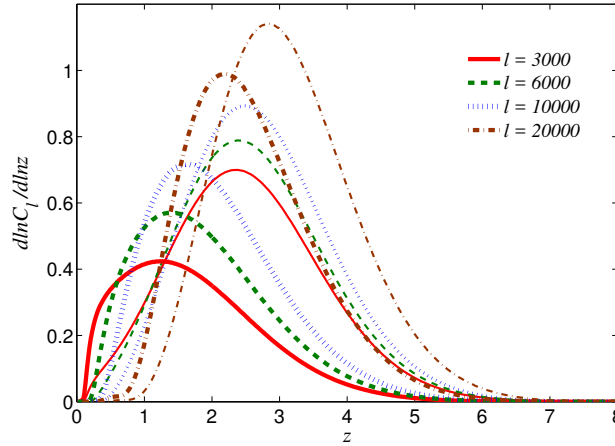


Fig. 2.4 Redshift distribution of tSZ and kSZ effects. tSZ cases are shown with thin lines and kSZ cases, with thick lines for $l = 3000$ (red solid lines), $l = 6000$ (green dashed lines), $l = 10000$ (blue dotted lines) and $l = 20000$ (brown dot-dashed lines).

galactic haloes with mass $\sim 10^{12} h^{-1} M_{\odot}$ are the dominant contributors for $\ell \lesssim 10^4$ for tSZ effect.

The moments of kSZ signal ($y_{\text{kSZ}} \times \frac{dN}{d \log M}$) show that low mass galactic haloes are the major contributors to the signal, and become progressively more important at increasing redshifts. Since, we have constrained the mass range from a cooling time-scale argument, the moments at different redshift show that the dominant mass is $\sim 5 \times 10^{11} h^{-1} M_{\odot}$ for $z \sim 1-3$. Again, from the redshift distribution information in Figure 2.4, this implies that galactic haloes with $\sim 10^{12} h^{-1} M_{\odot}$ are the major contributors, as in the case of tSZ effect. Since significant contribution for tSZ and kSZ comes from low mass haloes, our predictions are sensitive to the assumed lower mass in which the hot halo gas can remain hot until the next merging event.

2.3.7 Dependence of SZ angular power spectrum on cosmological parameters

We also calculate the dependence of SZ angular power spectrum on different cosmological parameters. In Figure 2.6, we plot the dependences of tSZ and kSZ signals on σ_8 , Ω_M , n_s and h with dashed and solid lines, respectively. When one cosmological parameter is varied, others are kept fixed. However, when Ω_M is varied, Ω_{Λ} is also changed to keep $\Omega_M + \Omega_{\Lambda} = 1$.

The dependences of C_l on different cosmological parameters can be fit by a simple power-law relations near the fiducial values of corresponding parameters. For example, we

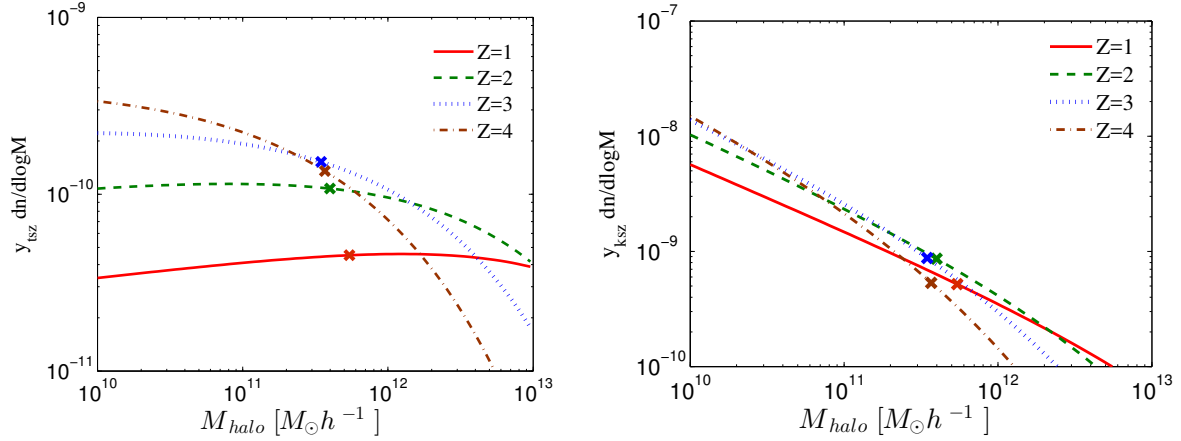


Fig. 2.5 Moments of the mass function for tSZ (top panel) and kSZ (bottom panel), as a function of galactic halo masses, for redshifts $z = 1$ (red solid line), $z = 2$ (green dashed line), $z = 3$ (blue dotted line) and $z = 4$ (brown dot-dashed line). The cross markers on each line show the lower limits of masses considered in the calculations of SZ signal based on the cooling time scale being longer than halo destruction time scale.

find that near the fiducial value of σ_8 , $C_l \propto \sigma_8^6$, which is similar to the dependence of tSZ signal from galaxy clusters (Komatsu & Seljak, 2002). For other parameters, we have, for tSZ, $C_l \propto \Omega_M^3$, $C_l \propto n_s^{7/2}$ and $C_l \propto h^3$ for tSZ. The corresponding dependences for kSZ are: $C_l \propto \sigma_8^5$, $C_l \propto \Omega_M^2$, $C_l \propto n_s$ and $C_l \propto h^2$.

2.4 Detectability in future surveys and constraining gas physics

2.4.1 Integrated Comptonization parameter \tilde{Y}_{500}

Next we estimate the integrated Comptonization parameter for CGM. The Comptonization parameter Y_{500} (due to tSZ) integrated over a sphere of radius R_{500} is

$$Y_{500} = \frac{\sigma_T}{m_e c^2} \int_0^{R_{500}} \frac{P dV}{D_A^2(z)} = \frac{\sigma_T n_e k_b T_e}{m_e c^2 D_A^2(z)} \frac{4\pi R_{500}^3}{3} \quad (2.19)$$

where, $P = n_e k_b T_e$ is pressure of electron gas and R_{500} is defined as the radius within which the mean mass density is 500 times the critical density of the Universe.

The integrated Comptonization parameter, scaled to $z=0$ is defined as,

$$\tilde{Y}_{500} \equiv Y_{500} E^{-2/3}(z) \left(\frac{D_A(z)}{500 M_{pc}} \right)^2. \quad (2.20)$$

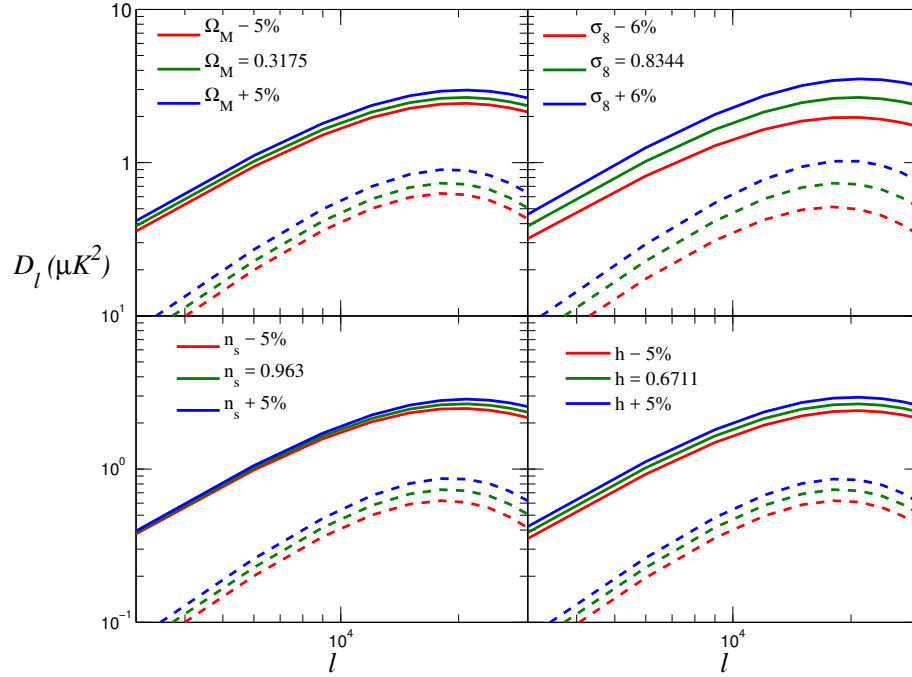


Fig. 2.6 Dependence of SZ angular power spectrum on σ_8 , Ω_M , n_s and h . Here the dashed lines are tSZ effect and the solid lines represent kSZ effect.

Here, \tilde{Y}_{500} and Y_{500} are expressed in square arcmin. We show in Figure 2.7, the values of \tilde{Y}_{500} as a function of halo mass, for gas fractions $f_{rmgas} = 0.11$ and $f_{gas} = 0.05$. We have used the fit for concentration parameter (c) as a function of halo mass from Duffy et al. (2008).

From Table 1 of Planck Collaboration et al. (2013), the lowest stellar mass bin for which SZ signal has been detected ($\tilde{Y}_{500} \sim 10^{-6}$ arcmin²) is $M_* \sim 4 \times 10^{12} M_\odot$. This stellar mass corresponds to a virial mass $\sim 4.25 \times 10^{12} M_\odot h^{-1}$. From our calculations for a galactic halo of $M_{vir} \sim 4.25 \times 10^{12} M_\odot h^{-1}$ with $f_{gas} = 0.11$, the $\tilde{Y}_{500} \sim 0.2\text{--}0.3 \times 10^{-6}$ arcmin², consistent with the observed values (Table 1 of Planck Collaboration et al. 2013). If we use $f_{gas} = 0.05$, \tilde{Y}_{500} goes down by roughly a factor of 2.

2.4.2 Signal to noise ratio in future surveys

The detectability of CMB distortion from circumgalactic baryons can be estimated by calculating the cumulative Signal-to-Noise-Ratio (SNR) of SZ power spectrum for a particular survey. For our purpose, we focus on two types of surveys, one which is an extension of the ongoing SPT survey to higher multipoles (although we show that the SNR from $\ell > 15000$ does not add much to the cumulative SNR), and a more futuristic survey which covers 1000

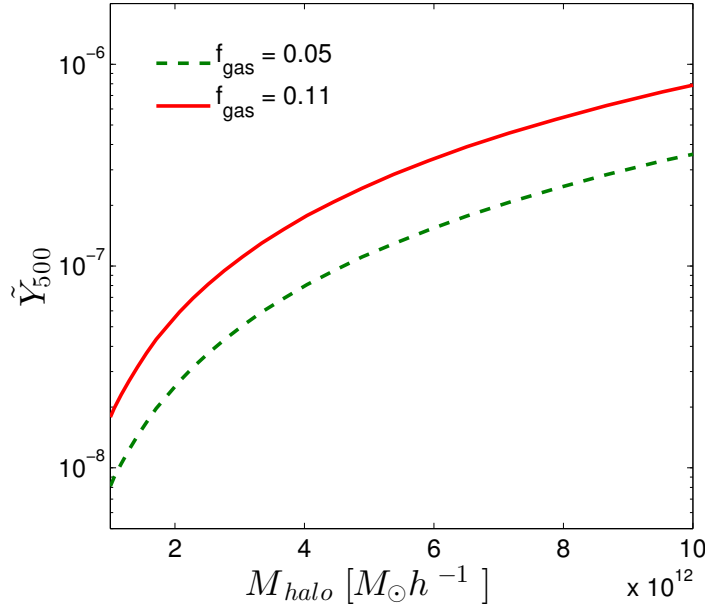


Fig. 2.7 \tilde{Y}_{500} as a function of halo mass (red solid line) for $f_{\text{gas}} = 0.11$ and $f_{\text{gas}} = 0.05$ (green dashed line).

square degrees of the sky (i.e. $f_{\text{sky}} \sim 2\%$) and is cosmic variance limited. These are labeled ‘SPT-like’ and ‘CV1000’, respectively, for the rest of the chapter.

(1) SPT-like survey: In this case we use $\ell_{\text{min}} = 3000$ and $\ell_{\text{max}} = 30000$. The noise in the measurement of C_ℓ ’s (i.e. ΔC_ℓ) is taken from actual SPT data (Figure 4 of Addison, Dunkley & Spergel 2012). These errors are then fitted with a power-law dependence on ℓ , and extrapolated till $\ell = 30000$.

(2) CV1000 survey: This survey has 2% sky coverage and errors on C_ℓ ’s are cosmic variance limited. Here, we have used a smaller ℓ -range, and taken $\ell_{\text{min}} = 6000$ and $\ell_{\text{max}} = 9000$.

The cumulative SNR, for SZ C_ℓ between ℓ_{min} and ℓ_{max} , is given by

$$\text{SNR}_{\text{cumu}}(\ell_{\text{min}} < \ell_{\text{max}}) = \left(\sum_{\ell_{\text{min}}}^{\ell_{\text{max}}} \mathbf{C}_\ell^X (\mathbf{M}_{\ell\ell'}^X)^{-1} \mathbf{C}_{\ell'}^X \right)^{1/2} \quad (2.21)$$

where X denotes cases tSZ, kSZ or Total, i.e tSZ+kSZ and $\mathbf{M}_{\ell\ell'}^X$ is the corresponding covariance matrix, for any particular survey, given by

$$\mathbf{M}_{\ell\ell'}^X = \frac{1}{4\pi f_{\text{sky}}} \left(\frac{4\pi(C_\ell^X + N_\ell)^2}{(\ell + 1/2)\Delta\ell} \delta_{\ell\ell'} + \mathbf{T}_{\ell\ell'}^X \right), \quad (2.22)$$

Table 2.1 Fiducial values and priors on the parameters

Parameter	Fiducial value	Prior-1	Prior-2	Prior-3
σ_8	0.8344	0.027	0.027	0.027
Ω_M	0.3175	0.020	0.020	0.020
n_s	0.963	0.0094	0.0094	0.0094
h	0.6711	0.014	0.014	0.014
f_{ratio}	1.0	-	1.0	1.0
f_{Temp}	1.0	-	-	0.25
f_{gas}	0.11	-	-	-
α_{gas}	0.0	-	-	-

where, N_ℓ is the noise power spectrum (after foreground removal) and $T_{\ell\ell'}^X$ is the SZ angular tri-spectrum (see, e.g., Komatsu & Kitayama 1999). Note that, this formula for the covariance matrix neglects the ‘halo sample variance’.

The cumulative SNR provides a simple way to assess the constraining power of a given experiment irrespective of the constraints on particular parameters. We compute the cumulative SNR’s for our two surveys, SPT-like and CV1000 surveys. Figure 2.8 shows the SNR as a function of ℓ_{max} for the SPT-like survey. Note that, the covariance matrix in Equation 2.21, in principle, should include all contributions from cosmic variance (Gaussian and non-Gaussian), experimental noise after foreground removal, as well as the tri-spectrum, which represents the sample variance contribution to the covariance. However, for the halo masses and ℓ range of interest, the tri-spectrum can be neglected and the covariance matrices are, effectively, diagonal. For the CV1000 survey, the diagonal covariance matrix only contains the cosmic variance errors. The covariance matrix, for the SPT-like survey, is taken to be the noise (actual error bar) reported by the SPT and extrapolated to higher ℓ ’s (as explained earlier). In general, our extrapolation of SPT errors to higher ℓ -values are conservative in nature as seen in Figure 2.8 due to the increasing observational errors for higher multipoles, the SNR for the SPT-like survey flattens off beyond $\ell_{\text{max}} \sim 15000$. It is also evident from this figure that it would need a stringent handle on astrophysical systematics and better modelling of SZ C_ℓ from galaxy clusters to separate out the tSZ C_ℓ from CGM. kSZ signal from CGM has a signal to noise ratio $\sim 2\sigma$ for the SPT-like survey. If we take $\ell_{\text{min}} = 10000$ for SPT-like survey, the signal to noise ratio goes down roughly by a factor of 2. In comparison, for the more futuristic CV1000 survey, the tSZ and kSZ signal can be detected with a SNR of $\sim 600(950)$, at (upto) $\ell_{\text{max}} \sim 6000(9000)$.

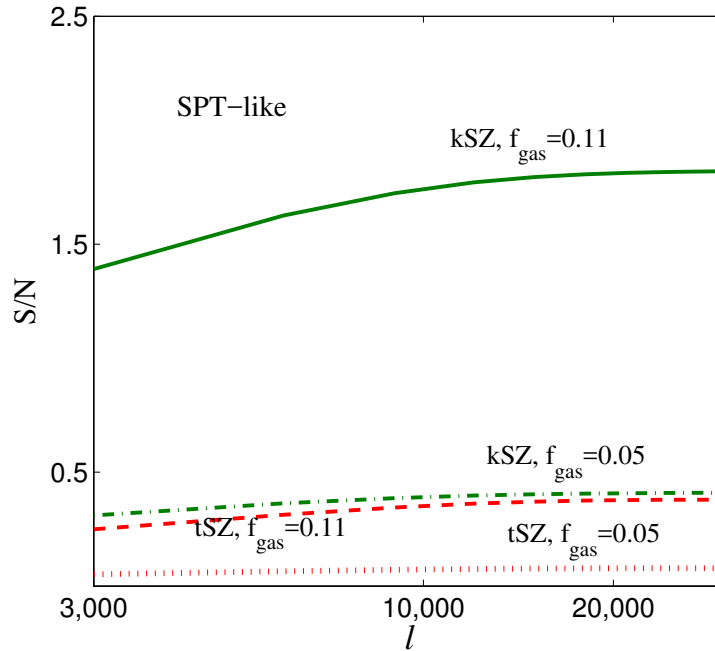


Fig. 2.8 The cumulative signal to noise ratio (SNR) as a function of ℓ_{\max} , in case of SPT-like survey, with $\ell_{\min} = 3000$. The upper line corresponds to kSZ and the lower line to tSZ. The solid (green) and dashed (red) lines corresponds to kSZ and tSZ for $f_{\text{gas}} = 0.11$, respectively, and the dot-dashed (green) and dotted (red) lines, for $f_{\text{gas}} = 0.05$.

2.5 Forecasting

2.5.1 Formalism

We now employ the Fisher matrix formalism to forecast the expected constraints on following parameters, focussing specially on the parameters related to gas physics of the circumgalactic baryons. The Fisher parameters considered are

$$\{[\sigma_8, \Omega_M, n_s, h], [f_{\text{gas}}, f_{\text{ratio}}, f_{\text{Temp}}, \alpha_{\text{gas}}]\} , \quad (2.23)$$

where, the first set within the parenthesis are the cosmological parameters and the second set, which depends on baryonic physics, are the *astrophysical* parameters.

To construct Fisher Matrices for the two surveys, we compute the derivatives of tSZ, kSZ and, hence, total SZ C_ℓ with respect to each parameter around the fiducial values listed in Table 1. Here, f_{gas} is the redshift independent fraction of halo mass in gaseous form and α_{gas} captures any possible evolution of the gas defined through $f_{\text{gas}}(z) = f_{\text{gas}}[E(z)]^{\alpha_{\text{gas}}}$.

Table 2.2 Error on parameters for different surveys and Prior cases with fixed α_{gas}

Parameters	CV1000 , P1	CV1000 , P2	CV1000 , P3	SPT-like , P1	SPT-like , P2	SPT-like , P3
$\Delta\sigma_8$	0.0166	0.0163	0.0162	0.0270	0.0270	0.0270
$\Delta\Omega_M$	0.0163	0.0161	0.0161	0.020	0.020	0.020
Δn_s	0.0093	0.0093	0.0093	0.0094	0.0094	0.0094
Δh	0.0139	0.0139	0.0139	0.0140	0.0140	0.0140
Δf_{ratio}	0.2329	0.2268	0.2266	18.7380	0.9986	0.9982
Δf_{Temp}	0.0312	0.0311	0.0309	1.6547	1.4826	0.2465
Δf_{gas}	0.0023	0.0023	0.0023	0.1119	0.0433	0.0366

Our fiducial model assumes no evolution of the gas fraction; see details in Section 2.5.2. The other two parameters that encapsulate the uncertainty in our knowledge of hot gas in galactic haloes are $f_{\text{ratio}} = \frac{t_{\text{cool}}}{t_{\text{dest}}}$, the ratio of cooling time to destruction time for galactic haloes, $f_{\text{Temp}} = \frac{T}{T_{\text{vir}}}$, the ratio of the temperature of the gas to the virial temperature of gas in a halo.

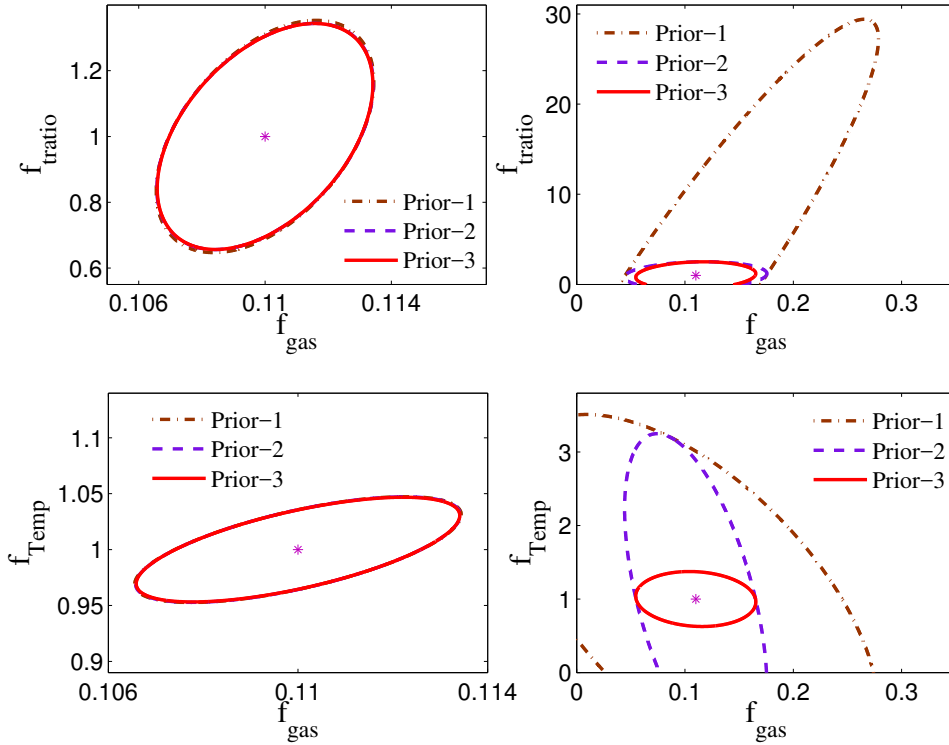


Fig. 2.9 $1-\sigma$ contours for gas physics parameters $f_{\text{gas}}, f_{\text{ratio}}, f_{\text{Temp}}$ when α_{gas} is fixed. The left panel is for CV1000 survey and the right panel is for SPT-like survey. In all cases red solid line is Prior-3, purple dashed line is Prior-2 and brown dot-dashed line is Prior-1.

For a given fiducial model, the Fisher matrix is written as

$$F_{ij} = \frac{\partial C_\ell^X}{\partial p_i} (M_{\ell\ell'}^X)^{-1} \frac{\partial C_{\ell'}^X}{\partial p_j} \quad (2.24)$$

where, $M_{\ell\ell'}$ is given by Equation 2.22 in case of CV1000 survey and for SPT-like survey we have $M_{\ell\ell'} = (\Delta C_\ell^{\text{SPT}})^2$. Here, $\Delta C_\ell^{\text{SPT}}$'s are the error on C_ℓ 's from SPT data. The fiducial values and priors used are listed in Table 2.1. Note that in all our calculations, cosmological priors are always applied. Priors related to gas/halo physics are additionally applied, on a case by case basis. For rest of the chapter, we denote different priors uses as follows:

Prior-1 : Priors on cosmological parameters only.

Prior-2 : Priors on cosmological parameters + 100% prior on f_{ratio} .

Prior-3 : Priors on cosmological parameters + 100% prior on f_{ratio} + 25% prior on f_{Temp} .

In Prior-3 and Prior-2 , we have assumed a 100% prior on f_{ratio} , reflecting the maximum uncertainty in this parameter. For f_{Temp} , we have assumed a smaller uncertainty, since our constraint that cooling time is longer than the destruction time ensures that the gas temperature to be close to the virial temperature.

Additionally, for each case considered, we look at constraints for all eight parameters listed above (Equation 2.23), and in the second case, we repeat the same procedure but with only 7 parameters, assuming that the baryonic content of galaxies is independent of redshift (i.e. $\alpha_{\text{gas}} = 0$). The introduction of varying gas fraction in haloes changes the shape of C_ℓ (see, for example, in Majumdar 2001) which results in different sensitivity to the Fisher parameters; it also introduces an extra nuisance parameter to be marginalised over. The results of the first analysis (with α_{gas} varying) are shown in Table 3 and the second case (with α_{gas} fixed) in Table 2.

2.5.2 Results

We are in an era in cosmology where major surveys like *Planck* have already provided tight constraints on the parameters of standard cosmological model. In the future, two of the major goals are to go beyond the standard model of cosmology and to constrain parameters related to baryonic/gas physics associated with non-linear structures. One of the puzzles related to baryonic matter is the issue of 'missing baryons', i.e the fact that after accounting for the gas locked up in structures (like galaxies and galaxy clusters) and the diffuse IGM, one still falls short of the cosmological mean baryon fraction Ω_B . While recently, much of

this missing material may have been accounted by the intra-cluster medium, a deficit of the order of at least $\sim 10\%$ is still found.

With the growing observational evidence for CGM, it would be interesting to determine if its inclusion in the baryon census can fill the deficit. To go forward, one needs to go beyond the discovery of CGM in nearby isolated haloes (other than the Milky Way) or beyond what one can measure by doing a stacking analysis of gas in a sample of haloes. This is possible by probing the locked gas in and around a cosmological distribution of galaxy haloes through its signature on the CMB as shown in this chapter. A constraint on the mean gas fraction, f_{gas} , included in our calculations, provides one of the best ways to estimate the amount of circumgalactic baryons in a statistical sense. In rest of the section, we focus on the constraints on f_{gas} , for a variety of survey scenarios.

Table 2.3 Error on parameters for different surveys and Prior cases

Parameters	CV1000 , P1	CV1000 , P2	CV1000 , P3	SPT-like , P1	SPT-like , P2	SPT-like , P3
$\Delta\sigma_8$	0.0270	0.0263	0.0261	0.0270	0.0270	0.0270
$\Delta\Omega_M$	0.020	0.0187	0.0187	0.020	0.020	0.020
Δn_s	0.0094	0.0094	0.0094	0.0094	0.0094	0.0094
Δh	0.0140	0.0140	0.0140	0.0140	0.0140	0.0140
Δf_{ratio}	0.5192	0.4608	0.4598	33.393	0.9995	0.9984
Δf_{Temp}	0.0405	0.0396	0.0392	3.6606	1.9240	0.2479
Δf_{gas}	0.0038	0.0035	0.0035	0.1687	0.1619	0.1404
$\Delta\alpha_{\text{gas}}$	0.1052	0.0958	0.0954	4.0753	2.2890	1.7734

The constraints on the amount of baryons locked up as CGM, as well on other Fisher parameters, are shown in Tables 2.2 & 2.3. The 1σ ellipses for joint constraints of f_{gas} with non-cosmological parameters, for the two surveys considered and different prior choices, are shown in Figures 2.9 – 2.12.

Constraints on CGM using using kSZ + tSZ

Strong degeneracies between the astrophysical parameters prevent us from getting any useful constraints on the CGM, using *only* cosmological priors i.e Prior-1, when one uses either of the tSZ or the kSZ C_ℓ alone. However, once both the tSZ and the kSZ signals are added, the strong degeneracies are broken. This is seen clearly in the upper left panel of Figure 2.10, which shows the joint constraint for the SPT-like survey. The fact that two cigar-like degeneracies, from two datasets, differing in their degeneracy directions eventually leads to very strong constraints in parameter space when taken together, is well known (see, for example, Khedekar, Majumdar & Das 2010) and the same idea is at work here. Although there is practically no constraint on f_{gas} from using tSZ or kSZ C_ℓ from CGM individually, adding them together results in a weak constraint of $\Delta f_{\text{gas}} \approx 0.11$, which is the same as the

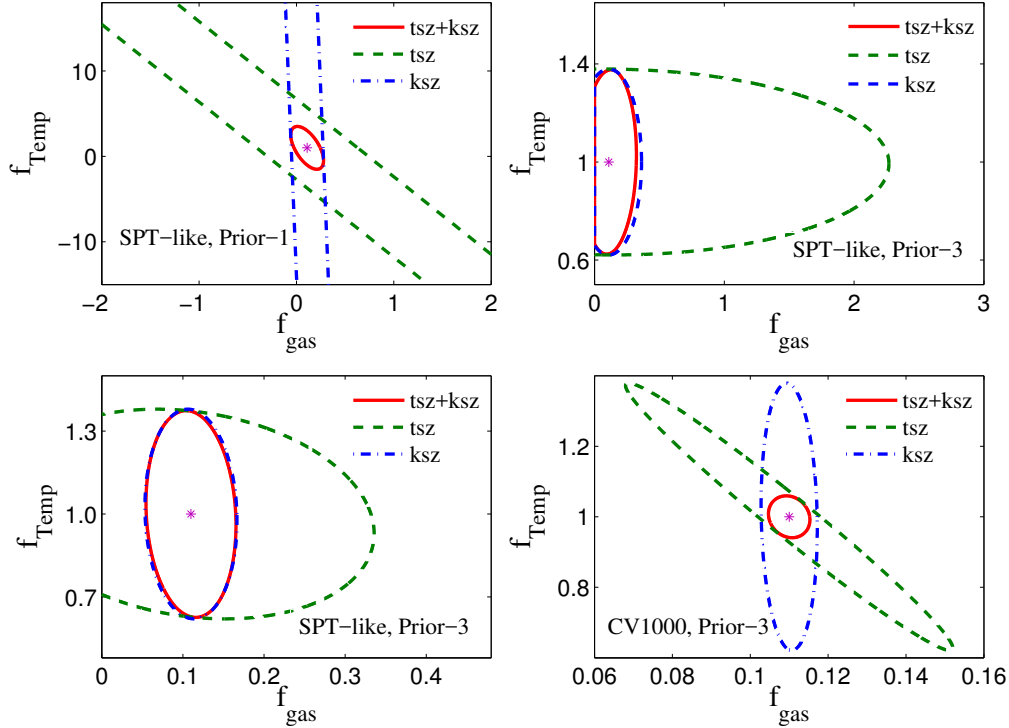


Fig. 2.10 The figure shows the breaking of parameter degeneracy when information from tSZ C_ℓ and kSZ C_ℓ are taken together for different cases. The Upper Left panel shows result from the case Prior-1, i.e., cosmological priors only, for the SPT-like survey even when α is fixed. The Upper Right panel shows the case Prior-3 which includes additional priors on f_{ratio} and f_{Temp} but α , now, varied for SPT-like. The Lower Left panel shows the case Prior-3 but with α fixed. The Lower Right panel shows the case for CV1000 for, with Prior-3 and α varied. In all cases, green dashed line is tSZ, blue dot-dashed is kSZ and solid red line is tSZ+kSZ.

fiducial value of f_{gas} . One reason for this weak constraint is the additional degeneracy of f_{gas} with α .

This degeneracy of f_{gas} with α is broken either (i) when one evokes no evolution in the Fisher analysis or (ii) when additional astrophysical priors are imposed. This is shown in the upper right and lower left panels of Figure 2.10. In both cases, the addition of astrophysical priors, for example Prior-3, can already break the strong cigar like degeneracies leaving both kSZ and tSZ signal power to constrain f_{gas} . The difference between these two panels is that α is not fixed (i.e we marginalise over unknown evolution) for the upper right panel leading to slightly weaker constraints (for tSZ+kSZ) than the lower left panel, where, α is held constant. The higher SNR of kSZ w.r.t tSZ (as seen in Figure 2.8) gives the kSZ C_ℓ a stronger constraining power on f_{gas} than tSZ, and the addition of tSZ C_ℓ makes only modest improvement on the constraint on CGM achieved by using kSZ C_ℓ only.

The lower right panel of Figure 2.10 shows that constraints from a more futuristic cosmic variance limited survey CV1000 in the presence of Prior-3 but including an unknown gas fraction. In this case, due to its better sensitivity, tSZ is capable of constraining f_{gas} (compare green dashed ellipses in the two right panels, upper and lower) and finally comes up with stronger joint constraint than SPT-like (compare the red solid ellipse in lower left and lower right). In rest of this section, we focus mainly on constraints coming from kSZ+tSZ C_ℓ , keeping in mind that all the constraints will only be slightly degraded if only kSZ C_ℓ are used instead. Note that, this is applicable as long as astrophysical priors are added.

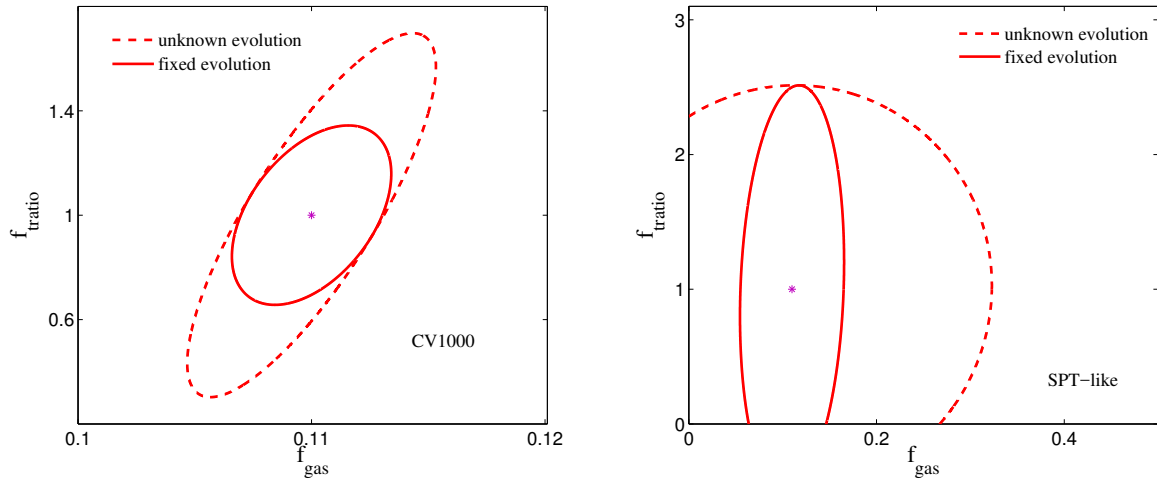


Fig. 2.11 The figure shows the impact on parameter constraints due to any unknown evolution of the gas fraction with redshift parametrised as $f_{\text{gas}}(z) = f_{\text{gas}}[E(z)]^{\alpha_{\text{gas}}}$. The Left Panel is for the survey 'CV1000' and Right Panel is for the survey 'SPT-like'. In both cases, the red dashed line corresponds to the case of α_{gas} is unknown and varied as one of the Fisher parameters, whereas the red solid line correspond to α_{gas} fixed at its fiducial value.

As evident above, one of the major uncertainties in our knowledge of the gas content of haloes at all scales is our lack of understanding of any redshift evolution of the gas. In using large-scale structure data to constrain cosmology, for example, an unknown redshift evolution can seriously degrade cosmological constraints (as an example, see Majumdar & Mohr 2003) and one needs to invoke novel ideas to improve constraints (Majumdar & Mohr, 2004; Khedekar & Majumdar, 2013). Whereas for galaxy clusters, in which case f_{gas} has been measured at higher redshift, and one finds evolution in gas content, no such evolution has been measured for galactic haloes considered in this work. It is however possible that feedback processes in galaxies, and cosmological infall of matter may introduce an evolution of f_{gas} with redshift. In order to incorporate the impact of gas evolution on our

constraints, we have considered the possibility that f_{gas} scales with the expansion history $E(z)$ with a power-law index α , with the fiducial value of α set to 0.

The constraints on all the parameters used in the Fisher analysis for the cases where we assume the gas fraction to remain constant, are given in Table 2.2. As mentioned before, in the absence of any astrophysical priors, there are no interesting constraints on f_{gas} (as well as f_{Temp} or f_{ratio}) for SPT-like survey. However, for the CV1000 survey the amount of gas locked as CGM can be constrained very tightly to better than 2%; similarly, with cosmological priors only, CV1000 can constrain departure from the virial temperature to 3.1% and f_{ratio} to $\sim 23\%$. The addition of astrophysical priors, either Prior-2 or Prior-3 does not improve the constraints for CV1000 any further, since the constraints with Prior-1 are much tighter than the priors imposed. However, astrophysical priors considerably improve the constraints for the SPT-like survey especially for f_{gas} which is constrained to 39% when Prior-2 is used and is further constrained to better than 33% accuracy with Prior-3. This means that for both Prior-2 and Prior-3, $f_{\text{gas}}=0$ can be excluded by at least 3σ with the SPT-like survey.

The corresponding constraint ellipses showing the 1σ allowed region between f_{gas} and either f_{Temp} or f_{ratio} are shown in Figure 2.9. The left panels show the degeneracy ellipses for CV1000 whereas the right panels show the same for SPT-like. Notice, from the upper panels that f_{ratio} has a positive correlation with f_{gas} . This can be understood by noting that any increase in f_{gas} increases C_ℓ , whereas, it can be offset by an increase f_{ratio} which pushes up the lower limit of halo mass (see Figure 2.1) and hence decreases the number density of haloes thus lowering the C_ℓ . The anti-correlation of f_{gas} with f_{Temp} , seen in the lower right panel, is a consequence of the anti-correlation of n_e and T_v (in Equation 2.1) in the tSZ relation which modulates the overall degeneracy direction of tSZ+kSZ. Note that, for the CV1000 survey, the 1σ ellipses are almost degenerate whereas priors shape the relative areas of the ellipses for the SPT-like survey.

A fixed non-evolving f_{gas} , although desirable, is rather naive. Given our lack of understanding of the energetics affecting the CGM over cosmic time scales, it is prudent to marginalise over any unknown evolution of f_{gas} parametrised, here, by α . The resultant constraints are given in Table 2.3. The presence over one extra unknown gas evolution parameter to marginalise over, dilutes the constraints on f_{gas} for both the surveys. For CV1000 survey, the constraints are still strong and hovers around 3% for all three prior choices. Moreover, f_{Temp} and f_{ratio} can be still be constrained to $\sim 4\%$ and $\sim 46\%$ by the futuristic survey. Without any external prior on α , all parameters poorly constrained by the SPT-like survey. With CV1000 survey, one can get a much stringent constraint on any possible evolution of the CGM with $\Delta\alpha \sim 0.1$

Constraints on Cosmology

The parameters of the standard cosmological model are already tightly constrained by *Planck*. These are the constraints that are used as Prior-1 in this chapter. With the SNR achievable in a SPT-like survey, it is not possible to tighten the cosmological constraints further irrespective of whether we know α or it is marginalized over. However, with the larger sensitivity of CV1000 survey, it is possible to further improve cosmological parameters, albeit with α fixed. A quick look at Table 2.2 shows that it is possible to shrink the 1σ error on σ_8 by almost a factor of 2 and that on Ω_M by $\sim 20\%$.

Constraints on the density profile of CGM

We have so far assumed the density profile of CGM to be uniform, which was argued on basis of current observations (Putman, Peek & Joung, 2012; Gatto et al., 2013). However, it is perhaps more realistic to assume that the density profile decreases at large galacto-centric distances. One can ask if it would be possible to determine the pressure profile of the halo gas from SZ observations in the near future. In order to investigate this, we parameterise the density profile by γ_{gas} such that $\rho_{\text{gas}}(r) \propto (1 + (r/R_s)^{\gamma_{\text{gas}}})^{-1}$, where R_s is the scale radius defined as $R_s \equiv R_{\text{vir}}/c(M, z)$ and $c(M, z)$ is the concentration parameter. This density profile gives uniform density at $r \ll R_s$ and $\rho_{\text{gas}}(r) \propto r^{-\gamma_{\text{gas}}}$ at $r \gg R_s$. We include γ_{gas} in the Fisher matrix analysis with fiducial value $\gamma_{\text{gas}} = 0$. For CV1000 survey with a fixed α_{gas} and Prior-3, the constrain on density profile of CGM is $\gamma_{\text{gas}} < 1.5$ whereas the constrain degrades to $\gamma_{\text{gas}} < 3.15$ in the presence of an unknown redshift evolution of gas fraction. γ_{gas} poorly constrained by SPT-like survey.

2.6 SZ effect from warm CGM

The observations of Tumlinson et al. (2011) have shown the existence of OVI absorbing clouds, at $10^{5.5}$ K, with hydrogen column density $N_{\text{H}} \sim 10^{19-20} \text{ cm}^{-2}$. The integrated pressure from this component in the galactic halo is estimated as $\langle p \rangle \sim N_{\text{H}} k T$. This implies a tSZ y -distortion of order $y_{\text{OVI}} \sim N_{\text{H}} k T \sigma_{\text{T}} / (m_e c^2) \sim 3.6 \times 10^{-9} N_{\text{H},20}$, where $N_{\text{H}} = 10^{20} N_{\text{H},20} \text{ cm}^{-2}$.

There is also a cooler component of CGM, at $\sim 10^4$ K, which is likely to be in pressure equilibrium with the warm CGM. The COS-Halos survey have shown that a substantial fraction of the CGM can be in the form of cold ($\sim 10^4$ K). Together with the warm OVI

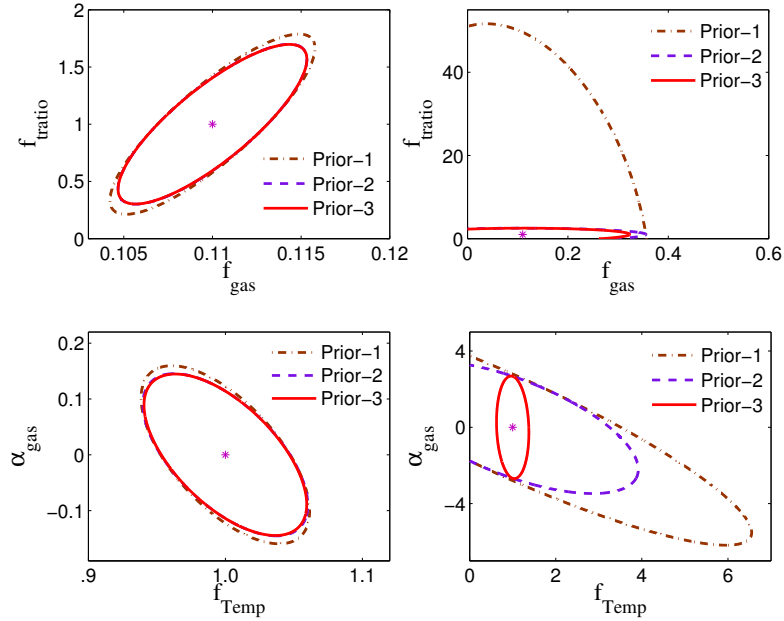


Fig. 2.12 $1\text{-}\sigma$ contours for gas physics parameters f_{gas} , f_{ratio} , f_{Temp} , α_{gas} . The left panel is for CV1000 survey and the right panel is for SPT-like survey. In all cases red solid line is Prior-3, purple dashed line is Prior-2 and brown dot-dashed line is Prior-1.

absorbing component, this phase can constitute more than half the missing baryons (Werk et al., 2014). Simulations of the interactions of galactic outflows with halo gas in Milky Way type galaxies also show that the interaction zone suffers from various instabilities, and forms clumps of gas at 10^4 K (Marinacci et al., 2010; Sharma et al., 2014a). These are possible candidates of clouds observed with NaI or MgII absorptions in galactic haloes. Cross-correlating MgII absorbers with SDSS, WISE and GALEX surveys, Lan, Ménard & Zhu (2014) have concluded that some of the cold MgII absorbers are likely associated with outflowing material. However, for similar column density of these clouds, the SZ signal would be less than that of the warm components by $10^{-1.5}$ because of the temperature factor.

We can calculate the integrated y -distortion due to the CGM in intervening galaxies, by estimating the average number of galaxies in the appropriate mass range ($10^{12-13} M_{\odot}$) in a typical line of sight, using Monte-Carlo simulations. Dividing a randomly chosen line-of-sight, we divide it in redshift bins up to $z = 8$, and each redshift bin is then populated with haloes using the Sheth-Tormen mass function, in the above mentioned mass range. We estimate the average number to be ~ 20 after averaging over 50 realisations. This implies an integrated y -parameter of order $7.5 \times 10^{-8} N_{\text{H},20}$. This can be detected with upcoming experiments such as Primordial Inflation Explorer (*PIXIE*) even with $N_{\text{H}} = 10^{19} \text{ cm}^{-2}$, since it aims to detect spectral distortion down to $y \geq 2 \times 10^{-9}$ Kogut et al. (2011).

The kSZ signal from the warm gas in galactic haloes can be estimated from Equation 2.3, writing v_{local} as the local (line of sight) velocity dispersion. Recent studies indicate that CGM gas is likely turbulent, probably driven by the gas outflows (Evoli & Ferrara, 2011). If we consider transonic turbulence for this gas, then $v_{\text{los}}/c \sim \sqrt{kT/m_p c^2}$. Then we have,

$$\frac{\Delta T_{\text{kin}}}{\Delta T_{\text{th}}} \approx \frac{1}{2} \frac{m_e}{m_p} \sqrt{\frac{m_p c^2}{k_b T_e}} = \frac{m_e}{2m_p} \frac{c}{v_{\text{loc}}}. \quad (2.25)$$

For $v_{\text{loc}} \sim 100 \text{ km s}^{-1}$ (corresponding to gas with temperature $\sim 10^6 \text{ K}$), the kSZ signal from turbulent gas is, therefore, comparable to the tSZ signal.

2.7 Conclusions

We have calculated the SZ distortion from galactic haloes containing warm and hot circumgalactic gas. For the hot halo gas, we have calculated the angular power spectrum of the distortion caused by haloes in which the gas cooling time is longer than the halo destruction time-scale (galactic haloes in the mass range of $5 \times 10^{11} - 10^{13} h^{-1} M_{\odot}$). The SZ distortion signal is shown to be significant at small angular scales ($\ell \sim 10^4$), and larger than the signal from galaxy clusters. The kSZ signal is found to dominate over the tSZ signal for galactic haloes, and also over the tSZ signal from galaxy clusters for $\ell > 10000$. We also show that the estimated Comptonization parameter \tilde{Y}_{500} for most massive galaxies (halo mass $\geq 10^{12.5} M_{\odot}$) is consistent with the marginal detection by *Planck*. The integrated Compton distortion from the warm CGM is estimated to be $y \sim 10^{-8}$, within the capabilities of future experiments.

Finally, we have investigated the detectability of the SZ signal for two surveys, one which is a simple extension of the SPT survey that we call SPT-like and a more futuristic cosmic variance limited survey termed CV1000. We find that for the SPT-like survey, kSZ from CGM has a SNR of $\sim 2\sigma$ and at much higher SNR for the CV1000 survey. We do a Fisher analysis to assess the capability of these surveys to constrain the amount of CGM. Marginalizing over cosmological parameters, with *Planck* priors, and astrophysical parameters affecting the SZ C_{ℓ} from CGM, we find that in the absence of any redshift evolution of the gas fraction, the SPT-like survey can constrain f_{gas} to $\sim 33\%$, and the CV1000 survey, to $\sim 2\%$. Solving simultaneously for an unknown evolution of the gas fraction, the resultant constraints for CV1000 becomes 3% and it is poorly constrained by SPT-like survey. We also find that a survey like CV1000 can improve cosmological errors on σ_8 obtained by *Planck* by a factor of 2, if one has knowledge of the gas evolution. The Fisher analysis tells

us that if indeed $\sim 10\%$ of the halo mass is in the CGM, then this fraction can be measured with sufficient precision and can be included in the baryonic census of our Universe.

Chapter 3

Probing the circumgalactic baryons through cross-correlations

Based on:

Singh, P., Majumdar, S., Nath, B. B., Refregier, A., Silk, J. 2016, MNRAS, 456, 1495

We study the cross-correlation of distribution of galaxies, the SZ and X-ray power spectra of galaxies, from current and upcoming surveys and show these to be excellent probes of the nature, i.e. extent, evolution and energetics, of the CGM. We forecast the detectability of the cross-correlated galaxy distribution, SZ and X-ray signals by combining SPT-DES and eROSITA-DES/eROSITA-LSST surveys, respectively. Finally, we demonstrate that the cross-correlated SZ-galaxy and X-ray-galaxy power spectrum can be used as powerful probes of the CGM energetics and potentially discriminate between different feedback models recently proposed in the literature

Main Results

- The SZ-galaxy cross-power spectrum, especially at large multipoles, depends on the steepness of the pressure profile of the CGM. This property of the SZ signal can, thus, be used to constrain the pressure profile of the CGM.
- The X-ray cross power spectrum also has a similar shape. However, it is much more sensitive to the underlying density profile.
- We find that, for the SPT-DES survey, the signal-to-noise ratio (SNR) peaks at high mass and redshift with $\text{SNR} \sim 9$ around $M_h \sim 10^{13} h^{-1} M_\odot$ and $z \sim 1.5\text{--}2$ for flat density and temperature profiles.
- The SNR peaks at $\sim 6(12)$ for the eROSITA-DES (eROSITA-LSST) surveys. We also perform a Fisher matrix analysis to find the constraint on the gas fraction in the CGM in the presence or absence of an unknown redshift evolution of the gas fraction.
- One can distinguish a ‘no AGN feedback’ scenario from a CGM energized by ‘fixed-velocity hot winds’ at greater than 3σ using above cross-correlation signals.

3.1 Introduction

The standard scenario of galaxy formation predicts that the amount of baryons in a galactic halo should approximately be a constant fraction ($\sim 16\%$) of the total halo mass (dark matter + baryonic matter). This baryon-to-total halo mass fraction is known as the cosmic baryon fraction (CBF). As discussed in Chapter 1, observations have detected only a small fraction of this CBF. More than half of the baryons of CBF are missing from the galaxies according to soft x-ray absorption line (Anderson & Bregman, 2010) and emission line searches (Miller & Bregman, 2015) in galactic haloes. This is an important problem for all galaxy formation studies, for with more than 50% of the baryon reservoir unaccounted for, the sources and sinks for forming stars become correspondingly uncertain. Recent detection of substantial amounts of cooler gas within the halo virial radius fails to significantly alleviate this problem (Werk et al., 2014).

There are recent observations which indicate the presence of significant amounts of hot coronal gas extended over a large region around massive spiral galaxies (Anderson & Bregman, 2011; Dai et al., 2012; Anderson, Bregman & Dai, 2013; Bogdán et al., 2013b,a). This gas, known as the CGM, may account for some of the missing baryons from the galaxies. The CGM is the gas surrounding the central, optically visible part of the galaxy within its host dark matter halo. This is the bridging medium that connects the ISM to the IGM. During galactic evolution, the galaxy accretes matter from its surrounding IGM and also ejects some material in the form of galactic winds resulting from feedback processes like SNe and AGN. The CGM, being the intermediate medium, is most affected by these processes and may contain important clues about galaxy evolution, making it a promising tool for the study of the processes affecting the galaxy evolution.

In the previous chapter, we have estimated the SZ distortion of CMBR due to the presence of hot CGM surrounding massive galaxies. The tSZ distortion of CMBR due to the CGM is small compared to the tSZ distortion caused by galaxy clusters (Planck Collaboration et al., 2013; Singh et al., 2015). The detectability of tSZ signal from a system can be enhanced by cross-correlating this signal with another signal originating from the same source like the distribution of haloes (Fang, Kadota & Takada, 2012) or the gravitational lensing (Van Waerbeke, Hinshaw & Murray, 2014; Ma et al., 2015). We cross-correlate the tSZ signal from the CGM with the distribution of the galaxies. The cross-power spectrum between the SZ signal and distribution of galaxies can be thought of as the SZ-galaxy cross power spectrum. It can be obtained by combining a high resolution a CMB survey such as SPT with an overlapping optical survey.

In addition to the SZ-effect, the hot CGM also manifests itself in X-ray emission through bremsstrahlung. Combining the X-ray observations with optically selected galaxies can

give the X-ray-galaxy cross power spectrum, which enhances the detectability of the X-ray emitting gas. The X-ray emission from the CGM is more sensitive to the underlying gas distribution than the SZ effect and it also breaks the degeneracy between the gas density and temperature which is present in the SZ effect. In this chapter, we study the prospects for the cross-correlation of the soft X-ray emission from the CGM with the distribution of galaxies. This can be used as an additional probe to constrain the properties of the CGM.

We also compute the X-ray-SZ cross-power spectrum for the CGM. Significant effort has been made to forecast/detect the X-ray-SZ cross-correlation on large scales by cross-correlating the CMB maps generated by WMAP (Wilkinson Microwave Anisotropy Probe) and/or *Planck* surveys with the ROSAT (Röntgen Satellite) all sky survey (Diego, Silk & Sliwa, 2003; Hernández-Monteagudo, Genova-Santos & Atrio-Barandela, 2004; Hernández-Monteagudo et al., 2006; Hinshaw et al., 2007; Hajian et al., 2013). The X-ray-SZ cross-correlation measured for the galaxy clusters is particularly useful to constrain the cosmological parameters as the number of clusters strongly depends on the underlying cosmology (Hurier, Aghanim & Douspis, 2014; Hurier et al., 2015). We look into the possibility of detecting the contribution of the CGM to the X-ray-SZ cross-power spectrum with SPT and eROSITA (extended ROentgen Survey with an Imaging Telescope Array) combination.

Simulations suggest that feedback processes are required to avoid the over-cooling problem and formation of excessively massive galaxies (in terms of stellar mass). A number of feedback mechanisms have been proposed that reproduce many observed galaxy properties despite having different implementations and physical motivations behind them. The CGM, thus can provide additional constraints on these simulations as the CGM properties are largely affected by the variation in the feedback mechanism (Suresh et al., 2015)

This chapter is organized as follows: In Section 3.2 we describe the SZ-effect. In Section 3.3 we estimate the cross-correlation between the SZ-effect from the hot CGM and the distribution of galaxies and forecast the detectability of the SZ-galaxy cross power spectrum. In Section 3.4 we describe the X-ray emission from the hot CGM and forecast the detectability of X-ray-galaxy cross power spectrum. In Section 3.5 we compute the X-ray-SZ cross power spectrum. In Section 3.6 we forecast the constraints on the CGM properties. In Section 3.7 we discuss the possibility of differentiating between various feedback models. In Section 3.8 we conclude by summarizing our main results.

3.2 SZ distortion from hot galactic halo gas

For simplicity, we assume that the mass fraction of the CGM is independent of the host halo mass. Observations indicate that the fractional mass in the stellar component of galaxies is

~ 0.05 (Mo, Mao & White, 1998; Moster et al., 2010; Leauthaud et al., 2012; Dutton et al., 2010). This corresponds to a fractional mass in gas, $f_{\text{gas}} = 0.11$, as the total fractional mass in baryons in a galaxy is ~ 0.16 . Due to the uncertainty in the amount of the CGM, we also calculate some key results with a smaller gas fraction, $f_{\text{gas}} = 0.05$. We assume that the gas is uniformly distributed in the galactic halo with a temperature given by the virial temperature of the halo. We also show the effect of different density profiles of the CGM on its cross power spectrum.

The cosmological parameters that we have used are driven by the joint analysis of CMB anisotropies along with observations from the Baryon Acoustic Oscillations surveys. The resulting best fit cosmological parameters, especially σ_8 , are in tension with those obtained from galaxy cluster and weak lensing studies. In particular, one can have a mismatch in the galaxy cluster counts by a factor of two due to the difference in the adopted value of σ_8 . Although, much efforts have been made to calibrate cluster masses (Planck Collaboration et al., 2015b), crucial for doing cosmology with clusters, the simplest explanation for the mismatch can be a remaining systematic mass bias at the galaxy cluster scales. Similarly, unknown systematics can also lead to the amplitude of the fluctuation spectrum inferred from weak gravitational lensing to be lower than that inferred from CMB. However, this tension has been lifted to a certain extent by the ‘first’ cosmological results from the Dark Energy Survey (DES; which is one of the surveys that we consider in our analysis), where the estimated σ_8 is consistent with the *Planck* measurement (Abbott et al., 2016). There are recent indications that masses estimated from velocity dispersions (for galaxy clusters) may have more robustness than previously envisaged (Rines et al., 2015). Taking positively these developments, which bring increased consensus among different cosmological results, we adopt the *Planck* CMB cosmological parameters (Planck Collaboration et al., 2015a) as our fiducial choices. We do comment on the impact of cosmological parameters/degeneracies on our results in Section 3.6.1.

3.2.1 tSZ effect

The inverse Compton scattering of the CMB photons by high energy electrons distorts the CMB spectrum giving rise to the tSZ effect (Sunyaev & Zeldovich, 1969). The tSZ effect is represented in terms of the a dimensionless parameter, known as the Compton y -parameter, defined as $y = \int dl \frac{k_b T_e n_e \sigma_T}{m_e c^2}$, which for a flat density and temperature profile becomes $y = (k_b T_e n_e \sigma_T L) / (m_e c^2)$ where σ_T is the Thomson scattering cross section, T_e is the gas temperature ($T_e \gg T_\gamma$), n_e is the electron density of the scattering medium, and L is the distance travelled by the photons through the scattering medium. The electron density $n_e = \frac{\rho_{\text{gas}}}{\mu_e m_p}$ of the gas is determined by the condition that the total hot gas mass within the

virial radius is a fraction $f_{\text{gas}} = 0.11$ of the total halo mass. For a halo of mass M at redshift z , the virial radius is given by

$$R_{\text{vir}} = 0.784h^{-1}kpc \left(\frac{M}{10^8 h^{-1}} \right)^{1/3} \left(\frac{\Omega_M}{\Omega_M(z)} \frac{\Delta(z)}{18\pi^2} \right)^{-1/3} \left(\frac{10}{1+z} \right) \quad (3.1)$$

where $\Delta(z) = 18\pi^2 + 82d - 39d^2$ is the critical overdensity with $d = \Omega_M(z) - 1$ and $\Omega_M(z) = \Omega_M(1+z)^3/E^2(z)$, where $E(z) = \sqrt{\Omega_\Lambda + \Omega_M(1+z)^3}$.

3.3 SZ-galaxy cross-correlation

3.3.1 The angular power spectrum for tSZ

The angular Fourier transform of the Compton y -parameter (under flat sky approximation) is

$$y_l = \frac{4\pi R_s}{l_s^2} \int_0^\infty dx x^2 y_{3D}(x) \frac{\sin(lx/l_s)}{(lx/l_s)} \quad (3.2)$$

where $x = r/R_s$ is the dimensionless scaled radius, $R_s \equiv R_{\text{vir}}/c(M, z)$ is the scale radius, $l_s = D_A(z)/R_s$ and $c(M, z)$ is the concentration parameter (Duffy et al., 2008). To calculate the SZ-effect from the CGM, we truncate the integration in Equation 3.2 at $r = R_{\text{vir}}$. The 3D-radial profile $y_{3D}(x)$ is

$$y_{3D}(x) = \frac{\sigma_T}{m_e c^2} n_e(x) k_b T_e(x) \quad (3.3)$$

The angular power spectrum of the tSZ effect (Komatsu & Kitayama, 1999) is given by

$$C_l^{yy} = C_l^{yy,1h} + C_l^{yy,2h} \quad (3.4)$$

where $C_l^{yy,1h}$ is the 1-halo or Poisson term and $C_l^{yy,2h}$ is the 2-halo or clustering term. These two terms can be written as

$$C_l^{yy,1h} = g(x_v)^2 \int_0^{z_{\text{max}}} dz \frac{dV}{dz} \int_{M_{\text{min}}}^{M_{\text{max}}} dM \frac{dn(M, z)}{dM} |y_l(M, z)|^2$$

$$C_l^{yy,2h} = g(x_v)^2 \int_0^{z_{\text{max}}} dz \frac{dV}{dz} P_M(k = \frac{l}{r(z)}, z) W_l^y(z)^2$$

where, $r(z) = (1+z)D_A$ is the comoving distance, $\frac{dV}{dz}$ is the differential comoving volume per steradian, $P_M(k, z)$ is the matter power spectrum, $b(M, z)$ is the linear bias factor (Sheth & Tormen, 1999), $\frac{dn(M, z)}{dM}$ is the differential mass function, $g(x_v) = x_v \coth(x_v/2) - 4$ is the frequency dependence of the tSZ effect with $x_v = \frac{h\nu}{k_b T_{\text{CMB}}}$. We compute all the power

spectra in dimensionless units throughout the chapter. All calculations in this work are done in the Rayleigh-Jeans (RJ) limit ($g(x_\nu) \rightarrow -2$). The term $W_i^y(z)$ present in the 2-halo term is defined as

$$W_i^y(z) \equiv \int_{M_{\min}}^{M_{\max}} dM \frac{dn}{dM}(M, Z) b(M, z) y_l(M, z) \quad (3.5)$$

We use the Sheth-Tormen mass function given by

$$\frac{dn}{dM} dM = A \sqrt{\frac{2\alpha v^2}{\pi}} \frac{\rho_M}{M^2} e^{-\alpha v^2/2} \left[-\frac{d \log \sigma}{d \log M} \right] \left[1 + (\alpha v^2)^{-p} \right] dM \quad (3.6)$$

where, $A = 0.322184$, $\alpha = 0.707$, $p = 0.3$ (Sheth, Mo & Tormen, 2001) and $v = \frac{\delta_c}{D_g(z)\sigma(M)}$ where $\delta_c = 1.68$ is the critical overdensity, $D_g(z)$ is the growth factor and $\sigma(M)$ is present day smoothed (with top hat filter) variance. We take $z_{\max} = 8$ as the upper redshift integration limit and $M_{\max} = 10^{13} h^{-1} M_\odot$ as the upper mass integration limit. The lower mass integration limit is set by the condition that the gas cooling timescale is larger than the halo destruction timescale (explained in detail in Singh et al. 2015).

3.3.2 The angular power spectrum for the distribution of galaxies

For simplicity, if we assume that the mass and redshift of a galaxy can be measured accurately, the probability that a given galaxy lies in the a^{th} redshift bin $z_{\text{obs}} \in [z_{\text{obs, min}}^a, z_{\text{obs, max}}^a]$ and b^{th} mass bin $M_{\text{obs}} \in [M_{\text{obs, min}}^b, M_{\text{obs, max}}^b]$ is represented by a selection function defined as (Fang, Kadota & Takada, 2012; Oguri & Takada, 2011)

$$S_{ab}(M, Z) = \Theta(z - z_{\text{obs, min}}^a) \Theta(z_{\text{obs, max}}^a - z) \Theta(M - M_{\text{obs, min}}^b) \Theta(M_{\text{obs, max}}^b - M) \quad (3.7)$$

where Θ is the Heaviside step function. The power spectrum for the distribution of galaxies/galactic haloes in the $(ab)^{\text{th}}$ and $(a'b')^{\text{th}}$ bins is

$$C_{l, (ab, a'b')}^{hh} = \int dz \frac{dV}{dz} P_M \left(k = \frac{l}{r(z)} \right) W_{ab}^h(z) W_{a'b'}^h(z) \quad (3.8)$$

with $W_{ab}^h(z)$ defined as

$$W_{ab}^h(z) \equiv \frac{1}{\bar{n}_{ab}^2 D} \int dM \frac{dn}{dM}(M, Z) S_{ab}(M, Z) b(M, Z) \quad (3.9)$$

where \bar{n}_{ab}^{2D} is the two-dimensional angular number density of the galaxies in $(ab)^{th}$ bin and is given by

$$\bar{n}_{ab}^{2D} = \int dz \frac{dV}{dz} \int dM S_{ab}(M, Z) \frac{dn}{dM}(M, Z) \quad (3.10)$$

3.3.3 SZ-galaxy cross-correlation power spectrum

The SZ-galaxy cross power spectrum is the cross-correlation between the SZ signal and the distribution of galaxies. For the galaxies in the $(ab)^{th}$ bin, the SZ cross power spectrum is

$$C_{l,(ab)}^{yh} = C_{l,(ab)}^{yh,1h} + C_{l,(ab)}^{yh,2h} \quad (3.11)$$

where $C_{l,(ab)}^{yh,1h}$ and $C_{l,(ab)}^{yh,2h}$ are the 1-halo and 2-halo terms respectively and these terms can be written as (Fang, Kadota & Takada, 2012; Oguri & Takada, 2011)

$$C_{l,(ab)}^{yh,1h} = \frac{g(x_v)}{\bar{n}_{ab}^{2D}} \int dz \frac{dV}{dz} \int dM \frac{dn}{dM} S_{ab}(M, Z) y_l(M, Z) \quad (3.12)$$

$$C_{l,(ab)}^{yh,2h} = g(x_v) \int dz \frac{dV}{dz} P_M \left(k = \frac{l}{r(z)} \right) W_{ab}^h(z) W_l^y(z) \quad (3.13)$$

Due to the presence of $S_{ab}(M, Z)$ in Equation 3.12 and 3.13, only the galaxies lying in the a^{th} redshift bin contribute to the SZ cross power spectrum. For the 2-halo term, even the galaxies lying outside the b^{th} mass bin contribute because of the presence of $W_l^y(z)$ in Equation 3.13 (see Equation 3.5).

In Figure 3.1 we show the SZ-galaxy cross power spectrum for a few mass and redshift bin combinations. The galaxies are binned in mass (total halo mass) and redshift with $\Delta \log(M) = 0.2$ and $\Delta z = 0.1$ respectively. The mean redshift increases from left panel to right panel and the mean halo mass increases from top panel to bottom panel. Most of the contribution to the total cross power spectrum comes from the 1-halo term.

3.3.4 CGM density profile and the cross-power spectrum

For a flat pressure profile for the CGM, the SZ-galaxy cross power spectrum shows oscillations if $l > l_{\max}$, where l_{\max} depends on the mass and redshift of the galaxy. In Figure 3.2 we show l_{\max} as a function of the mean halo mass for different redshift bins. The oscillations begin when the multipole l corresponds to an angular size $\sim \frac{2}{3} \times$ virial radius of the galaxy. The reason for these oscillations is the truncation of the signal at R_{vir} .

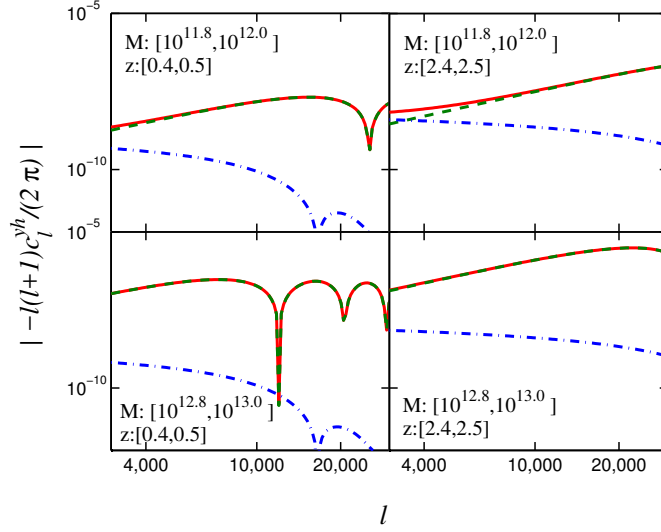


Fig. 3.1 The cross power spectra of the SZ effect in the RJ limit and the distribution of galaxies in different mass and redshift bins. Here green (dashed) lines, blue (dot-dashed) lines and red (solid) lines represent the 1-halo term, 2-halo term and the total signal respectively.

The shape of the SZ-galaxy cross power spectrum is sensitive to the pressure profile of the CGM. Since we have fixed the temperature of the CGM, the density profile of the CGM can be constrained using the cross-correlated SZ-galaxy power spectrum. In order to estimate the effect of different density profiles on the SZ cross power spectrum, we parameterise the density profile by γ_{gas} , defined by $\rho_{\text{gas}} \propto [1 + (r/R_s)^{\gamma_{\text{gas}}}]^{-1}$. In Figure 3.3 we show the total SZ cross-power spectrum for mass bins: $[10^{12.8}, 10^{13.0}] (h^{-1} M_{\odot})$ and redshift bins: $[0.4, 0.5]$ for the following three density profiles,

Profile-(a): $\gamma_{\text{gas}} = 0 \implies$ a flat density profile.

Profile-(b): $\gamma_{\text{gas}} = 1 \implies \rho_{\text{gas}} \propto [1 + (r/R_s)]^{-1}$

Profile-(c): $\gamma_{\text{gas}} = 3 \implies \rho_{\text{gas}} \propto [1 + (r/R_s)^3]^{-1}$

From profiles-(a) to (c), the density becomes steeper and more centrally concentrated. Above density profiles are similar to the β -model (with $\beta = 2/3$) with a central core followed by a gradual decrease in the density. This choice of the density profile is inspired by the observation of nearly flat distribution of the hot halo gas in the Milky Way Galaxy (Grcevich & Putman, 2009; Putman, Peek & Joung, 2012; Gatto et al., 2013) and the simulation results of Le Brun, McCarthy & Melin (2015) and Suresh et al. (2015), which predict a flatter distribution of the gas compared to the Navarro-Frenk-White (NFW) profile in galaxies due

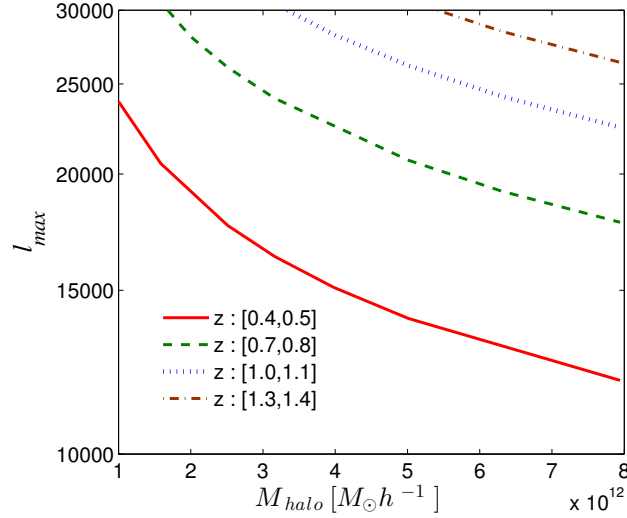


Fig. 3.2 l_{\max} is shown as a function of the mean halo mass for redshift bins z : [0.4–0.5] (red solid line), z : [0.7–0.8] (green dashed line), z : [1.0–1.1] (blue dotted line) and z : [1.3–1.4] (brown dot-dashed line).

to the presence of feedback processes. In all 3 cases the SZ signal is truncated at the virial radius. As the density profile becomes steeper from (a) to (c) the value of l_{\max} shifts from 12000 to 14000 whereas there are no oscillations in the case of profile-(c). This shift occurs since with the steepening of the density profile, the pressure at the virial radius decreases.

In Figure 3.3 at small l -values (~ 3000), the SZ cross power spectrum for the three density profiles are almost identical but there is a significant difference between the profiles near $l \sim 10^4$. This is because the steepening of the density profile increases the power at small angular scales or large l values. The value of l where the shape of the cross-power spectrum is significantly different for different density profiles depends on the mean mass and redshift of the bin in a similar way as for l_{\max} . Therefore, the shape of the SZ-galaxy cross-power spectrum at these l -values can be used to determine the slope of the density profile of the CGM. However, the use of this method is limited by the resolution of the CMB survey. Presently the SPT survey has the best resolution and it goes up to $l \approx 10^4$. High mass and low redshift galaxies are better choices for this purpose as the SZ power spectrum for different profiles is distinguishable at $l < 10^4$ for these galaxies.

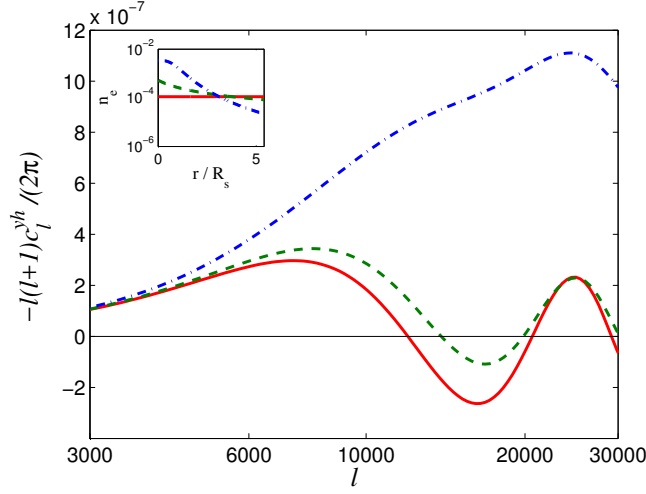


Fig. 3.3 The cross power spectra of the SZ effect (in RJ limit) and the distribution of the galaxies for $M_h : [10^{12.8}, 10^{13.0}](h^{-1}M_\odot)$ and $z : [0.4, 0.5]$ for the density profile-(a) (red solid line), profile-(b) (green dashed line) and profile-(c) (blue dot-dashed line) i.e. $\gamma_{\text{gas}} = 0, 1 \& 3$ respectively. In the inset, we show the corresponding density profiles.

3.3.5 Detectability of the SZ-galaxy cross-correlation signal

Cumulative signal to noise ratio

Given a survey one can estimate the detectability of the SZ-galaxy cross-correlation signal for galaxies binned according to their masses and redshift using the cumulative signal to noise ratio (SNR) defined as

$$\left(\frac{S}{N}\right)^2 = \Sigma_{ll'} C_{l,(ab)}^{yh} (M_{ll',(ab)}^{yh})^{-1} C_{l',(ab)}^{yh} \delta_{ll'} \quad (3.14)$$

where $M_{ll',(ab)}^{yh}$ is the covariance matrix which represents the uncertainty in the measurement of $C_{l,(ab)}^{yh}$. The covariance matrix is given by

$$M_{ll',(ab,a'b')}^{yh} = \frac{\delta_{ll'}}{f_{\text{sky}}(2l+1)\Delta l} \times \left[\hat{C}_l^{yy} \hat{C}_{l,(ab,a'b')}^{hh} + \hat{C}_{l,(ab)}^{yh} \hat{C}_{l,(a'b')}^{yh} \right] \quad (3.15)$$

where f_{sky} is the fractional sky coverage for a survey, Δl is the l -bin size used to calculate the power spectrum and \hat{C}_l^i 's represent the power spectrum including the noise contribution (i.e. $C_l^i + N_l^i$) where i stands for yy , hh and yh . For simplicity, we neglect the non-Gaussian contribution for the l -range considered: this is particularly true for the massive galaxies. Note that the dominant contribution to the noise in the SZ-galaxy as well as X-ray-galaxy

Table 3.1 Specifications of surveys

Survey	Ω_s (deg ²)	f_{sky}	ν (GHz)	θ_{FWHM} (arcmin)	σ_T (μK)
SPT	2500	6%	95	1.6	26.3
			150	1.1	16.4
			220	1.0	85

Survey	Ω_s (deg ²)	f_{sky}	z range
DES	5000	12%	0.1-1.4
LSST	20000	48%	0.1-1.4

Survey	Ω_s (deg ²)	f_{sky}	θ_{FWHM} (arcsec)	Exposure time (ks)
eROSITA	All sky	100%	20	2

cross-power spectrum comes from the instrumental noise. Thus, the inclusion of clusters has negligible effect on the error calculations and hence the SNR. Therefore, we neglect this contribution in our calculation.

The instrumental noise simply adds to the SZ power spectrum and for a given CMB survey, it is given by

$$N_l^{yy,(\text{CMB})} = \frac{1}{\sum_k w_k s_k^2 B_{kl}^2} \quad (3.16)$$

where the summation in Equation 3.16 is over the different frequency channels, $w = (\sigma_T \theta_{\text{FWHM}} / T_{\text{CMB}})^{-2}$ where σ_T is the rms instrumental noise per pixel, θ_{FWHM} is the full width half maximum of the beam, $B_l^2 = \exp[-l(l+1)\theta_{\text{FWHM}}^2/(8\ln 2)]$ is the fourier transform of beam profile and $s = -g(x_\nu)/2$ is to rescale the result in RJ limit. The shot noise in the galaxy distribution power spectrum is

$$N_{(ab,a'b')}^{hh,(g)} = \frac{1}{n_{ab}^{2D}} \delta_{aa'} \delta_{bb'} \quad (3.17)$$

For the cross-power spectrum $N_l^{yh} = 0$ i.e. $\hat{C}_l^{yh} = C_l^{yh}$ as the distribution of galaxies is not correlated with the instrumental noise in the CMB surveys.

CMB survey

To detect the SZ-galaxy cross-correlation signal, we need a galaxy survey and a CMB survey with overlapping sky coverages. Since the SZ signal from the CGM becomes non-negligible compared to other contribution to CMB distortion at large l -values (at $l \gtrsim 3000$), we

consider the SPT survey for this work. Presently, the optical survey which overlaps with the SPT survey, is the DES. The specifications of these surveys are given in Table 3.1.

Note that, the dominant contribution to the covariance in Equation 3.15 comes from $N_l^{yy,(\text{CMB})}/n_{ab}^{2D}$ for $l > 3000$. The contribution from other terms ($C_l^{yy}C_l^{hh}$, $C_l^{hh}N_l^{yy,(\text{CMB})}$, C_l^{yy}/n_{ab}^{2D} and $C_l^{yh}C_l^{yh}$) is negligible compared to this term. For example, for the haloes in the mass bin $M_h : [10^{12.8}, 10^{13.0}](h^{-1}M_\odot)$ and redshift bin $z : [0.4, 0.5]$, the instrumental noise is nearly three to four orders of magnitude larger than C_l^{yh} .

In Figure 3.4 we show the contours of cumulative SNR of the SZ-galaxy cross power spectrum of the CGM for the flat density profile. The galaxies are binned in mass and redshift with $\Delta \log(M) = 0.2$ and $\Delta z = 0.1$ respectively. Here we take $l_{min} = 3000$. Note that the DES survey goes only upto $z \sim 1.4$ whereas in Figure 3.4 we have shown the results upto $z \sim 3$ to show the decreasing contribution from high redshift haloes. The SZ signal increases with increasing halo mass for a given redshift as the amount of gas causing the SZ-effect increases with increasing halo mass. This results in higher SNR for higher mass galaxies compared to the low mass haloes in the same redshift bin. For a given halo mass, the SNR first increases with increasing redshift, reaches a maximum value and then decreases. As a combined effect there is an optimum spot with $\text{SNR} \sim 9$ at the high mass end of galaxies, at redshift around $z \sim 1.5-2$. Even for low mass galaxies ($M_h \sim 2-4 \times 10^{12}h^{-1}M_\odot$) the SNR is ~ 3 in the redshift range covered by the DES survey. This makes the SPT-DES survey a useful tool to study the CGM in the low mass galaxies which is otherwise difficult to detect at higher redshifts.

In the calculation of the SNR in this section as well as the constraints on the model parameters from the SZ-galaxy cross-power spectrum in Section 3.6.1 and 3.7, we neglect the contamination from other astrophysical sources (kSZ, CIB, point sources etc.). However, the tSZ signal has a distinct frequency dependence and the relative contribution from other sources can be minimized using multi-frequency data from surveys like SPT.

3.4 X-ray-galaxy cross-correlation

The hot CGM causing the SZ-effect also emits in the soft X-rays. This X-ray emission from the galaxies can be cross-correlated with the galaxy distribution to increase its detectability. The X-ray surface brightness due to the presence of the hot gas in a direction θ (eg. Cheng, Wu & Cooray 2004) is given by

$$S(\theta) \approx \frac{1}{4\pi(1+z)^4} \int n_e^2 \Lambda(T, Z) d\chi \quad (3.18)$$

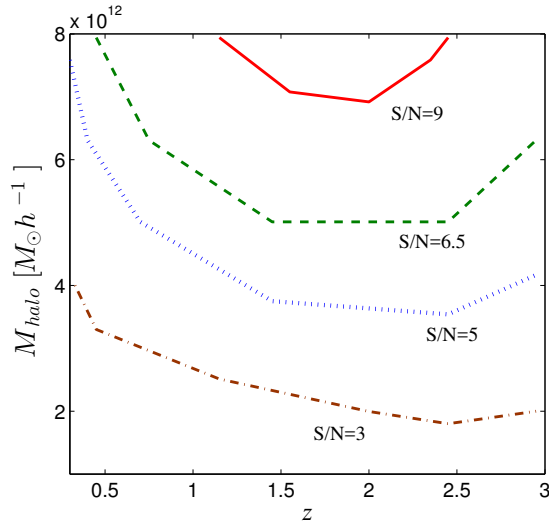


Fig. 3.4 Contours of the cumulative signal-to-noise (SNR) for the measurement of the cross-power spectrum of the SZ effect with the distribution of galaxies for the combined SPT-DES like surveys. The red (solid), green (dashed), blue (dotted) and brown (dot-dashed) lines represent the SNR 9, 6.5, 5 and 3 respectively. The upper redshift limit plotted here is more than the highest redshift probed by DES.

where $\Lambda(T, Z)$ is the cooling function which depends on the metallicity and temperature of the gas. We assume that the halo gas has a metallicity $\sim 0.1 Z_{\odot}$ and use the cooling function from Sutherland & Dopita (1993). For the metallicity and mass range of interest, we calculate the emission from the CGM in the soft X-ray band (0.5-2.0 keV) assuming that the fraction of total energy in soft X-ray band is $\sim (\exp^{-\frac{E_1}{k_b T}} - \exp^{-\frac{E_2}{k_b T}})$, where E_1 is the lower and E_2 is the higher energy limit of the soft X-ray band. The mass and redshift range considered here corresponds to the temperature range $\sim 10^6$ - 10^7 K. Therefore, these galaxies lie near the lower energy limit of the soft X-ray band used for this study.

The fluctuations in the X-ray background in the direction θ are

$$s(\theta) = \frac{S(\theta)}{\langle S_{\text{SXR}} \rangle} - 1 \quad (3.19)$$

where $\langle S_{\text{SXR}} \rangle$ is the mean surface brightness of the soft X-ray background (SXR) and it includes all possible sources of soft X-ray background (see Merloni et al. 2012).

3.4.1 The X-ray angular power spectrum

In analogy with the SZ-effect, the angular Fourier transform of fluctuations in the SXRБ (for $l > 0$) is given by

$$s_l = \frac{4\pi R_s}{l_s^2} \int_0^\infty dx x^2 s_{3D}(x) \frac{\sin(lx/l_s)}{(lx/l_s)} \quad (3.20)$$

where the 3D-radial profile $s_{3D}(x)$ is

$$s_{3D}(x) = \frac{1}{4\pi(1+z)^4} \frac{n_e^2(x)\Lambda(T, Z)}{\langle S_{\text{SXRБ}} \rangle} \quad (3.21)$$

The X-ray power spectrum can be obtained by replacing $g(x_\nu)y_l$ by s_l in Equation 3.5.

$$C_l^{\text{xx},1h} = \int_0^{z_{\text{max}}} dz \frac{dV}{dz} \int_{M_{\text{min}}}^{M_{\text{max}}} dM \frac{dn(M, z)}{dM} |s_l(M, z)|^2 \quad (3.22)$$

$$C_l^{\text{xx},2h} = \int_0^{z_{\text{max}}} dz \frac{dV}{dz} P_M(k = \frac{l}{r(z)}, z) W_l^x(z)^2 \quad (3.23)$$

with $W_l^x(z)$ defined as

$$W_l^x(z) \equiv \int_{M_{\text{min}}}^{M_{\text{max}}} dM \frac{dn}{dM}(M, Z) b(M, z) s_l(M, z) \quad (3.24)$$

Similarly, the X-ray-galaxy cross-power spectrum is given by

$$C_{l,(ab)}^{\text{xh},1h} = \frac{1}{\bar{n}_{ab}^{2D}} \int dz \frac{dV}{dz} \int dM \frac{dn}{dM} S_{ab}(M, Z) s_l(M, Z)$$

$$C_{l,(ab)}^{\text{xh},2h} = \int dz \frac{dV}{dz} P_M(k = \frac{l}{r(z)}) W_{ab}^h(z) W_l^x(z) \quad (3.25)$$

To calculate $\langle S_{\text{SXRБ}} \rangle$ we use the soft X-ray background counts expected to be observed by the eROSITA mission (Merloni et al., 2012) assuming a conversion factor 1 count/sec $\sim 10^{-11}$ erg sec $^{-1}$ cm $^{-2}$, which is approximately the conversion factor for the ROSAT all sky survey. Note that using a constant conversion factor underestimates the power at low redshifts ($z < 1$ for massive galaxies) and overestimates the power at high redshifts ($z > 1$). Therefore, this simplified approach gives only an order of magnitude estimate of the X-ray power spectrum. However, this does not affect the estimate of the uncertainty on the model parameters using X-ray-galaxy cross-power spectrum as the main contribution to the constraints comes from the massive galaxies near $z \sim 1$. In addition, these constraints saturate fast once

the information from two or more appropriate mass-redshift bins is combined together as shown in Section 3.6.1.

In Figure 3.5 we show the X-ray-galaxy cross power spectrum for a few mass and redshift bins. For the flat density and temperature profiles, the shape of the X-ray-galaxy cross-correlation power spectrum is analogous to the shape of the SZ-galaxy cross power spectrum and has the same value of l_{\max} . The contribution of the 2-halo term is negligible compared to the 1-halo term beyond $l = 10^4$ for all mass and redshift bin combinations considered here.

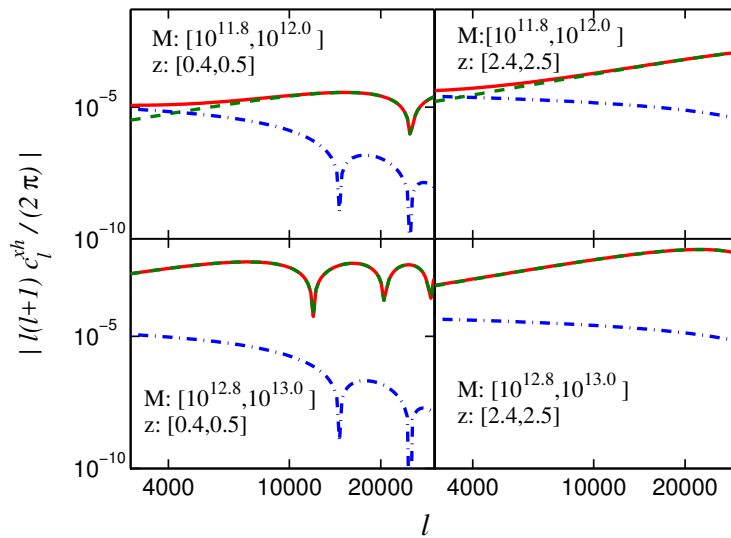


Fig. 3.5 The cross power spectra of the X-ray emission from the CGM and the distribution of galaxies in different mass and redshift bins. Here green (dashed) lines, blue (dot-dashed) lines and red (solid) lines represent the 1-halo term, 2-halo term and the total signal respectively.

In Figure 3.6 we show the X-ray-galaxy cross power spectrum for $M_h : [10^{12.8}, 10^{13.0}] (h^{-1} M_\odot)$ and $z : [0.4, 0.5]$ for the density profiles described in Section 3.3.4. Note that for all these profiles we have assumed the CGM to be at the virial temperature and we truncate the signal at the virial radius. The X-ray-galaxy cross-correlation signal increases rapidly compared to the SZ-galaxy cross-correlation signal with the steepening of the density profile. This is due to the fact that the X-ray emission is proportional to n_e^2 and is more sensitive to the gas density profile compared to the SZ-effect which is proportional to n_e . The difference between the profiles is now significant even at smaller l -values (~ 3000).

3.4.2 Detectability of the X-ray-galaxy cross-correlation signal

As mentioned earlier in Section 3.3.5, the cumulative signal-to-noise ratio provides an efficient way of estimating the detectability of a signal for a given survey. The cumulative SNR of the X-ray-galaxy cross power spectrum in ab^{th} bin is

$$\left(\frac{S}{N}\right)^2 = \Sigma_{ll'} C_{l,(ab)}^x (M_{ll',(ab)}^{xh})^{-1} C_{l',(ab)}^{xh} \delta_{ll'} \quad (3.26)$$

where the covariance matrix $M_{ll',(ab)}^{xh}$ for the X-ray-galaxy cross-correlation is given by

$$M_{ll',(ab,a'b')}^{xh} = \frac{\delta_{ll'}}{f_{\text{sky}}(2l+1)\Delta l} \times \left[\hat{C}_l^{xx} \hat{C}_{l,(ab,a'b')}^{hh} + \hat{C}_{l,(ab)}^{xh} \hat{C}_{l,(a'b')}^{xh} \right] \quad (3.27)$$

with $\hat{C}_l = C_l^i + N_l^i$. Assuming that the noise in X-rays is dominated by the shot noise, the noise in the X-ray power spectrum is

$$N_l^{xx} = \frac{1}{N_{\text{bg}}} \exp\left(\frac{l(l+1)\theta_{\text{FWHM}}^2}{8\ln 2}\right) \quad (3.28)$$

where N_{bg} is the total number of the soft X-ray photons collected/steradian by the X-ray telescope and θ_{FWHM} is the full width half maximum of the beam.

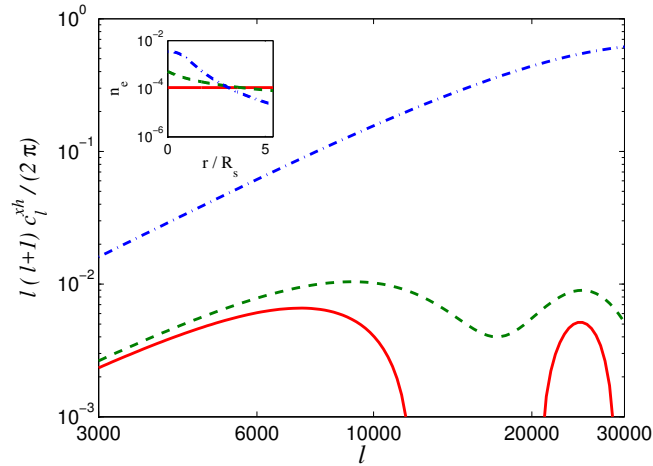


Fig. 3.6 The X-ray-galaxy cross power spectra for $M_h : [10^{12.8}, 10^{13.0}](h^{-1}M_\odot)$ and $z : [0.4, 0.5]$ for the density profile-(a) (red solid line), profile-(b) (green dashed line) and profile-(c) (blue dot-dashed line). In the inset we show the corresponding density profiles.

In practice some of the X-ray background is produced by the X-ray emission of AGNs, X-ray binaries, SNe remnants amongst which AGNs are dominant. AGNs are clustered with

galaxies and would thus contribute to the X-ray-galaxy correlation. This could however be mitigated by first removing the fraction of X-ray AGNs which are above the detection threshold of the X-ray survey. In addition, AGNs have a harder X-ray spectrum than the diffuse circumgalactic X-ray gas. The photon energy dependence of the cross-correlation signal can thus also be used to separate the contribution from AGNs. In addition, the signal from AGNs would be produced by a 1-source term and a clustering term with an angular dependence determined by the point spread function (PSF) of the X-ray instrument and the correlation function of the AGNs. This specific angular dependence can be used to disentangle the contribution from the AGNs and from the circumgalactic gas. While a detailed analysis which incorporates these mitigating techniques is beyond the scope of this thesis, we make the optimistic assumption that the X-ray noise is not correlated with the distribution of galaxies, i.e. $N_i^{xh} = 0$ in Equation 3.27.

3.4.3 X-ray survey

Since we are interested in the X-ray signal from the galaxies, we need an X-ray survey with a small beam size (high resolution) and large sky coverage. We consider the eROSITA survey for this purpose. The eROSITA is a future mission expected to be launched in 2016 (see Merloni et al. 2012 for the details of this mission). The specifications of this mission are given in Table 3.1. The total background expected in the soft band of the eROSITA is $\sim 2 \times 10^{-3}$ counts $\text{sec}^{-1} \text{arcmin}^{-2}$ (Merloni et al., 2012). To calculate the X-ray-galaxy cross-power spectrum, we consider the combination of the eROSITA-DES and eROSITA-LSST (Large Synoptic Survey Telescope) surveys.

In Figure 3.7 we show the contours of the cumulative SNR for the X-ray-galaxy cross power spectrum for the eROSITA-DES combination. Similar to the SZ-galaxy cross power spectrum, the galaxies are binned in mass and redshift with $\Delta \log(M) = 0.2$ and $\Delta z = 0.1$ respectively. Again the high mass galaxies have larger SNR due to their larger gas reservoir compared to the low mass galaxies and the SNR increases with increasing redshift, becomes maximum and then decreases with further increase in redshift. The difference between the X-ray-galaxy and SZ-galaxy cross power spectra is that the X-ray cross-power spectrum peaks at relatively smaller redshift compared to the SZ cross-power spectrum due to the fact that the observed X-ray surface brightness decreases rapidly with increasing redshift. Also the contribution from the low mass galaxies at high redshifts is more than that of the SZ-galaxy cross power spectrum. This is essentially due to the much better resolution of the eROSITA ($\sim 20''$) compared to the resolution of the SPT ($\sim 1'$). The SNR peaks for the high mass and intermediate redshift galaxies ($z \sim 1$). For the most massive galaxies ($M_h = [10^{12.8}, 10^{13.0}] h^{-1} M_\odot$) at redshift $z \sim 1$, the SNR is ~ 7 . For the low mass galaxies

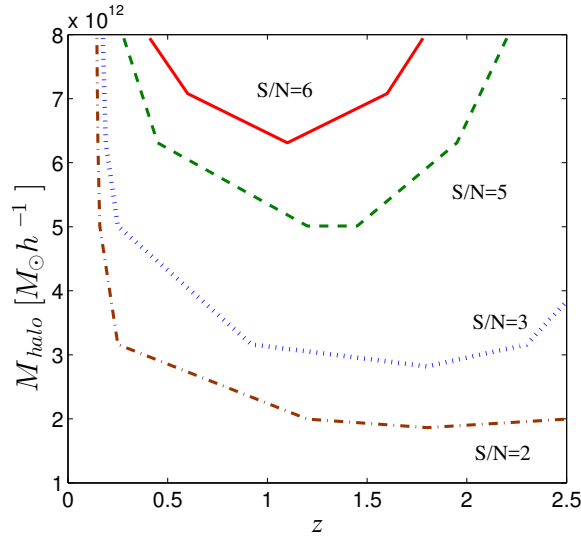


Fig. 3.7 Contours of the cumulative signal to noise (SNR) for the measurement of the cross-power spectrum of the X-ray emission from the CGM with the distribution of galaxies for the combined eROSITA-DES-like survey. The red (solid), green (dashed), blue (dotted) and brown (dot-dashed) lines represent the SNR 6, 5, 3 and 2 respectively. Note that, the upper redshift limit plotted here is more than the highest redshift probed by DES.

($\lesssim 10^{12} h^{-1} M_{\odot}$), the SNR is low (< 2) at all redshifts. Massive galaxies have significant SNR (~ 6) even at redshifts < 0.5 , hence the X-ray-galaxy cross-power spectrum can be used to study the the CGM of these systems.

The sky coverage of the LSST is 4 times the sky coverage of the DES. Since the cumulative SNR $\propto \sqrt{f_{\text{sky}}}$, SNR for the eROSITA-LSST combination will be twice the SNR of the eROSITA-DES combination. Therefore, for the assumed CGM properties, the eROSITA-LSST survey will be able to detect the X-ray-galaxy cross-correlational signal from the galaxies with a peak SNR ~ 14 . Note that the estimates of the SNR for both the SZ-galaxy and X-ray-galaxy power spectra depend on the size of the mass and redshift bins. Therefore, increasing or decreasing the size of mass and/or redshift bin also changes the detectability of these signals accordingly.

3.5 X-ray-SZ cross-correlation

The SZ effect and X-ray emission have different dependences on the gas density and temperature. The SZ effect is proportional to $n_e T_e$ whereas the X-ray emission scales approximately as $n_e^2 \sqrt{T_e}$. Combining the two can improve the constraints on the gas physics parameters. The X-ray-SZ cross power spectrum is given by

$$C_l^{xy} = C_l^{xy,1h} + C_l^{xy,2h} \quad (3.29)$$

where

$$\begin{aligned} C_l^{xy,1h} &= g(x_V) \int_0^{z_{\max}} dz \frac{dV}{dz} \int_{M_{\min}}^{M_{\max}} dM \frac{dn(M, z)}{dM} [s_l(M, z) \times y_l(M, z)] \\ C_l^{xy,2h} &= g(x_V) \int_0^{z_{\max}} dz \frac{dV}{dz} P_M(k = \frac{l}{r(z)}, z) [W_l^x(z) \times W_l^y(z)] \end{aligned} \quad (3.30)$$

In Figure 3.8 we show the X-ray-SZ cross power spectrum for the flat density profile and the mass and redshift range specified in Section 3.3.1 in dimensionless as well as $10^{-6} \text{ counts sec}^{-1} \text{ arcmin}^{-2}$ units. The cross-power spectrum peaks at $l \approx 15000$ for galactic haloes whereas for galaxy clusters it peaks at $l \approx 3000$ (see Figure 1 of Hurier, Aghanim & Douspis 2014). This difference is mainly because the galaxies are smaller objects than the clusters and therefore, the X-ray-SZ cross power spectrum for galaxies peaks at smaller angular scales or larger l -values. Recently, Hurier et al. (2015) detected the total X-ray-SZ cross-power spectrum at 28σ level with ROSAT and *Planck* all sky surveys. For the l -range of interest for the CGM, we show the SPT-eROSITA combination. However, due to the weak signal compared to the noise for SPT-eROSITA surveys ($\text{SNR} \sim 0.65$), it is not possible to detect the X-ray-SZ cross-correlation signal from the CGM.

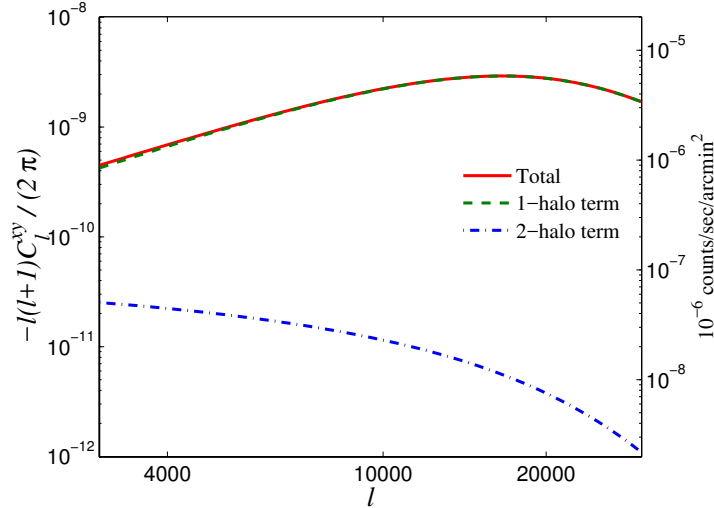


Fig. 3.8 The cross power spectra of the SZ effect in RJ limit and soft X-ray emission from CGM. Here green (dashed) lines, blue (dot-dashed) lines and red (solid) lines represent the 1-halo term, 2-halo term and the total signal respectively.

3.6 Forecasting of CGM constraints

We now use the Fisher matrix formalism to forecast the expected constraints for different survey combinations. Since the cosmological parameters are well constrained by *Planck*, our main focus is to constrain the astrophysical parameters related to the gas physics. The parameters considered for this work are

$$\{[\sigma_8, \Omega_M, n_s], [f_{\text{gas}}, f_{\text{Temp}}, \alpha_{\text{gas}}]\} , \quad (3.31)$$

where the parameters in the first bracket are cosmological parameters and in the second bracket are astrophysical parameters which depend on baryonic physics. Note that we have assumed the flat- Λ CDM cosmology. The fiducial values of these parameters are given in Table 3.2. Here f_{gas} is the redshift independent gas fraction, $f_{\text{Temp}} = \frac{T}{T_{\text{vir}}}$, i.e., the ratio of the temperature of the gas to the virial temperature of the gas in the halo and α_{gas} represents any possible evolution of the gas defined through $f_{\text{gas}}(z) = f_{\text{gas}}[E(z)]^{\alpha_{\text{gas}}}$. Our fiducial model assumes no redshift evolution of the gas fraction i.e. $\alpha_{\text{gas}} = 0$.

Table 3.2 Fiducial values and priors on the parameters

Parameter	Fiducial value	Prior-1	Prior-2
σ_8	0.831	0.013	0.013
Ω_M	0.3156	0.0091	0.0091
n_s	0.9645	0.0049	0.0049
f_{gas}	0.11	-	-
f_{Temp}	1.0	-	0.25
α_{gas}	0.0	-	-

Given a fiducial model, the Fisher matrix can be written as

$$F_{ij} = \Sigma_{ll'} \frac{\partial C_\ell}{\partial p_i} (M_{\ell\ell'})^{-1} \frac{\partial C_{\ell'}}{\partial p_j} \delta_{ll'} \quad (3.32)$$

where $M_{ll'}$ is the covariance matrix given by Equation 3.15. To calculate the uncertainty on the parameters we have considered following two prior cases:

Prior-1 : Priors on cosmological parameters only.

Prior-2 : Priors on cosmological parameters + 25% prior on f_{Temp} .

We have included only those galaxies for which the gas cooling time is more than the halo destruction time ensuring that the CGM temperature is close to the virial temperature of the halo. Therefore, we assume a small uncertainty in f_{Temp} in Prior-2 .

3.6.1 Results

In Table 3.3 and 3.4 we show the forecasted uncertainty on the parameters for the SPT-DES and eROSITA-DES surveys respectively. Here we have combined the Fisher from three different combinations of the mass and redshift bins M1Z1, M2Z1 and M2Z2 where $M1=[10^{11.8}, 10^{12.0}]h^{-1}M_{\odot}$, $M2=[10^{12.8}, 10^{13.0}]h^{-1}M_{\odot}$, $Z1=[0.4, 0.5]$ and $Z2=[1.0, 1.1]$. We show the constraints on the astrophysical parameters only as the cosmological parameters are already well constrained by *Planck*. There is a strong degeneracy between the gas physics parameters if we consider only one mass and redshift bin. However, when the information from two or more bins are added together, we can break this degeneracy and obtain strong constraints on these parameters. In Table 3.3 we show the constraints on the parameters from the SZ-galaxy cross-correlation signal for the SPT-DES survey. Combining the Fisher matrix from M1Z1, M2Z1 and M2Z2 can constrain f_{gas} to $\sim 44\%$ and f_{Temp} to $\sim 37\%$ around their fiducial values, even without any prior knowledge on astrophysical parameters. For Prior-1, the constraint on α_{gas} is $\Delta\alpha_{\text{gas}} \sim 0.5$. Including additional 25% prior on gas temperature does not improve the constraint on α_{gas} whereas the constraint on f_{gas} (f_{Temp}) improves considerably to 34% (21%).

Table 3.3 Error on parameters for different scenarios for SPT-DES combination

Parameter	P1	P2	P1 (fixed α_{gas})	P2 (fixed α_{gas})
f_{gas}	0.049	0.037	0.042	0.025
f_{Temp}	0.369	0.207	0.369	0.207
α_{gas}	0.519	0.519	-	-

Table 3.4 Error on parameters for different scenarios for eROSITA-DES combination

Parameter	P1	P2	P1 (fixed α_{gas})	P2 (fixed α_{gas})
f_{gas}	0.20	0.025	0.036	0.015
f_{Temp}	2.65	0.25	0.649	0.233
α_{gas}	1.219	0.318	-	-

In the absence of any redshift evolution of the gas fraction, the constraint on f_{Temp} does not improve whereas the constraint on f_{gas} improves to $\sim 38\%$ for Prior-1 and to $\sim 23\%$ for Prior-2.

We use only above three mass-redshift bins to forecast the constraints on gas physics parameters as the addition of more bins does not improve these constraints much. For example, for Prior-1, the addition of mass-redshift bin M2Z3, where $Z3=[0.8, 0.9]$, improves the constraint on f_{gas} and α_{gas} from 0.049 and 0.5 to 0.047 and 0.46 respectively whereas the change in the constraint on f_{Temp} is $< 1\%$. Also the change in these constraints in other prior

cases is negligible. Further addition of mass-redshift bins in the Fisher matrix analysis does not improve these constraints. Therefore, we use only the bins M1Z1, M2Z1 and M2Z2 for the purpose of our work.

In Table 3.4 we show the constraints on the parameters from the X-ray-galaxy cross-correlation signal for the eROSITA-DES survey. Now for Prior-1 and in the presence of unknown redshift evolution of the gas fraction, astrophysical parameters are poorly constrained by this survey. This is mainly due to the large noise contamination from the X-ray background. The addition of a 25% prior on f_{Temp} significantly improves the constraints on the parameters. The uncertainty on f_{gas} reduces to 23% and α_{gas} can be constrained to $\Delta\alpha_{\text{gas}} \sim 0.3$.

In the absence of any redshift evolution of the gas fraction, f_{gas} (f_{Temp}) can be constrained to $\sim 33\%$ (65%) for Prior-1 and the constraint becomes $\sim 14\%$ (23%) for Prior-2.

In Figure 3.9, we show the constraints from the SPT-DES (SZ-galaxy cross power spectrum) and eROSITA-DES (X-ray-galaxy cross power spectrum) surveys in the upper and lower panels respectively. All the plots are for Prior-2 and in the right panels, we have fixed α_{gas} . In the upper left panel we show the 68% confidence limit (CL) ellipse for f_{gas} and α_{gas} for the SZ-galaxy cross power spectrum. The individual ellipses for M1Z1, M2Z1 and M2Z2 are large and there is a large uncertainty on these parameters. But combining them together results in $\Delta f_{\text{gas}} \approx 0.037$ i.e. we can constrain f_{gas} to $\sim 34\%$. This is because the degeneracy of f_{gas} with α_{gas} is broken when we add information from the galaxies in similar mass bins but in different redshift bins. The X-ray-galaxy cross power spectrum also has similar contours for f_{gas} v/s α_{gas} (lower left panel of Figure 3.9). In this case, the Fisher matrix analysis gives a constraint $\Delta f_{\text{gas}} \approx 0.025$ on gas fraction, i.e. 23% of its fiducial value. In both the cases, M1Z1 bin has relatively large uncertainty and the final uncertainty ellipse is essentially determined by the other two bins. The amount of gas present in the M1Z1 bin is roughly an order of magnitude smaller than that of the other bins which results in a smaller signal and large uncertainty on the parameters.

In the upper right panel of Figure 3.9 we show the constraints on the SPT-DES survey for Prior-2 case and the redshift-independent gas fraction. Here adding the information from different bins does not improve the constraints on the parameters as we already have a strong prior on f_{Temp} ($\sim 25\%$ of its fiducial value). However, even with a strong prior on the CGM temperature, there is a large uncertainty in the gas fraction for M1Z1 bin which is again due the small signal in this bin. In the lower right panel on Figure 3.9 we show the 68% CL ellipses for $f_{\text{gas}} - f_{\text{Temp}}$ from eROSITA-DES survey. This survey can constrain the gas fraction to $\Delta f_{\text{gas}} \approx 0.015$ in case of a redshift-independent f_{gas} .

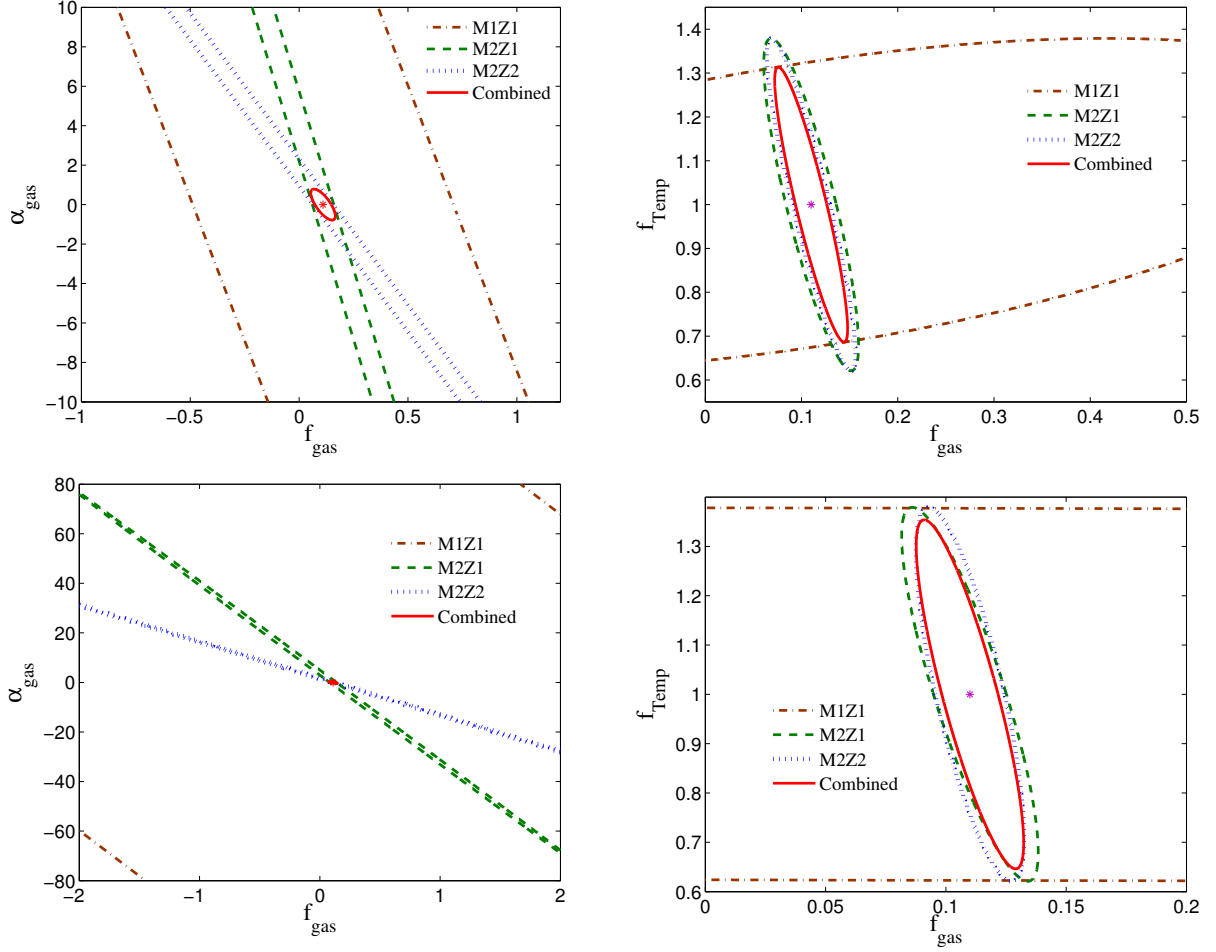


Fig. 3.9 The 68% CL for the gas physics parameters f_{gas} , f_{Temp} and α_{gas} from the SPT-DES (SZ-galaxy cross power spectrum) and eROSITA-DES (X-ray-galaxy cross power spectrum) surveys in the upper and lower panels respectively. All the plots are for Prior-2 case and in the right panels, we have fixed α_{gas} . The brown (dot-dashed), green (dashed), blue (dotted) and red (solid) lines represent the ellipses for the mass and redshift bins M1Z1, M2Z1, M2Z2 and the combined ellipse respectively.

Note that, in the calculation of the constraints on gas physics parameters, we have used strong priors on the cosmological parameters (from Planck Collaboration et al. 2015a). However, if we remove the prior on the cosmological parameters, it increases the uncertainty in the determination of the gas physics parameters. For example, if we remove the prior on σ_8 , the uncertainty on the gas physics parameters becomes larger than 100% for SZ-galaxy as well as X-ray-galaxy cross-correlation in Prior-1 case. But the inclusion temperature prior (Prior-2 case) improves the constraint on f_{gas} ($\Delta f_{\text{gas}} = 0.041$ (0.026) for SZ-galaxy (X-ray-galaxy) cross-correlation) and α_{gas} ($\Delta \alpha_{\text{gas}} = 0.52$ (0.38) for SZ-galaxy (X-ray-galaxy) cross-correlation) significantly even in the absence of any prior on σ_8 . These constraints are similar to the constraints on these parameters in the presence of *Planck* prior on σ_8 . Therefore, the prior knowledge of one of the gas physics parameter helps in breaking the degeneracy between the cosmological and gas physics parameters.

3.7 Probing the energetics of the CGM

Currently, there is a large uncertainty in the knowledge of the distribution of the CGM. Simulations suggest that the extent and distribution of the CGM also depends on the feedback processes taking place in the central part of the galaxy (Le Brun, McCarthy & Melin, 2015; Suresh et al., 2015). Without any feedback, the temperature at outer radii falls rapidly, whereas the winds and AGN feedback tend to make the profile flatter. The effect of the feedback on the density profile is however weaker than on the temperature profiles. In other words, the pressure profile is likely to be flatter at the outer radii in the presence of the feedback processes than in the cases without any feedback.

In this section, we investigate whether the SZ/X-ray-galaxy cross power spectrum can distinguish between different density profiles of the CGM and hence the processes giving rise to these profiles. In order to constrain the density profile of the CGM, assuming the gas to be at the virial temperature, we now include γ_{gas} in the Fisher matrix analysis, where γ_{gas} is defined by

$$\rho_{\text{gas}} = \rho_0 [1 + (r/R_s)^{\gamma_{\text{gas}}}]^{-1} \quad (3.33)$$

where ρ_0 is the normalization such that the mass within the virial radius of the galaxy remains the same and the fiducial value of γ_{gas} is 0 for the flat density profile. For the SPT-DES survey, the uncertainty on the γ_{gas} is large and it can at best be constrained to $\gamma_{\text{gas}} < 3.16$ in the absence of any redshift evolution of f_{gas} and Prior-2 case. Even when we include the redshift evolution of gas fraction and remove the prior on gas temperature, the uncertainty on γ_{gas} degrades only slightly to $\gamma_{\text{gas}} < 3.35$. This shows that the SZ-galaxy cross power spectrum is less sensitive to the density profile of the CGM as compared to other astrophysi-

cal parameters within the resolution of the SPT ($l \sim 10^4$). Varying the density profile affects the SZ-galaxy cross power spectrum only at large l -values and hence this situation can only be improved by a higher resolution CMB survey in the future.

On the other hand, the X-ray emission which is proportional to the square of the density of the CGM, is much more sensitive to its density profile even at small l -values. Also the resolution of the eROSITA ($l \sim 30000$) is much better than the resolution of the SPT. As a result, γ_{gas} can be constrained to $\gamma_{\text{gas}} < 0.6$ by the X-ray-galaxy cross power spectrum. This constraint remains almost invariant even if we fix α_{gas} in the Prior-2 case.

In the case of a steeper density profile i.e. a larger value of γ_{gas} , both the SZ-galaxy and X-ray-galaxy cross power spectrum increase, specially at large l -values (see Figure 3.3 and 3.6). This results in an increased signal-to-noise ratio, as well as an improvement in the constraints on the parameters. For example, if we take $\gamma_{\text{gas}} = 2$, the constraint on γ_{gas} improves to $\Delta\gamma_{\text{gas}} < 1$ from the SZ-galaxy cross power spectrum whereas the slope of the density profile can be constrained with an accuracy better than 5% (i.e. $\Delta\gamma_{\text{gas}} < 0.1$) from the X-ray-galaxy cross power spectrum.

In Figure 3.10, we show the 68% CL ellipses for $f_{\text{gas}} - \gamma_{\text{gas}}$ from the SPT-DES and the eROSITA-DES surveys. Again, due to the more sensitive dependence of the X-ray emission on the CGM density profile as compared to the SZ-effect, the uncertainty ellipses of the X-ray-galaxy cross-correlation are smaller and hence can constrain γ_{gas} better than the SZ-galaxy cross-correlation.

This result has implications of being able to constrain the distribution and evolution of the CGM. Recent simulations (Le Brun, McCarthy & Melin, 2015; Suresh et al., 2015) have shown that the feedback processes (from star formation and AGNs) can affect the density and temperature profiles of the CGM. These simulations match some of the observed properties of the CGM and galaxies. However, they are quite sensitive to the feedback mechanism used and give a variety of the CGM density and temperature profiles depending on the feedback process. The density profiles of the CGM in these simulations can be reasonably fit by $1.2 \leq \gamma_{\text{gas}} \leq 2.5$, within the virial radius of the galaxy for various feedback processes. For example, the No AGN, fixed- v hot winds and fully enriched winds models of Suresh et al. (2015) can be fit with $\gamma_{\text{gas}} = 2, 1.6$ and 2.2 respectively (excluding the central part). Also the pressure profile for the massive galaxies from Le Brun, McCarthy & Melin (2015) (see the first panel of Figure 3 of Le Brun, McCarthy & Melin 2015) can be fit with a $\gamma_{\text{gas}} \sim 1.25$, assuming the gas to be at the virial temperature. Therefore the X-ray-galaxy and SZ-galaxy cross power spectrum have the potential of discriminating between the evolutionary processes for the CGM, at greater than 3σ , if $\Delta\gamma_{\text{gas}}$ can be constrained within ~ 0.5 .

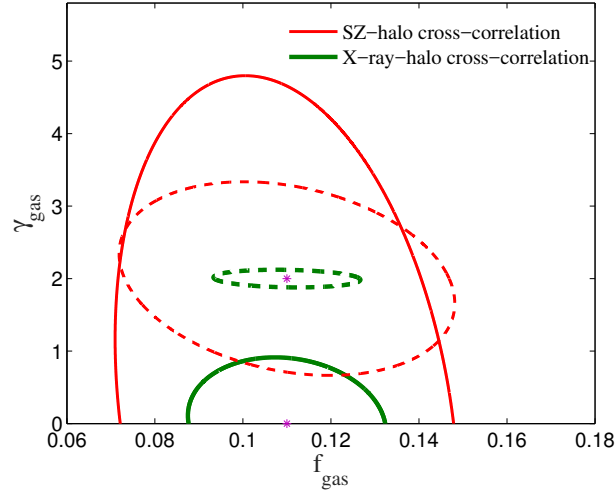


Fig. 3.10 The 68% CL contours for f_{gas} and γ_{gas} from the SPT-DES (SZ-galaxy cross power spectrum) and eROSITA-DES (X-ray-galaxy cross power spectrum) surveys. The solid thin red (thick green) ellipse is for the fiducial value $\gamma_{\text{gas}} = 0$ for the SZ (X-ray)-galaxy cross power spectrum and the dashed thin red (thick green) ellipse is for the fiducial value $\gamma_{\text{gas}} = 2$ for SZ (X-ray)-galaxy cross power spectrum. All the plots are for Prior-2 case with fixed α_{gas} .

3.8 Conclusions

We have studied the cross-correlation power spectra for the SZ-galaxy distribution, X-ray-galaxy distribution and X-ray-SZ effect for the hot gas in the galactic haloes. Our main conclusions are as follows:

1. We predict that the SZ-galaxy cross power spectrum is significant at small scales ($l \gtrsim 3000$) and can be detected at $\text{SNR} \sim 9$ by combining the SPT and DES surveys for the massive galaxies at intermediate redshifts. The shape of the SZ-galaxy cross-power spectrum is sensitive to the underlying distribution of the gas at large l -values ($l \approx 10^4$).
2. For the X-ray-galaxy cross power spectrum, we have considered the combination of the eROSITA-DES and eROSITA-LSST surveys and these surveys can detect the signal at $\text{SNR} \sim 6$ and 12 respectively for the high mass and intermediate redshift galaxies. For the flat density profile, the shape of the X-ray-galaxy cross power spectrum is similar to the shape of the SZ-galaxy cross power spectrum. However, the X-ray emission ($\propto n_e^2$) is more sensitive to the density profile than the SZ-effect ($\propto n_e$). As a result, the X-ray-galaxy cross power spectrum varies significantly with the steepening of the density profile even at $l \approx 3000$.

3. The possibility of detecting the X-ray-SZ cross power spectrum from the CGM is low ($\text{SNR} < 1$) for the SPT-eROSITA combination. This is due to the combined effect of the high noise in X-rays and low resolution of the SPT survey.
4. Finally, we do a Fisher matrix analysis for these surveys to forecast the constraints that can be derived on the amount of gas in the CGM. After marginalizing over the cosmological parameters with *Planck* priors and combining the Fisher matrix analysis for three different mass and redshift bin combinations, the SPT-DES survey can constrain f_{gas} to $\sim 34\%$ in the presence, and to $\sim 23\%$ in the absence, of any possible redshift evolution of the gas fraction. For the same set of mass and redshift bins, the eROSITA-DES survey can constrain f_{gas} to $\sim 23\%$ and $\sim 14\%$ in the presence and absence of redshift evolution of gas fraction respectively. Note that we neglect the correlation between the galaxies and the AGNs in the calculation of the uncertainties in the X-ray-galaxy cross-power spectrum.
5. Including the slope of the density profile γ_{gas} (defined in Equation 3.33) in the Fisher matrix analysis, degrades the constraints on other astrophysical parameters whereas γ_{gas} itself can be constrained to $\gamma_{\text{gas}} < 0.6$ (< 3.4) by the X-ray (SZ)-galaxy cross power spectrum for the flat density profile. These constraints are sensitive to the fiducial value of γ_{gas} and improve for a steeper density profile of the CGM. For $\gamma_{\text{gas}} = 2$, it can be constrained to $\Delta\gamma_{\text{gas}} < 0.1$ (< 1.0) by the X-ray (SZ)-galaxy cross power spectrum.
6. In all our calculations, we have assumed $f_{\text{gas}} = 0.11$. If instead, we take a low value of the gas fraction in the CGM, e.g. $f_{\text{gas}} \approx 0.05$, the SZ cross-power spectrum and its detectability goes down roughly by a factor 2 as the SZ signal is proportional to the amount of gas. So with $f_{\text{gas}} \approx 0.05$, the peak $\text{SNR} \sim 4-5$ for the SPT-DES survey. However, since the X-ray signal is proportional to n_e^2 , the X-ray cross power spectrum and its detectability goes down by a factor of 4. As a result, the SNR goes below 2 for the eROSITA-DES survey whereas this signal can still be detected at $\text{SNR} \sim 3$ with the eROSITA-LSST combination.

Presently, the amount of CGM in galactic haloes, its distribution, energetics and other properties are not well determined. Therefore, the detection and study of the SZ-galaxy and X-ray-galaxy cross power spectrum can provide powerful constraints on the nature of the CGM and open up the possibility of differentiating between various feedback models which affect the evolution of the CGM.

Chapter 4

Suppression of galactic outflows by cosmological infall and circumgalactic medium

Based on:

Singh, P., Rana, S., Bagla, J. S., Nath, B. B. 2016, MNRAS, 459, 2

We investigate the relative importance of two galactic outflow suppression mechanisms: a) Cosmological infall of the intergalactic gas onto the galaxy, and b) the existence of a hot CGM. We also discuss the impact of outflow suppression on the enrichment history of the galaxy and its environment.

Main Results

- Considering only radial motion, the infall reduces the speed of outflowing gas and even halts the outflow, depending on the mass and redshift of the galaxy.
- For star forming galaxies there exists an upper mass limit beyond which outflows are suppressed by the gravitational field of the galaxy. We find that infall can reduce this upper mass limit approximately by a factor of two (independent of the redshift).
- Massive galaxies ($\gtrsim 10^{12}M_{\odot}$) host large reservoir of hot, diffuse CGM around the central part of the galaxy. In this mass regime, CGM acts as a barrier between the infalling and outflowing gas and provides an additional source of outflow suppression.
- At low redshifts ($z \lesssim 3.5$), the CGM is more effective than the infall in suppressing the outflows.

4.1 Introduction

In previous chapters, we forecasted the detectability of SZ and X-ray signals from the CGM as well as the constraints on the properties of CGM. In this chapter, we address the question of interaction between outflows, infalling gas and CGM. The two components of matter in galaxies—dark matter and baryons—have contrasting properties, a fact which makes the study of galactic evolution a complex one. Unlike dark matter, baryons undergo collisions, radiate, and condense towards the central part of the galaxy in order to form stars. However, a significant fraction of these baryons may remain too hot to condense and form stars, especially in large galaxies. This gas likely stays in a hot, diffuse, gaseous form and envelopes the central, optically visible part of the galaxy (Rees & Ostriker, 1977; Silk, 1977), is referred to as the CGM.

Galaxies also undergo feedback processes like SNe and AGN which may give rise to galactic-scale outflows (Croton et al., 2006; Davé, Oppenheimer & Finlator, 2011; Vogelsberger et al., 2013). Simultaneously, the galaxies also accrete matter from their surrounding IGM (Birnboim & Dekel, 2003; Kereš et al., 2005; Oppenheimer et al., 2010). Together, the infall and outflows regulate the evolution of the host galaxies. However, the interaction between these two opposing processes is not yet well understood.

The CGM can also act as a barrier for infalling gas as well as the outflowing material if the CGM gas cooling timescale is comparable to or larger than the halo destruction timescale (Singh et al., 2015) leading to a hot, diffuse gaseous barrier between the central galaxy and IGM. Recent results of observations (Mathes et al., 2014) and simulations (Gördt & Ceverino, 2015; Gabor & Davé, 2015) can be explained by the existence of the hot CGM suppressing the outflows as well as infall. The outflows are generally metal rich and remove a significant amount of metal from galaxies. Since the outflows can be decelerated and even stopped by the hot CGM in massive galaxies, the recycling of metals in massive galaxies becomes more important as compared to the low mass galaxies. This mass dependent recycling behaviour is known as the differential wind recycling (Oppenheimer et al., 2010) and it can alter the metal evolution history of these galaxies and the surrounding IGM. For low mass galaxies ($M_h \lesssim 10^{12} M_\odot$), the gas cooling timescale is small compared the halo destruction timescale. As a result low mass galaxies cannot sustain the hot CGM gas. This gas cools down, form clumps and does not interfere much with in the infall/outflows. Whereas, in case of massive galaxies, the CGM gas remains hot for long enough timescale, leading to the existence of hot, gaseous barrier decelerating infalling (Dekel & Birnboim, 2006) as well as outflowing material. Therefore, the presence of the hot CGM divides the galaxies into two categories: 1). Massive galaxies ($M_h \gtrsim 10^{12} M_\odot$), where the CGM is hot enough to affect the physical properties (infall, outflows, metal enrichment etc.) of the

galaxy and the wind recycling becomes important, 2). low mass galaxies ($M_h \lesssim 10^{12} M_\odot$), where the CGM cools fast enough and is essentially invisible to the outflowing and infalling gas.

In this chapter, instead of focussing on the fate of infalling gas, we would like to study the effect of infalling gas and CGM on the outflowing gas. Can outflowing gas escape to the IGM, or is its ultimate mixing with the IGM suppressed? How does this suppression, if at all, depend on the galactic mass and redshift? The possible suppression of outflows is more important for low mass haloes where the hot CGM is essentially absent. For a given halo mass, there exists a redshift where the suppression of outflows by the presence of the hot CGM becomes more important than its suppression by infall. The relative importance of the two wind suppression mechanisms depends on the mass and redshift of the galactic halo. Therefore, it is important to take into account both the mechanisms to understand the galaxy evolution and enrichment.

However, the task is made a difficult one by the complications inherent in the physics of outflowing gas, and also in the complicated nature of infalling gas. Firstly, the outflowing gas may not be spherically symmetric and may have a complicated density, temperature and velocity structure, and this structure itself may be a function of time. Secondly, the infalling gas may also have an anisotropic density and velocity structure. One way to approach the problem is to use cosmological hydrodynamical simulations, which, however, is unlikely to help in understanding the physical processes involved, because of the complexity of the processes. The other approach is to set up idealised numerical experiments, in which certain parameters are varied keeping the others constant, and the processes are studied in detail. However, even before such an exercise, it is useful to study idealised theoretical scenarios with a mix of analytical and numerical tools. This is what we attempt here. In this chapter, for outflows, we use the analytical prescription by Sharma & Nath (2013a). For infall we use N-body simulations with TreePM code and $N = 512^3$ particles (Bagla, 2002; Khandai & Bagla, 2009). Used together, they allow us to arrive at a few interesting conclusions regarding the suppression of outflows by infalling matter and CGM, which may have important implications in the cosmological context.

This chapter is organized as follows: In Section 4.2 we describe the formalism used to calculate the infall and outflow velocities. In Section 4.3 we discuss the outflow suppression processes and estimate the relative importance of these processes. In Section 4.4 we discuss the impact of the suppression on the IGM enrichment and present our main conclusions in Section 4.6.

4.2 Formalism

4.2.1 Outflow velocity

The velocity of the outflowing gas mainly depends on the mass and redshift of the galactic halo and the feedback recipe considered. Sharma & Nath (2013a) derived the terminal velocity of outflows driven by multiple SNe in a galaxy whose dark matter profile is described by the Navarro-Frenk-White (NFW) profile. They showed that the wind speed at large galacto-centric distance depends on two velocity scales: (a) v_* , which depends on the mass and energy deposition rate due to SNe, and is given by $v_* \approx (\dot{E}/2\dot{M})^{1/2}$, and (b) v_s , which depends on the dark matter profile, and is closely related to the circular speed in a NFW profile. The terminal speed of winds (in the absence of momentum injection from AGN) was shown to be,

$$v_{\text{wind}}(r) = 2 \left[v_*^2 - \frac{1}{2} \left[\phi_{\text{NFW}}(r) - \phi_{\text{NFW}}(R) \right] \right]^{1/2} \quad (4.1)$$

where $R=200\text{pc}$ is assumed to be the sonic point, as well as the size of the region in which mass and energy is being injected and $\phi_{\text{NFW}}(r) = -2v_s^2 \frac{\ln(1+r/r_s)}{r/r_s}$ is the NFW gravitational potential. The terminal wind velocity ($r \rightarrow \infty$) is given by:

$$v_{\text{term}} = 2(v_*^2 - v_s^2)^{1/2} \quad (4.2)$$

The velocity scale inherent in the energy deposition is given by $v_* = 562\sqrt{\alpha}$ km/s, and it is due to effect of SNe, where α represents energy injection efficiency. The other velocity scale, $v_s = \sqrt{\frac{GM_h}{Cr_s}}$ is due to the gravity of the halo, where, M_h is the virial mass of the halo, $r_s = R_v/c$ is the scale radius of the halo, $C = \ln(1+c) - c/(1+c)$ and $c(M, Z)$ is the concentration parameter (Muñoz-Cuartas et al., 2011).

In Figure 4.1, we show the terminal wind velocity as a function of α , for the halo mass range $\sim 10^{10}\text{-}10^{13}h^{-1}M_\odot$, at $z=0$. For a given halo mass and redshift, the terminal wind velocity is close to zero below a particular value of α ($v_* < v_s$), beyond which there is a sharp increase in the wind velocity ($v_* > v_s$) and with further increase in α , the terminal velocity varies slowly ($v_{\text{term}} \propto \sqrt{\alpha}$).

Recent hydrodynamical simulations have shown that the efficiency of energy deposition by multiple SNe can be as large as ≈ 0.3 , which signifies that the rest of the energy is lost in radiation (Sharma et al., 2014b; Vasiliev, Nath & Shchekinov, 2015). These studies have investigated the radiative energy loss in the case of SNe that are separated in time and in space, but are coherent enough to mildly compensate for the radiative loss. This is also

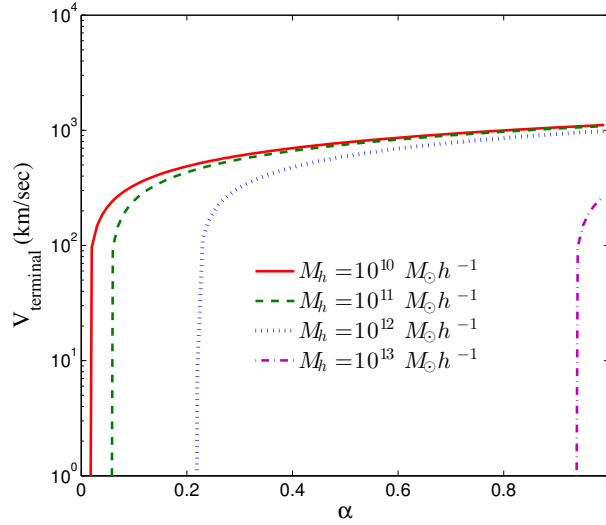


Fig. 4.1 Terminal wind velocity as a function of energy injection efficiency α , due to stellar feedback processes, for galactic haloes in the mass range, $10^{10-13} M_{\odot} h^{-1}$ (shown in different colors), at redshift, $z = 0$.

corroborated by inference from X-ray observations of outflows from M82 by Strickland & Heckman (2009). We fix the value of α at 0.3 for the rest of this work.

4.2.2 Infall velocity

We use gravity only simulations run with the TreePM code (Bagla, 2002; Khandai & Bagla, 2009) to compute the velocity of infalling gas under the assumption that the gas particles follow the dark matter particles. The suite of simulations used here is described in the Table 4.1. The cosmological model and the power spectrum of fluctuations corresponds to the best fit model for WMAP-5: $\Omega_{\text{nr}} = 0.26$, $\Omega_{\Lambda} = 0.74$, $n_s = 0.96$, $\sigma_8 = 0.79$, $h = 0.72$, $\Omega_{\text{B}} h^2 = 0.02273$ (Komatsu et al., 2009).

We use the Friends-of-Friends (FOF) (Davis et al., 1985) algorithm with a linking length $l = 0.2$ to identify haloes and construct a halo catalog. Velocity field around each halo is obtained from the same simulations.

The velocity field in the vicinity of haloes is highly anisotropic with infall often along filaments and sheets. We simplify the discussion here by considering only the radial motion around haloes, and also by averaging in all directions around haloes. This is an idealisation but should suffice to give us a glimpse of the relative role of infall and outflows.

In order to calculate the infall speed (and hence the net outflow speed), we divided the region around the halo into shells of thickness $R_{\text{vir}}/5$, where R_{vir} is the virial radius of

Table 4.1 The table lists the simulations used here. The first column lists the comoving size of the simulation box, the second column lists the minimum halo mass that we can resolve in the simulations, this is given in units of solar mass. Each simulation was run with 512^3 particles. Cosmological parameters used here are described in text.

L_{box} (Mpc)	M_{min} (M_{\odot})
51.2 h^{-1}	$10^{9.02}$
76.8 h^{-1}	$10^{9.43}$
153.6 h^{-1}	$10^{10.33}$

the halo. We calculate the average infall velocity of the shell by averaging over the radial velocity of the particles present in the shell. This gives the infall velocity of each shell as a function of distance from the centre of the halo. We then average this radial infall velocity for approximately ten randomly selected haloes for every mass scale and snapshot. This gives the average radial infall velocity as a function of halo mass and redshift.

4.3 Suppression of outflows

4.3.1 Suppression by infall

Subtracting the infall velocity from the radial outflow velocity gives the net outflow velocity. This approach ignores the effect of pressure and assumes a pure advection of outflow in the velocity field. Thus our estimate of the effect of infall on outflows is likely to be an under-estimate.

In Figure 4.2, we show the variation of the wind velocity and the net outflow velocity (wind velocity-infall velocity) as a function of the distance from the centre of the dark matter halo. We plot the ratio of distance from the centre to the virial radius of the halo on the x-axis, and the ratio of net outflow speed to $3 \times$ circular speed of the halo along the y-axis. We also show the root-mean-square error on the net outflow velocity. The main features of these plots are as follows:

- For a given redshift, the effect of infall increases with the increasing halo mass. This is mainly due to the increase in the gravitational field of the galaxy with its increasing mass, resulting in higher infall velocity.
- For a given halo mass, the effect of infall increases with the increasing redshift. This behaviour is due to the hierarchical formation history of the universe. Small galaxies

form early in the universe at high σ -peaks. These galaxies then grow through accretion and merger to form larger galaxies and galaxy clusters. The same halo mass corresponds to higher σ -peaks resulting in higher infall velocity at higher redshifts.

Thus, by neglecting the effect of infall one may over-predict the outflow velocity and hence the mass outflow rate.

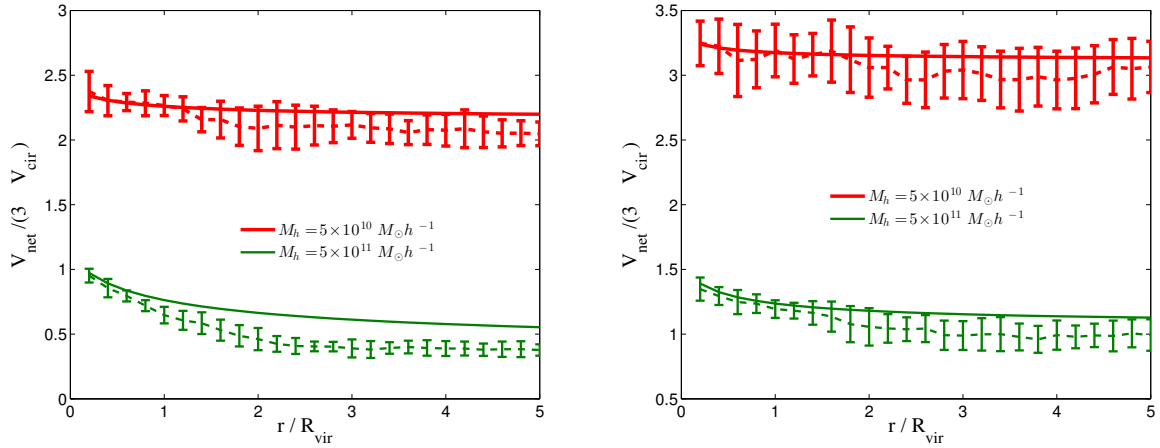


Fig. 4.2 Ratio of outflow velocity to $3 \times$ circular speed of the halo as a function of r/R_{vir} at $z=3.0$ (left panel) and $z=1.0$ (right panel). The thick red (thin green) solid line represents the unsuppressed wind velocity whereas the dashed line represents the net outflow velocity (wind velocity-infall velocity) for halo mass $M_h = 5 \times 10^{10} M_\odot h^{-1}$ ($M_h = 5 \times 10^{11} M_\odot h^{-1}$) at corresponding redshifts.

In Figure 4.3 we show the ratio of the net outflow velocity with and without taking into account the effect of infall. To find this ratio, we calculate the average radial velocity of the shells between R_{vir} and $2R_{\text{vir}}$, for different redshifts. For a given mass, the suppression of outflow due to the presence of infall increases with increasing redshift. This effect is more prominent for high mass haloes as compared to low mass haloes. For example, haloes with $M_h \sim 10^{10} h^{-1} M_\odot$, the difference in the suppression of the outflow due to infalling gas is $<10\%$ in the redshift range 0.5-5.0, whereas this difference increases to 20% at $M_h \sim 10^{11} h^{-1} M_\odot$ and 50% at $M_h \sim 2 \times 10^{11} h^{-1} M_\odot$. This variation is due to the decrease in the outflow speed and increase in infall speed with increasing halo mass. This results in the sharp decline in the net outflow speed near M_{max} , where M_{max} is the upper mass limit beyond which there are no effective outflows, as predicted by Equation 4.2. The vertical lines in Figure 4.3 show the values of M_{max} at different redshift. The curves in the figure shows that the infall effectively suppresses the outflows even for mass lower than M_{max} , effectively decreasing the value of M_{max} , beyond which outflows cannot reach the IGM. We find that the value of M_{max} decreases nearly by a factor of 2 due to the presence of infall.

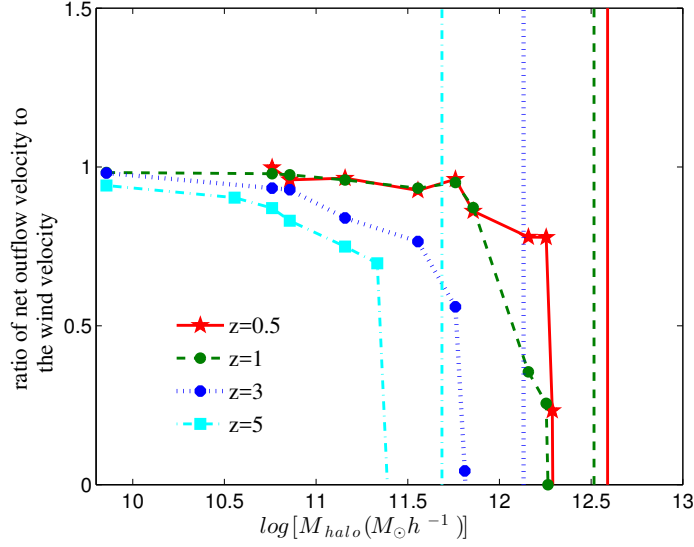


Fig. 4.3 Ratio of net outflow velocity with and without the infall, as a function of the halo mass, for different redshifts (shown in different colors). The vertical lines represent the mass limit above which the outflows cannot overcome the gravitational field of the galaxy and the galaxies do not host the outflows even in the absence of the infall.

Next, in Figure 4.4 we show M_{\max}^{infall} , the upper mass limit beyond which there are no effective outflows as function of redshift. M_{\max}^{infall} includes the effect of suppression of outflows due the presence of infall which decreases the value of M_{\max} approximately by a factor of two, independent of the redshift, as shown in Figure 4.3 and to illustrate this effect, we compare M_{\max} (thin dashed, brown line) with M_{\max}^{infall} as a function of redshift. In this figure, we also show the value of M_{\max}^{infall} when the infall velocity is calculated analytically from a spherical top hat model (thin solid, cyan line). It is interesting to find that the prediction of M_{\max}^{infall} from N-body simulation (dot-dashed, blue line) and spherical collapse model agree well with each other.

4.3.2 Suppression by hot CGM

In Figure 4.4, we also show M_{\max}^{CGM} (dotted, pink line), which is the mass limit above which the hot CGM exists in the galactic halo. This mass limit is determined by the condition $\frac{t_{\text{cool}}}{t_{\text{dest}}} > 1$, where t_{cool} is the halo gas cooling time and t_{dest} is the timescale in which a halo forms a larger halo through merger or accretion and the halo gas is reheated during the process (Singh et al., 2015). The gas cooling timescale is given by $t_{\text{cool}} = 3n_p k_b T / (2n_e^2 \Lambda(Z, T))$, where T is the gas temperature (assumed to be the virial temperature of the galaxy), n_e is

the electron density (computed assuming that the CGM contains approximately 10% of the total halo mass), $n_p (\sim \mu_e n_e / \mu)$ is the total particle density with μ and μ_e the mean molecular weight of the gas and per free electron respectively and $\Lambda(Z, T)$ is the cooling function (Sutherland & Dopita, 1993) which depends on gas temperature and metallicity. The metallicity of the CGM is assumed to be $\sim 0.1Z_\odot$. The value of M_{\max}^{CGM} is consistent with earlier studies by Birnboim & Dekel (2003) and Kereš et al. (2005). It changes only slightly with redshift and is comparable to M_{\max}^{infall} .

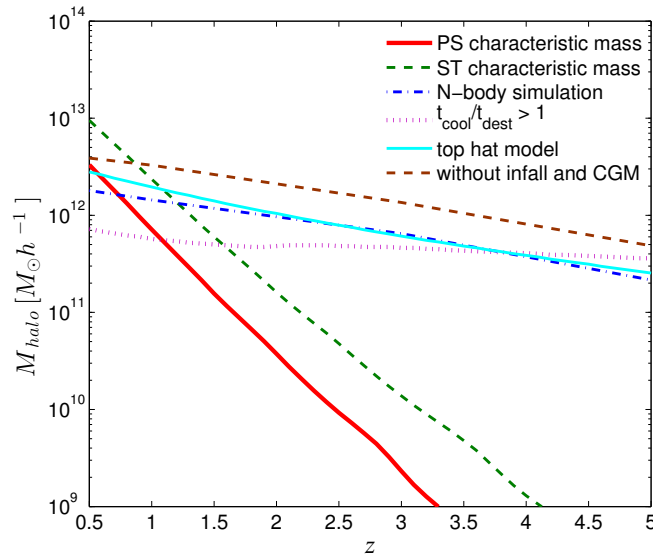


Fig. 4.4 Comparison between M_{\max} (thin dashed, brown line) which does not include the suppression of outflows by infall and CGM, M_{\max}^{infall} calculated for N-body simulation (dot-dashed, blue line) and the top hat model (thin solid, cyan line), M_{\max}^{CGM} (dotted, pink line) and M_{char} calculated for the PS (thick solid, red line) and ST (dashed, green line) mass function.

Recent simulations have found that for the haloes more massive than M_{\max}^{CGM} , the outflow speed is reduced to the sound speed in the CGM (Sarkar et al., 2015) due to the presence of hot environment around the central galaxy. This decelerates the outflow and even turns it around to form a galactic fountain.

The observations by Mathes et al. (2014) showed that the fraction of clouds escaping the galactic halo decreases with increasing halo mass. They studied a sample of 14 galaxies in the redshift range $0.1 < z < 0.7$ using the quasar absorption spectroscopy. The authors divided the galaxy sample into two mass bins: massive galaxies with $M_h > 10^{11.5} M_\odot$ and the low mass galaxies with $M_h < 10^{11.5} M_\odot$. The cloud escape fraction (within the virial radius of the galaxy) for the low mass galaxies is $\sim 55\%$ whereas the escape fraction decreases significantly to $\sim 5\%$ for massive galaxies. It is interesting to find that the dividing mass

limit between the two samples is comparable to M_{\max}^{CGM} determined in the present work. This observation supports the scenario of differential wind recycling where the hot halo gas in massive galaxies decelerates the outflowing clouds. For low mass galaxies $M_h \lesssim 10^{12} M_\odot$, the CGM cooling time is short (compared to halo destruction time), and, consequently, the gas pressure is not sufficient to support against gravity. As a result, the gas forms clumps, reducing its covering fraction and hence the efficiency to suppress outflows.

We note that, in addition to interfering with outflows, hot CGM forms a barrier in front of the infalling gas. In a recent study by Gabor & Davé (2015), the authors found the quenching of star formation due to the suppression of direct supply of the gas to the central galaxy, in the mass range $10^{12} - 10^{13} M_\odot$. The zoom-in hydrodynamic simulations by Goerdt & Ceverino (2015) predict that the gas infall velocity increases with increasing halo mass up to $M_h \approx 10^{12} M_\odot$ beyond which the infall velocity decreases as the halo mass is increased. Note that, the halo mass where the relation between the infall velocity and the halo mass is reversed, is independent of the galaxy redshift and its comparable to M_{\max}^{CGM} . This indicates that the presence of hot CGM decreases the infall velocity. However, Nelson et al. (2015b) found a significant suppression of the infall by the galactic winds at small r ($< 0.5R_{\text{vir}}$) but they did not find any change in accretion properties as a function of halo mass, in the mass range 10^{10} - $10^{12} M_\odot$. Note that this is still not in disagreement with differential wind recycling scenario if one uses $M_h \sim 10^{12} M_\odot$ as a dividing line between the galaxies with and without a hot circumgalactic environment.

4.3.3 Relative importance of infall versus hot CGM in suppressing outflows

The cosmological infall and the presence of hot CGM, both give the upper mass limits, M_{\max}^{infall} and M_{\max}^{CGM} respectively, beyond which the outflow is halted. If $M_{\max}^{\text{infall}} < M_{\max}^{\text{CGM}}$, the outflow is suppressed by the infall, even before the existence of the pressure supported, hot circumgalactic gas. In this scenario, the infall plays more important role than the CGM in suppressing the outflows. However, if $M_{\max}^{\text{infall}} > M_{\max}^{\text{CGM}}$, the galaxies host the hot CGM before the infall velocity becomes comparable to the outflow velocity. Therefore, the process corresponding to minimum of the two mass-limits, dominates the suppression. Comparing M_{\max}^{infall} and M_{\max}^{CGM} (see Figure 4.4) suggest that at low redshifts ($z \lesssim 3.5$), the role of hot CGM, in suppressing the outflows is more important than the infall, since $M_{\max}^{\text{infall}} > M_{\max}^{\text{CGM}}$, whereas at high redshifts where $M_{\max}^{\text{infall}} < M_{\max}^{\text{CGM}}$ ($z > 3.5$), infall suppresses the outflow more effectively than the CGM. The two mass limits are close in the redshift range considered. M_{\max}^{infall} is larger than M_{\max}^{CGM} by a factor of 2 – 3 near $z \sim 0$. The difference between the two

mass-limits decreases with increasing redshift. Therefore, these two processes give a mass range separating the haloes with and without effective outflows.

4.4 Fraction of galaxies affected by the suppression of outflows

The IGM is enriched by metals ejected by galaxies through galactic winds. Therefore, the enrichment level of IGM crucially depends on the feedback mechanism, which throws out metals into the IGM and the processes such as infall and the existence of hot CGM, which suppress the outflows. In this section, we examine whether the suppression of outflows by cosmological infall/hot CGM affects a significant fraction of the galaxy population.

In Figure 4.4, we also show the characteristic mass M_{char} for the Press-Schechter (PS) (defined as $\frac{\delta^2(z)}{2\sigma^2(M_{\text{char}})} = 1$) as well as Sheth-Tormen (ST) mass function ($\alpha_{\text{ST}} \frac{\delta^2(z)}{2\sigma^2(M_{\text{char}})} = 1$, where $\alpha_{\text{ST}} = 0.707$). The characteristic mass, M_{char} represents the mass scale beyond which the number of haloes decreases rapidly with increasing halo mass. Therefore, the haloes with masses below M_{char} , dominate the halo population. The present day value of $M_{\text{char}} \sim 1.4 \times 10^{13} h^{-1} M_{\odot}$ for Press-Schechter mass function and it decreases with increasing redshift as expected from the hierarchical structure formation scenario. We find that at $z > 1 - 2$, $M_{\text{max}}^{\text{infall}}$ and $M_{\text{max}}^{\text{CGM}} > M_{\text{char}}$, which implies that the haloes in which outflows are completely suppressed by infalling gas or the presence of the hot CGM, are rare. At low redshifts, majority of the haloes lie near the characteristic mass range, and therefore outflow suppression becomes important. Therefore, the suppression of the outflows due the infall as well as the hot CGM should be taken into account while dealing with the haloes hosting outflows, especially at low redshifts.

Next, to get an estimate of the population of galaxies with suppressed or unsuppressed outflows, we compute the ratio of the total mass in the galaxies hosting unsuppressed outflows to the total mass present in collapsed structures. In Figure 4.5, we show this ratio as a function of redshift. The total mass in the collapsed structures is estimated using the N-body simulation. To compute the mass in the haloes supporting outflows, we consider haloes with $M_{\text{h}} \lesssim \text{Min}[M_{\text{max}}^{\text{infall}}, M_{\text{max}}^{\text{CGM}}]$. Note that, while calculating the number of galaxies with unsuppressed outflows, we exclude those haloes in which outflows are *completely* suppressed. Therefore, the ratio includes galaxies with partially suppressed outflows.

Given that the mass resolution of simulations used in this study is different, and that simulations with a larger box-size are required for low redshift studies (Bagla & Prasad, 2006), the mass resolution is not independent of redshift in the analysis. The mass resolution

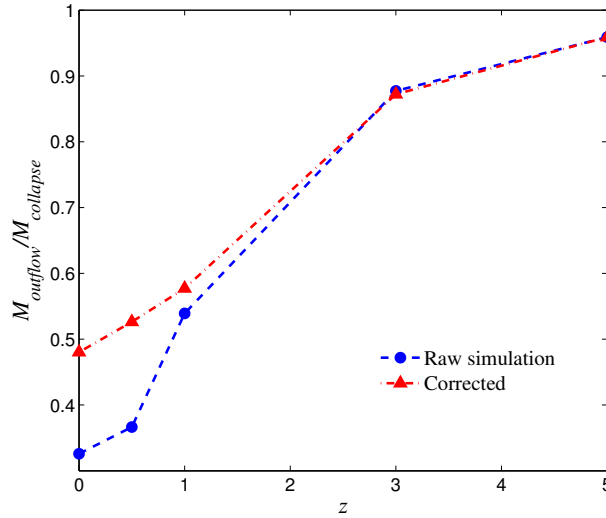


Fig. 4.5 The ratio of mass in haloes hosting unsuppressed outflows to the total mass in all collapsed structures. The blue curve (dashed) shows the ratio as determined in N-Body simulations. Given that we use simulations with different mass resolution and we are unable to resolve low mass haloes in simulations used at low redshifts, this approach under-estimates the ratio. The red curve (dot-dashed) is obtained by applying a correction by extrapolating the mass function to the same mass resolution as is available in the simulations used for high redshift snapshots. The qualitative trend remains the same though the ratio has the value closer to 0.5 rather than 0.3.

is poorer at low redshifts and therefore we miss out on low mass haloes that can potentially contribute to outflows. To overcome this problem, we compute the mass function at each redshift and extrapolate it to the mass resolution of the highest resolution simulation used here. The red curve (dot-dashed) in Figure 4.5 incorporates this correction while computing the ratio of total mass in galaxies that have an unsuppressed outflow to the total mass in collapsed haloes.

The ratio is close to unity at high redshifts ($z \gtrsim 5$) due to the hierarchical formation history of the universe, the haloes at high redshifts are mostly low mass ones. The fraction of mass present in the outflow-supporting haloes decreases with decreasing redshift due to the formation of massive haloes at low redshifts. The redshift range, $z \sim 1 - 2$, represents the era of high star formation activity. Hence, the abundance of outflow supporting systems can potentially determine the enrichment history of the galaxies, CGM and IGM. We find that the ratio $M_{\text{outflow}}/M_{\text{collapse}}$ decreases from 70% to 60% in this redshift range. Thus, a small but significant fraction of haloes lie in the mass range where the outflows are completely suppressed by the infall or the presence of the hot CGM during the era of high star formation hence high feedback activity. In the redshift range $z < 1$, $M_{\text{outflow}}/M_{\text{collapse}}$ decreases from

60% to less than 50%. Since, the presence of the hot CGM is more important at low redshifts (see Figure 4.4), the outflowing gas in approximately half of the haloes at low redshift, is decelerated and suppressed by the surrounding CGM in these galactic haloes.

Therefore, the enrichment of the IGM is easier at high redshifts whereas at low redshifts, the metal carrying outflows are suppressed more effectively, mostly by the hot CGM. These suppressed outflows are then recycled into the galaxy hence enriching the CGM as well as the stars. This result is in agreement with the simulation result of Davé & Oppenheimer (2007), indicating that the IGM contains more metals at high redshifts whereas the stars and the halo gas contain more metals at low redshifts.

4.5 Caveats

The usefulness of our results discussed above is, however, subject to certain caveats. Firstly, the geometry of the infalling gas near the virial radius may not be isotropic as we have assumed, and is likely to be in the form of streams (Dekel, Sari & Ceverino, 2009; Dekel et al., 2009). Simulations show that gas mainly flows along filaments in the cosmic web, and the enhanced density of gas in the filaments causes it to cool, and avoids being shocked to the virial temperature (Birnboim & Dekel, 2003). Considerations of such cold streams with regard to the fraction of outflowing gas that can escape is difficult without hydrodynamical simulations, and beyond the scope of the present work. However, we note that the cold mode of accretion dominates galaxies below the mass scale of $\sim 10^{12} M_{\odot}$, and the mode of accretion changes to that of slow cooling from hot halo gas (hot mode) beyond this mass scale (Kereš et al., 2005). The shock heating and disruption of cold infalling streams, especially at high redshifts and low galacto-centric radii, becomes more important near $M_h \sim 10^{12} M_{\odot}$ (Danovich et al., 2012; Nelson et al., 2013; Danovich et al., 2015; Gabor & Bournaud, 2014; Nelson et al., 2015a). This mass scale coincides with the mass scale shown in Figure 4.4 (dotted pink line corresponding to the galactic haloes with $t_{\text{cool}}/t_{\text{dest}} > 1$), and therefore the filamentary nature of cold flows in low mass galaxies does not significantly alter our conclusions.

Secondly, all of the CGM gas may not be in a hot, diffuse state, and a fraction of it is likely to be in a warm ($\sim 10^4$ K) phase, as indicated by the COS-Halos survey (Werk et al., 2014). It is also believed that the interaction of the CGM gas with the outflows driven by first phases of star formation may cause clumping (Marinacci et al., 2010; Sharma et al., 2014b). The gas in the interaction zone may suffer from various instabilities, such as thermal instability (due to the mixing of gas at different temperatures and densities) and Kelvin-Helmholz instability (due to shear). The resulting structures and turbulence in the

CGM may allow some fraction of the outflowing gas to escape, in the cases where our results above for a homogeneous CGM may not allow any escape. However, this fraction is difficult to estimate without the aid of hydrodynamic simulations.

However, given these uncertainties, it is interesting to note the similarities of the mass scale we have discussed so far, that of $M_{\text{max}}^{\text{infall}}$, with other mass scales that are significant for galaxy evolution. Several studies (e.g, Behroozi, Wechsler & Conroy 2013) have shown that the ratio of baryonic mass to the total mass of galaxies reaches a maximum around $\sim 10^{12} M_{\odot}$ at the present epoch, and slightly lower at high redshift (e.g., lower by a factor of ~ 3 at $z \sim 4$). This is remarkably close to the mass scale $M_{\text{max}}^{\text{infall}}$ shown in Figure 4.4 (dot-dashed blue line and thin solid cyan line). We can speculate, on the basis of our calculations here, that the stoppage of the outflow is causally connected to the baryon-to-total mass ratio. The analytic work of Sharma et al. (2014b), which did not consider the effect of infall or the presence of CGM, and only considered the effect of gravity, has already suggested that the stoppage of outflow is related to the baryons-to-total mass ratio. Our work on the effect of infall and CGM's presence provides additional supports for this scenario.

4.6 Conclusions

In this work, we have studied the relative importance of galactic outflows, cosmological infall and the role of presence of hot circumgalactic gas on these processes under some simplified assumptions such as spherically symmetric infall, constant value of energy injection efficiency, and gas particles following the dark matter particles. We have also neglected the complexities involved in the dynamics and distribution of the CGM as well as the infalling gas. However, as discussed in Section 4.5, the detailed treatment of these complexities is unlikely to change the conclusions drawn from our analysis substantially. Our conclusions can be summarised as follows:

1. Without considering the CGM, the infalling gas interferes with the outflowing gas reducing the net outflow velocity. This reduction depends on the mass and redshift of the galaxy. The larger (massive) galaxies at high redshifts suffer more suppression compared to smaller (low mass) galaxies at low redshifts due to the combined effect of weaker outflows and stronger infall in the case of massive galaxies.
2. Even in the absence of any infall, there exists an upper mass limit beyond which the outflows are unable to overcome the gravitational field of the galaxy. This upper mass limit decreases roughly by a factor of two due to the additional suppression of outflows by infalling gas, independent of the redshift. The value of this upper mass

limit, M_{\max}^{infall} , predicted by simulations agrees well with the value predicted by the top-hat model.

3. In addition to the infall, the presence of the hot gaseous environment in the form of CGM, decelerates the outflows. The CGM also gives an upper mass limit, M_{\max}^{CGM} , beyond which the hot CGM effectively stops the outflows from escaping the galaxy. The hot CGM may also reduce the direct supply of infalling gas to the central part of the galaxy. We estimate M_{\max}^{CGM} under the condition that the gas cooling time exceeds the halo destruction timescale. M_{\max}^{CGM} varies slowly with the redshift with its value $\sim 10^{12}M_{\odot}$ in the redshift range 0 – 5.
4. The hot CGM is more effective than the infall in the low redshift range 0-3.5 in counteracting the outflows whereas the infall becomes more effective at high redshift ($z > 3.5$). The upper mass limits, for suppressing the outflows, predicted by both the processes are comparable and together determine the fate of the outflowing gas.
5. Comparison of M_{\max}^{CGM} and M_{\max}^{infall} with the characteristic mass predicts the suppression of the outflows to be important at low redshifts ($z < 1 - 2$), where the galaxies with completely suppressed outflows constitute a significant fraction of the overall galaxy population. The fraction of galaxies with unsuppressed outflows predicted by the simulation decreases from $\sim 90\%$ at $z = 5$ to $\sim 50\%$ at $z = 0$. This fraction is of order 60-70% in the era of high star formation and hence high feedback activity ($z \sim 1 - 2$), likely affecting the enrichment history of the universe.

Chapter 5

Constraining the X-ray AGN halo occupation distribution: implications for eROSITA

Based on:

Singh, P., Refregier, A., Majumdar, S., Nath, B. B. 2017, MNRAS, 466, 3961

The X-ray emission from AGN is a major component of extragalactic X-ray sky. In this thesis, we use the X-ray luminosity function (XLF) and halo occupation distribution (HOD) formalism to construct a halo model for the X-ray emission from AGNs. We compute the auto-correlation power spectrum in the soft X-ray band (0.5-2 keV) due to the AGNs potentially resolved by eROSITA mission and explore the redshift and mass dependence of the power spectrum. We also forecast the potential of X-ray auto-correlation power spectrum and X-ray-lensing cross-correlation power spectrum using eROSITA and eROSITA-LSST surveys, respectively, to constrain the HOD parameters and their redshift evolution. In addition, we compute the power spectrum of the AGNs lying below the flux resolution limit of eROSITA, which is essential to understand in order to extract the X-ray signal from the hot diffuse gas present in galaxies and clusters.

Main Results

- The two inputs (XLF and HOD) are in agreement with each other, especially in the redshift range $0.5 \lesssim z \lesssim 3.5$.
- The dominant contribution to the resolved AGN luminosity and redshift distribution comes from $L_X \sim 2 - 3 \times 10^{44} \text{ergs}^{-1}$ and $z \sim 1.2$.
- At multipoles $l \lesssim 1000$ (i.e. large scales), the clustering term of the resolved AGN auto power spectrum is larger than its Poisson term.
- In case of unresolved AGNs, the clustering term is larger than Poisson term at $l \lesssim 2000$.
- Without any priors, the AGN X-ray auto power spectrum poorly constraints the HOD model parameters for eROSITA survey.
- The uncertainty in HOD model parameters decreases by an order of magnitude by including X-ray-lensing cross power spectrum for eROSITA-LSST survey combination.

5.1 Introduction

In previous chapter, we discussed the importance of CGM in determining the fate of outflowing and infalling gas, and hence in galaxy evolution. In Chapter 3, we showed that X-ray emission from the CGM is a powerful probe of distribution and energetics of the CGM. However, AGNs are the major component of extragalactic X-ray emission (Softan, 2007), and needs to be modelled well to extract the X-ray emission from any other component of the X-ray sky. Therefore, studying X-ray emission from AGNs is crucial to understand the origin and evolution of AGNs as well as to extract the X-ray signal from the subdominant components such as CGM and ICM.

Almost every galaxy with a central bulge contains a supermassive black hole (SMBH) ($M_{\text{SMBH}} \gtrsim 10^6 M_{\odot}$) at its centre (Kormendy & Richstone, 1995; Ferrarese & Merritt, 2000). The SMBH acquires such a large mass through accretion of matter from its surrounding and the merger of the host galaxies. These processes trigger the AGN phase of the SMBH during which the accretion rates are high and the accreting material emits a large fraction of its rest energy. The luminosity of the AGN may surpass the total light from the galaxy and drive strong galactic outflows. The evidence of such a feedback from the AGN is present in massive galaxies, groups and clusters. Simulations (Omma et al., 2004; Springel, Di Matteo & Hernquist, 2005; McNamara & Nulsen, 2007; Puchwein, Sijacki & Springel, 2008; Battaglia et al., 2010; McCarthy et al., 2010) as well as analytical studies (Valageas & Silk, 1999; Bower et al., 2001; Cavaliere, Lapi & Menci, 2002; Sharma & Nath, 2013b) show that, in the absence of any AGN feedback, it is difficult to reproduce various observations such as the gas mass fractions, X-ray luminosity scaling relations, heating of cooling flows of galaxy clusters, gas pressure profiles. The cluster gas entropy also holds key to AGN feedback, which can be directly linked to the non-gravitational energy deposited and remaining in the intracluster medium (Chaudhuri, Nath & Majumdar, 2012; Chaudhuri, Majumdar & Nath, 2013; Iqbal et al., 2016). These studies give indirect but strong evidence of the presence of AGN and support the importance of AGN driven feedback in the evolution of galaxies.

In addition to giving rise to the outflows, AGNs are strong X-rays emitters and form a dominant part of the extragalactic X-ray sky. eROSITA, which is a future X-ray satellite with all sky coverage will provide a large sample of X-ray AGNs (Merloni et al., 2012; Kolodzig et al., 2013a). It will also cover a significant range of angular scales due to its large sky coverage and improved angular resolution ($\sim 30''$ in 0.5-2 keV band) compared to ROSAT all-sky survey (RASS), which was the last all-sky X-ray survey with mean point spread function $\sim 2'$ (La Barbera et al., 2009).

In this chapter, we first compute the angular auto-correlation power spectrum of the X-ray emission coming from AGNs, which are expected to be resolved by eROSITA survey, using a halo model approach. There are two main ingredients of this approach: 1) a model that describes the X-ray emission from AGNs. It can be obtained using the X-ray luminosity function (XLF) of AGNs which represents the luminosity distribution of AGNs as a function of redshift. Here we use the XLF given in Aird et al. 2015 (hereafter A15). 2) We also need a model that describes how AGNs populate a dark matter halo (DMH). Large efforts have been invested into probing how the DMH affect the distribution and energetics of AGNs (Croom et al., 2004; Gilli et al., 2005; Krumpel et al., 2012; White et al., 2012; Koutoulidis et al., 2013; Mountrichas et al., 2013; Allevato et al., 2014; Gatti et al., 2016). The clustering measurements of X-ray AGNs suggest that AGNs occupy haloes in the mass range $\sim 10^{12.5} - 10^{13.5} h^{-1} M_{\odot}$ (Coil et al., 2009; Cappelluti et al., 2010; Allevato et al., 2011; Leauthaud et al., 2015). AGN clustering measurements can also be used to construct the halo occupation distribution (HOD) model of AGNs (Miyaji et al. 2011; Allevato et al. 2012; Richardson et al. 2013, hereafter R13). In this formalism, the number of AGN (central+satellite) is modelled in terms of the mass of the host DMH. The HOD analysis describes how AGNs populate the DMH, which can be used to construct the AGN power spectrum. Specifically, we use the HOD model described in R13. This HOD model, however, lacks a redshift dependence, which is expected from the redshift dependence of AGN XLF and the host halo properties. Here, we study the constraints that can be put on the redshift evolution of the HOD model with eROSITA and LSST (LSST Science Collaboration et al., 2009). using the X-ray auto-correlation power spectrum and X-ray-lensing cross-correlation power spectrum of the resolved AGN. The choice of the X-ray-lensing cross-correlation power spectrum is motivated by the fact that the HOD formalism connects the distribution of the AGNs with the host DMH mass and lensing signal is direct tracer of the mass. We also compute the angular power spectrum of the unresolved AGNs which are expected to contribute to the diffuse X-ray background of eROSITA and contaminate the angular power spectrum due the ICM/CGM in the 0.5-2 keV X-ray band.

This chapter is organised as follows. In Section 5.2, we describe the methodology and various ingredients required for the calculation of X-ray power spectrum from the resolved AGNs, and show the redshift and halo mass dependence of the power spectrum. In Section 5.3, we forecast the constraints on the HOD parameters and their redshift evolution. In Section 5.4, we describe the X-ray-lensing cross power spectrum and its power to put stringent constraints on HOD model parameters. In Section 5.5, we compute the X-ray auto-correlation power spectrum due to the unresolved AGNs, its redshift and halo mass

dependence. Finally, we summarise our main conclusions in Section 5.6. The cosmological parameters used in this chapter are taken from Planck Collaboration et al. (2015a).

5.2 Auto-correlation power spectrum of the resolved AGNs

Given a signal $x(\theta, \phi)$, its angular power spectrum is given by (eg. Hivon et al. 2002; Molinari et al. 2014),

$$C_l = \frac{1}{2l+1} \sum_{m=-l}^{m=l} |a_{lm}|^2 \quad (5.1)$$

where, $a_{lm} = \int d\Omega x(\theta, \phi) w(\theta, \phi) Y_{lm}^*(\theta, \phi)$, $w(\theta, \phi)$ is the mask (decided by the sky coverage of the survey with low foreground and low instrumental noise) and Y_{lm}^* are the spherical harmonic functions. There are also other corrections applied to the above power spectrum due to the partial sky coverage of the survey which is generally the case.

Presently, due to the small sky coverage of the ongoing X-ray surveys, the clustering of AGNs are usually studied only through their two-point correlation function (2PCF). But, with the launch of eROSITA, it will be possible to explore the power spectrum of these AGNs in great detail. Therefore, we choose to deal with the number weighted power spectrum of AGNs that are expected to be resolved by eROSITA i.e. AGNs lying above the flux resolution limit of eROSITA. We assume that all AGNs above the flux limits $\sim 1.5 \times 10^{-14} \text{erg s}^{-1} \text{cm}^{-2}$ and $1.8 \times 10^{-13} \text{erg s}^{-1} \text{cm}^{-2}$ in 0.5-2 keV (soft) and 2-10 keV (hard) X-ray bands, respectively, will be resolved by eROSITA.

For resolved AGNs, $x(\theta, \phi)$ represents the AGN number counts, whereas in the case of unresolved AGNs, it represents unresolved X-ray flux. In reality, the observed signal also contains contribution from many other sources and one has to carefully remove the noise to get the desired power spectrum. In this chapter, we show the analytical estimate of the angular power spectrum calculated using halo model approach. In this approach, the AGN power spectrum is represented by the total contribution of the AGNs residing in a halo, convolved with the DMH mass function, integrated over mass and redshift, as a function of multipole l . The AGN angular auto-correlation power spectrum is the sum of two terms,

$$C_l^{\text{AGN}} = C_l^{\text{AGN,P}} + C_l^{\text{AGN,C}} \quad (5.2)$$

where $C_l^{\text{AGN,P}}$ and $C_l^{\text{AGN,C}}$ are the Poisson and clustering terms, respectively.

5.2.1 Poisson term

The Poisson term (independent of l ; also known as shot noise) of the AGN angular auto-correlation power spectrum is given by

$$C_P^{\text{AGN}} = \int dz \frac{dV}{dz d\Omega} \int d \log L_X \phi_{\text{AGN}}(L_X, z) \quad (5.3)$$

The above equation also represents the number of AGNs per unit solid angle. Here $\phi_{\text{AGN}}(L_X, z)$ is the XLF and L_X is the X-ray luminosity of the AGN (in the hard X-ray band) related to the observed X-ray flux (in the soft X-ray band) S_X by,

$$L_X = \frac{4\pi d_L^2(z) S_X}{(1+z)^{2-\Gamma}} \frac{E_{\text{max,RF}}^{2-\Gamma} - E_{\text{min,RF}}^{2-\Gamma}}{E_{\text{max,obs}}^{2-\Gamma} - E_{\text{min,obs}}^{2-\Gamma}} \quad (5.4)$$

where $d_L(z)$ is the luminosity distance, Γ is the AGN spectral index (assuming that the AGN X-ray emission follows a power law spectrum), $E_{\text{max,RF}}$ and $E_{\text{min,RF}}$ are the upper and lower limit of the X-ray band in the rest frame of the AGN, respectively, whereas, $E_{\text{max,obs}}$ and $E_{\text{min,obs}}$ correspond to the observed X-ray band. The lower luminosity limit in above integral is determined by the sensitivity limit of the telescopes, which is $\sim 1.5 \times 10^{-14} \text{erg s}^{-1} \text{cm}^{-2}$ and $1.8 \times 10^{-13} \text{erg s}^{-1} \text{cm}^{-2}$ for soft and hard X-ray bands, respectively.

5.2.2 AGN XLF

The AGN XLF is defined as the comoving number density of AGNs per unit logarithmic X-ray luminosity, i.e. $\phi_{\text{AGN}}(L_X, z) = dn/d \log_{10} L_X$. To compute it, we use the Luminosity And Density Evolution (LADE) model (see A15 for the details of the model), which gives

$$\phi_{\text{AGN}}(L_X, z) = K(z) \left[\left(\frac{L_X}{L_*(z)} \right)^{\eta_1} + \left(\frac{L_X}{L_*(z)} \right)^{\eta_2} \right]^{-1}, \quad (5.5)$$

where $K(z) = K_0 \times 10^{d(1+z)}$ and $L_*(z) = L_0 \left[\left(\frac{1+z_c}{1+z} \right)^{p_1} + \left(\frac{1+z_c}{1+z} \right)^{p_2} \right]^{-1}$. The values of the model parameters are shown in Table 5.1. Note that this XLF corresponds to luminosities integrated in the hard X-ray band in the rest frame of the AGN. Therefore, one has to take into account the band correction (see Equation 5.4) to estimate the XLF in different X-ray bands.

The differential number counts i.e. the number of AGNs per unit flux and solid angle in the soft band is

$$\frac{dN}{dS_X d\Omega} = \frac{1}{S_X \ln 10} \int dz \frac{dV}{dz d\Omega} \phi_{\text{AGN}}(L_X, z), \quad (5.6)$$

Table 5.1 LADE model parameters.

Parameter	Soft X-ray band	Hard X-ray band
$\log K_0(\text{Mpc}^{-3})$	-4.28	-4.03
$\log L_0(\text{erg s}^{-1})$	44.93	44.84
γ_1	0.44	0.48
γ_2	2.18	2.27
p_1	3.39	3.87
p_2	-3.58	-2.12
z_c	2.31	2.00
d	-0.22	-0.19

where $dV/dz d\Omega$ is the differential comoving volume. We compare the AGN differential number counts calculated using the LADE model with the observed number counts (Mateos et al., 2008) for soft as well as hard X-ray band in Figure 5.1. We take $\Gamma = 1.7$ for soft and 2.0 for the hard X-ray band. There is a good agreement between the observed AGN counts and the LADE model.

In the left-hand panel of Figure 5.2, we show the redshift distribution of AGNs that are expected to be observed by eROSITA in the soft as well as the hard X-ray band. The soft and hard band AGN number counts get maximum contribution from AGNs near $z \sim 1.2$ and 0.2, respectively. The hard band AGNs are less concentrated near the peak than the soft band AGNs with a hint of another peak near $z \sim 1.2$. Beyond $z \sim 4$, the number of resolved AGNs becomes negligible.

In the right-hand panel of Figure 5.2, we show the luminosity distribution of the resolved AGNs in the soft and hard X-ray bands. In the soft band, the luminosity distribution peaks at $L_X \sim 10^{44.5} \text{erg s}^{-1}$. In the hard band, the peak is at smaller X-ray luminosity, $L_X \sim 10^{43.4} \text{erg s}^{-1}$. Again, the hard X-ray AGNs have a much broader luminosity distribution compared to the soft X-ray AGNs. In both the bands, negligible fraction of the total resolved AGN population lies outside the luminosity range $L_X \sim 10^{41} - 10^{47} \text{erg s}^{-1}$.

Note that, the prediction of redshift and luminosity dependence of the AGNs crucially depend on the choice of the XLF. Different XLFs, though broadly consistent with each other, give rise to different shapes and peak values of the AGN redshift and luminosity distributions (see Figure 10 of Kolodzig et al. 2013b). Also, our default XLF (A15) describes the AGN in 2-10 keV rest frame and for simplicity we use the power law approximation to get the soft band XLF, neglecting the effect of evolving fraction of absorbed and unabsorbed AGNs, which may affect the overall redshift distribution of the AGNs. Our choice of XLF is motivated by the reasonable reproduction of AGN number counts (shown in Figure 5.1) and

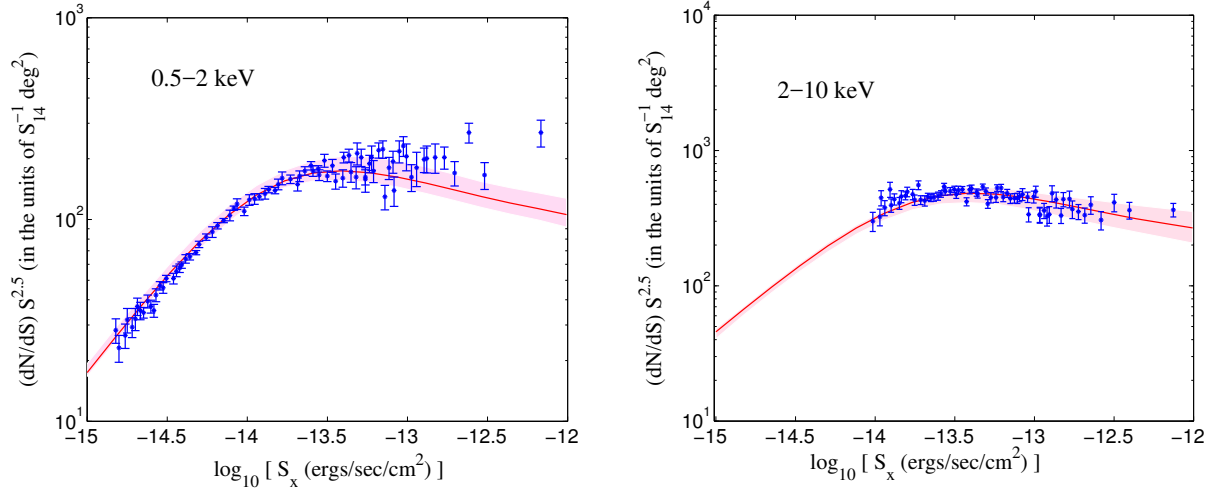


Fig. 5.1 The observed differential number counts of X-ray AGNs (blue points with error bars) from Mateos et al. (2008) against the prediction of the XLF (solid red line) in the soft (left panel) and the hard (right panel) X-ray bands. In both the panels, the shaded region represents the $3\text{-}\sigma$ uncertainty in the prediction of the XLF.

its consistency with the HOD model used in this chapter (discussed later in Section 5.2.3). We have also found a good agreement between the predictions of redshift distribution of the soft band AGNs using A15 and Ebrero et al. (2009) XLFs, where the author use the luminosity function for the 0.5–2 keV observed band. The luminosity distribution of the soft band AGNs estimated using A15 is more consistent with the prediction of AGN XLF by Miyaji, Hasinger & Schmidt (2000). The possible reasons for the disagreement between various AGN XLFs are described in detail in section-5.3 of Kolodzig et al. (2013b).

5.2.3 Clustering term

The clustering term of the AGN angular auto-correlation power spectrum can be further divided into two terms (Mo, van den Bosch & White, 2010; Miyaji et al., 2011; Helgason et al., 2014),

$$C_l^{\text{AGN,C}} = C_l^{\text{AGN,1h}} + C_l^{\text{AGN,2h}} \quad (5.7)$$

where $C_l^{\text{AGN,1h}}$ is due to the correlation between AGNs within the same halo and $C_l^{\text{AGN,2h}}$ is due to the correlation between AGNs residing in different haloes.

2-halo clustering term

The contribution of clustering term to the AGN angular auto-correlation power spectrum due to the correlation between AGNs residing in different haloes (under flat sky approximation)

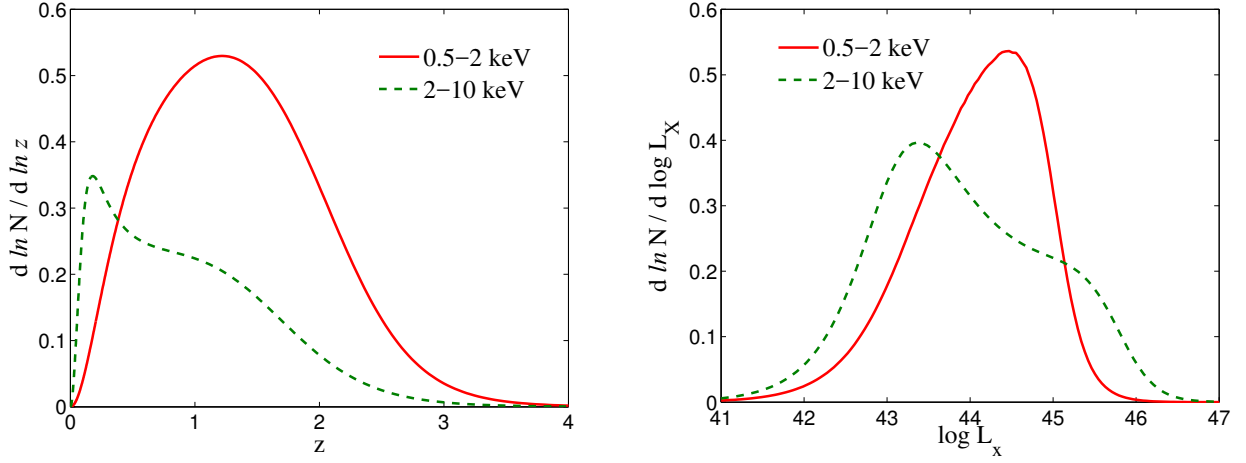


Fig. 5.2 Left-hand panel: the differential redshift distribution of the AGNs expected to be resolved by eRASS in the soft (solid red line) and the hard (dashed green line) X-ray bands. Right-hand panel: Same as left panel but for the luminosity distribution of resolved AGNs.

is

$$C_l^{\text{AGN},2h} = \int dz \frac{dV}{dz d\Omega} P_{\text{AGN}}^{2h} \left(k = \frac{l}{\chi(z)} \right) [W^{\text{AGN}}(z)]^2 \quad (5.8)$$

where $\chi(z)$ is the comoving distance,

$$P_{\text{AGN}}^{2h}(k) \approx P_{\text{lin}}(k) \left[\int dM \frac{dn}{dM} b_h(M, z) \left(\frac{\langle N_c(M) \rangle + \langle N_s(M) \rangle f_{\text{AGN}}(k, M, z)}{\bar{n}_{\text{AGN}}} \right) \right]^2 \quad (5.9)$$

and

$$W^{\text{AGN}}(z) = \int d \log L_X \phi_{\text{AGN}}(L_X) \quad (5.10)$$

where $P_{\text{lin}}(k)$ is the linear matter power spectrum, $b_h(M, z)$ is the linear bias parameter, \bar{n}_{AGN} is the average comoving number density of the AGNs, $\langle N_c(M) \rangle$ and $\langle N_s(M) \rangle$ are the average numbers of central and satellite AGN residing in a halo of mass M , respectively, $f_{\text{AGN}}(k, M, z)$ (defined such that, $f_{\text{AGN}}(k, M, z) \rightarrow 1$ at large scales) is the Fourier transform of the normalized AGN distribution within a halo and its given by,

$$f_{\text{AGN}}(k, M, z) = \int dr 4\pi r^2 n_{\text{AGN}}(r) \frac{\sin(kr)}{kr} \quad (5.11)$$

where $n_{\text{AGN}}(r)$ is the radial distribution of the satellite AGN, normalized such that its volume integral within the virial radius of the halo is unity. In Figure 5.3, we show $n_{\text{AGN}}(r)$ for $M_h = 10^{14} h^{-1} M_\odot$ at $z = 0$ which is assumed to be given by the Navarro-Frenk-White (NFW) profile (Navarro, Frenk & White, 1997) with a concentration parameter (R13 and references therein),

$$c_{\text{AGN}}(M, z) = \frac{32}{(1+z)} \left(\frac{M}{M_{\text{ch}}} \right)^{-0.13} \quad (5.12)$$

where M_{ch} is a characteristic mass at $z=0$, defined such that $\sigma(M_{\text{ch}}) = 1.686$, where $\sigma(M)$ is the present day smoothed variance of density fluctuations. In the same figure, we also show the NFW profile (with concentration parameter from Duffy et al., 2008), which describes the radial distribution of the dark matter. Due to the high concentration of the AGNs, the radial distribution profile of the AGNs appears steeper than the NFW profile.

Our calculation of the 2-halo term does not take into account the effect of scale dependent bias. Also, if the separation between two objects is less than the sum of the virial radii of their host haloes, they should not be counted in the 2-halo term. We neglect this effect which results in the overestimation of the 2-halo term at the scale corresponding to the virial radius of the host halo. However, these corrections are expected to be significant only at small scales (\sim virial size of the object), where 1-halo term becomes more important. Therefore, neglecting this effect is not expected to make much difference to our analysis. These corrections are described in detail in Tinker et al. (2005), Zheng et al. (2009), and van den Bosch et al. (2013) for the real space correlation function.

We use the mean occupation function (MOF) i.e. the number of AGNs ($\langle N(M) \rangle$) residing in a halo of mass M from R13, where the authors use the measurement of 2PCF of X-ray selected AGNs by Allevato et al. (2011) to determine the HOD parameters.

$$\langle N(M) \rangle = \frac{1}{2} \left[1 + \text{erf} \left(\frac{\log M - \log M_{\text{min}}}{\sigma_{\log M}} \right) \right] + \left(\frac{M}{M_1} \right)^\alpha \exp \left(-\frac{M_{\text{cut}}}{M} \right) \quad (5.13)$$

where erf is the error function, M_{min} , $\sigma_{\log M}$, M_1 , α and M_{cut} are the model parameters and their values are shown in Table 5.2. The first part of Equation 5.13 represents the central AGN contribution, $\langle N_c(M) \rangle$ and the second part represents the satellite contribution, $\langle N_s(M) \rangle$. At low halo masses ($M_h < 10^{13.5} h^{-1} M_\odot$), the MOF is dominated by the central AGNs, whereas, at high masses ($M_h > 10^{13.5} h^{-1} M_\odot$), the satellite component takes over. In the high mass regime, the number of satellite AGNs is approximately $\propto M^{5/2}$.

In Figure 5.4, we show the mean number density of AGNs calculated using the MOF from R13 ($\bar{n}_{\text{AGN}} = \int dM \langle N(M) \rangle \frac{dn}{dM}$) and the XLF from A15 ($\bar{n}_{\text{AGN}} = \int d \log L_X \phi_{\text{AGN}}(L_X)$) as a function of redshift, confirming that there is a good agreement between the two approaches, especially in the redshift range 0.5-3. Note that we choose the HOD model by R13 over other models for the X-ray AGNs (Miyaji et al., 2011; Allevato et al., 2012) as the X-ray AGN sample used by R13 span a much wider redshift range compared to that by Miyaji et al. (2011) ($0.16 < z < 0.36$) and Allevato et al. (2012) ($z \lesssim 1$) and is thus easier to use with the luminosity function considered in this chapter.

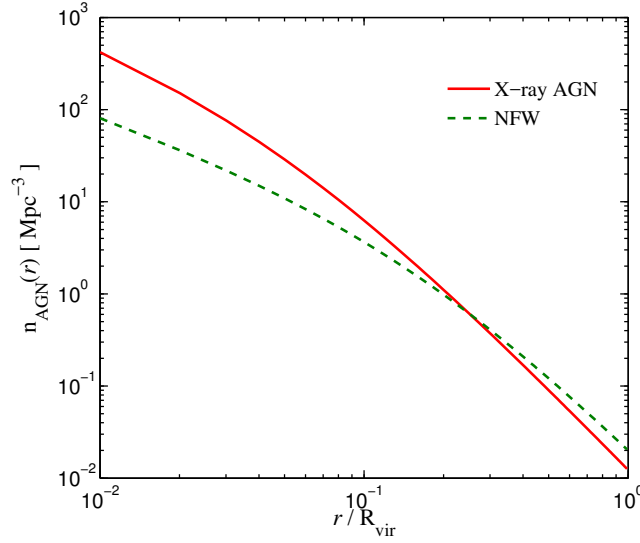


Fig. 5.3 The normalized radial distribution of the X-ray AGNs (solid red line) with concentration parameter given by Equation 5.12, compared with the NFW profile (dashed green line) with concentration parameter from Duffy et al. (2008), for a halo mass $M_h = 10^{14} h^{-1} M_\odot$ at $z = 0$.

Table 5.2 Parameters of MOF.

Parameter	Best fit value
$\log(M_{\min}/h^{-1}M_\odot)$	13.65
$\sigma_{\log M}$	0.78
$\log(M_1/h^{-1}M_\odot)$	14.32
α	2.59
$\log(M_{\text{cut}}/h^{-1}M_\odot)$	11.0

1-halo clustering term

The contribution of the clustering term to the AGN angular auto-correlation power spectrum due to the correlation between AGNs residing in the same halo can be obtained by replacing $P_{\text{AGN}}^{2h}(k)$ by $P_{\text{AGN}}^{1h}(k)$ in Equation 5.8, with

$$P_{\text{AGN}}^{1h}(k) = \int dM \frac{dn}{dM} \frac{\langle N(M)(N(M) - 1) \rangle}{\bar{n}_{\text{AGN}}^2} f_{\text{AGN}}^2(k) \quad (5.14)$$

Equation 5.14 assumes that all AGNs residing in a halo follow the same radial profile (Mo, Mao & White, 1998). However, the central AGN is located near the centre of the halo and the satellite AGNs are assumed to follow the radial distribution shown Figure 5.3.

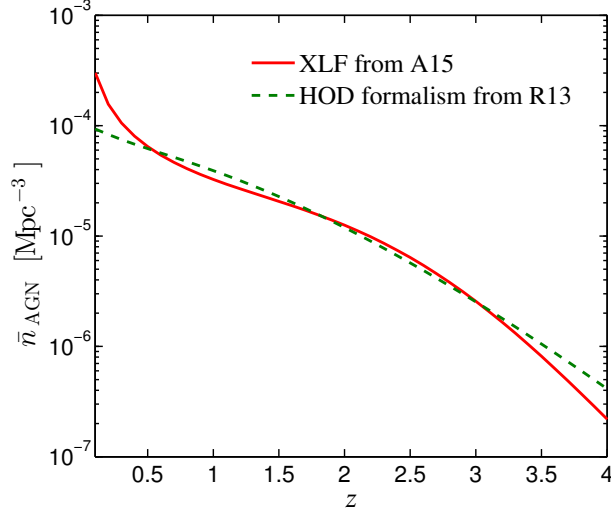


Fig. 5.4 Comparison between the X-ray AGN number density in the soft band as a function of redshift estimated using the XLF from A15 (solid red line) and the HOD formalism from R13 (dashed green line).

Taking into account the different distributions of central and satellite AGNs we get

$$P_{\text{AGN}}^{1h}(k) = P_{\text{AGN}}^{1h,ss}(k) + P_{\text{AGN}}^{1h,cs}(k) \quad (5.15)$$

where $P_{\text{AGN}}^{1h,ss}(k)$ and $P_{\text{AGN}}^{1h,cs}(k)$ are the terms due to satellite-satellite and central-satellite correlation*, respectively.

$$P_{\text{AGN}}^{1h,ss}(k) = \int dM \frac{dn}{dM} \frac{\langle N_s(M) \rangle^2}{\bar{n}_{\text{AGN}}^2} f_{\text{AGN}}^2(k) \quad (5.16)$$

$$P_{\text{AGN}}^{1h,cs}(k) = \int dM \frac{dn}{dM} \frac{2\langle N_c(M) \rangle \langle N_s(M) \rangle}{\bar{n}_{\text{AGN}}^2} f_{\text{AGN}}(k) \quad (5.17)$$

Here we have assumed that the satellites follow Poisson distribution for which $\langle N_s(M)(N_s(M) - 1) \rangle = \langle N_s(M) \rangle^2$.

In Figure 5.5, we show the number weighted auto-correlation power spectrum of X-ray AGNs. At large l -values ($l > 1000$) i.e. small scales, the Poisson term dominates the total power spectrum. However, at small l -values ($l < 1000$) i.e. large angular scales, the clustering is larger than the Poisson term. Within the clustering term, the 1-halo term is always greater than the 2-halo term. Both, the 1-halo and the 2-halo terms increase with increasing l , till $l \sim 500$, beyond which the 2-halo term decreases and the 1-halo term

*There is a typo in equation-10 of Miyaji et al. (2011). The first term of the integrand should be $2 \langle N_c N_s \rangle$.

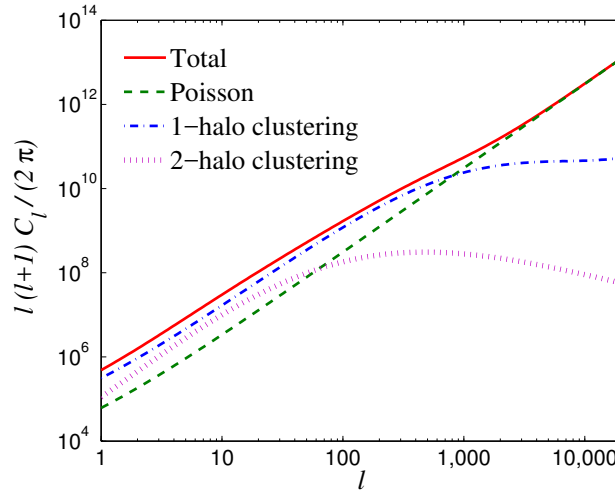


Fig. 5.5 The total power spectrum (solid red line), Poisson term (dashed green line), 1-halo (dot-dashed blue line) and 2-halo (dotted magenta line) clustering terms due to the resolved AGNs in the soft band.

continues to increase till $l \sim 1000$, remains approximately constant till $l \sim 10000$ and dies down with further increase in l .

5.2.4 Redshift and mass dependence

We show the redshift dependence of the Poisson, 1-halo and 2-halo clustering terms of the AGN auto-correlation power spectrum in Figure 5.6. Since, the Poisson term is essentially the number of AGNs, its redshift dependence is identical to the solid red curve in Figure 5.2, with a peak near $z \sim 1.2$. The 1-halo clustering term peaks near $z \sim 0.1$ for $l = 10$. Increasing the value of l does not significantly change the redshift corresponding to the peak. Even at $l = 1000$, the power spectrum peaks at $z \sim 0.25$. Therefore, the 1-halo clustering term is dominated by low redshifts where the radial structure of the haloes can be probed.

In the case of 2-halo clustering term, the power spectrum peaks at $z \sim 0.2, 0.4$ and 1 for $l = 10, 100$ and 1000 , respectively. The 2-halo term, comes from the correlation of two distinct haloes, and so depends on the angular difference between two haloes, and hence smaller angular separation (or higher ℓ -value) peaks at higher z . For the 1-halo, similar to the 2-halo clustering terms, the reason of increasing contribution from high redshift AGN with increasing l value is that the larger l values correspond to smaller angular scales and the distances at higher redshifts appear smaller on the sky.

In Figure 5.7, we show the mass dependence of the AGN clustering terms. The 1-halo term peaks near $2 - 3 \times 10^{15} h^{-1} M_{\odot}$ in the l -range $\sim 10 - 1000$ and the peak shifts only slightly to smaller masses with increasing l as smaller objects contribute more at large l .

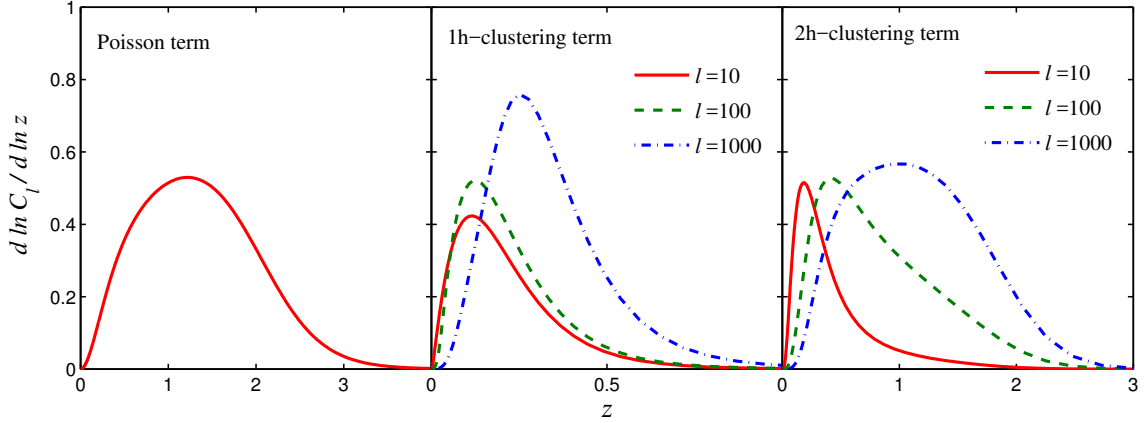


Fig. 5.6 The first, second and third panel show the redshift dependence of the Poisson, 1-halo clustering and 2-halo clustering terms of the resolved AGN auto-correlation power spectrum in the soft band, respectively. In the case of clustering power spectra, $l = 10$, 100 and 1000 is shown by solid red, dashed green and dot-dashed blue lines, respectively.

There is negligible contribution coming from low mass haloes (below $10^{14}h^{-1}M_{\odot}$) to the 1-halo term as expected from the AGN MOF. Massive haloes contribute the most due to the large number of satellite AGNs residing in them. However, we note that the mass dependence of the 1-halo term is really sensitive to the relation between the satellite AGN MOF and the host halo mass. Since, the average number of satellite AGNs increases rapidly with the halo mass ($\langle N_s(M) \rangle \propto M^{2.59}$), most of the contribution to the power spectrum comes from the high mass end of the galaxy population where the number of galactic haloes decreases exponentially. Also, there is a large uncertainty in the determination of α (hence in the determination of $\langle N_s(M) \rangle$), as shown in R13. Therefore, the power spectrum as well as its mass distribution may change significantly with a different value of α .

The 2-halo term shows a prominent double peaked structure in its mass distribution due to the different mass dependencies of central and satellite AGNs. The lower mass peak ($\sim 10^{13}h^{-1}M_{\odot}$) comes from the central AGN contribution, whereas, the higher mass peak ($\sim 10^{15}h^{-1}M_{\odot}$) comes from the satellite AGN contribution to the 2-halo term. The relative strength of these two peaks depend on the l value. For small l values (i.e. large scales) major contribution comes from the massive haloes, whereas, at large l values (i.e. small scales) the low mass haloes rule the 2-halo term. Therefore, at small l , the higher mass peak is more prominent than the smaller mass peak and at large l smaller mass peak overshadows the higher mass peak.

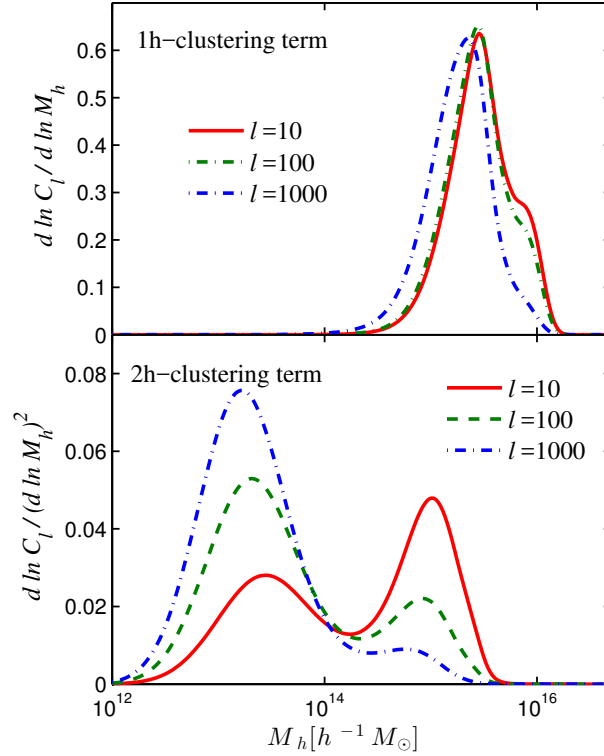


Fig. 5.7 The mass dependence of the 1-halo (left panel) and 2-halo (right panel) clustering terms of the resolved AGN auto-correlation power spectrum in the soft band. The solid red, dashed green and dot-dashed blue lines corresponds to $l = 10$, 100 and 1000, respectively.

5.3 Forecast for constraining HOD parameter using auto-correlation power spectrum

There are the following four free parameters in the AGN HOD model: M_{\min} , $\sigma_{\log M}$, α and M_1 , where M_{\min} is the halo mass at which $\langle N_{\text{cen}} \rangle = 0.5$, $\sigma_{\log M}$ is the width of softened step function used for the central AGN MOF, α is slope of power law relation between the satellite AGN MOF and the halo mass and M_1 is the mass scale at which $\langle N_{\text{sat}} \rangle \approx 1$. The AGN auto-correlation power spectrum can be directly related to the HOD parameters through simple power laws (varying one parameter at a time and keeping all others fixed) in a broad range around the fiducial values of these parameters. For example, C_l has power law dependence on these parameters as follows: $C_l \propto (\log M_{\min})^{1.5}$, $\sigma_{\log M}^{-2}$ and $(\log M_1)^{-4}$ with little to no change in the power law index as a function of l . However, the variation of C_l^{1h} with α cannot be fit by a single power law. The 1-halo term has $\langle N_s(M) \rangle^2$ in its integrand and the satellite MOF itself is proportional to $M^{2.59}$. Consequently, the power spectrum is highly biased towards the massive haloes as discussed in Section 5.2.4. However, varying

the value of α can significantly alter the power spectrum due to the presence of $\langle N_s(M) \rangle^2$ term. Increasing the value of α results in a large increase in the power spectrum causing the sensitive dependence of the power spectrum on the value of α . For $0.5 < \alpha < 1.5$, $C_l^{1h} \propto \alpha^{1.5(1)}$, whereas in the range, $1.5 < \alpha < 3.0$, $C_l^{1h} \propto \alpha^{8.7(6.8)}$, at $l = 10(1000)$.

Similarly, C_l^{2h} is proportional to $(\log M_{\min})^{0.5}$ and $\sigma_{\log M}^{-1}$, and the power law indices are nearly independent of l . However, in the case of $\log M_1$, the power law index depends on the fiducial value of M_1 as well as the value of l . At $l = 10$, near the fiducial value of M_1 , $C_l^{2h} \propto (\log M_1)^{-1.1}$. Analogous to the 1-halo term, the relation between the 2-halo term and α is really sensitive to the value of α as well as l , with $C_l^{2h} \propto \alpha^{0.5(0.3)}$ for $0.5 < \alpha < 2.5$ and $C_l^{2h} \propto \alpha^{2.5(0.6)}$ for $2.5 < \alpha < 3$, at $l = 10(1000)$.

Figure 1b of R13 shows $\langle N_c(M) \rangle$ and $\langle N_s(M) \rangle$ with their $1-\sigma$ uncertainties. There is a large uncertainty in $\langle N_c(M) \rangle$ at low halo masses ($M_h < 10^{12.5} h^{-1} M_\odot$) and in $\langle N_s(M) \rangle$ throughout the entire mass range. This is due to the current large uncertainties in the determination of the model parameters, especially for the satellite AGNs. Also, the X-ray AGN sample (Allevato et al., 2011) used to construct the HOD model in R13 spans a broad redshift range (0-4) with a median redshift, $z_{\text{med}} \sim 1.2$. Therefore, this HOD model represents the AGN population at the median redshift, an average over the redshift range of the AGN sample and it lacks any redshift dependence. Other studies (eg. Koutoulidis et al. 2013; Gatti et al. 2016) involving the X-ray AGN clustering measurement also indicate that the HOD may have a weak redshift dependence. However, it is not possible to put strong constraints due to the small sample sizes. In this section, we look into the possibility of constraining the redshift evolution of the HOD model with upcoming eROSITA all-sky survey (eRASS) using a Fisher matrix analysis.

For simplicity, we consider a power law redshift dependence of the parameters. For the purpose of this study, we choose following Fisher parameters.

$$\left\{ \left\{ \log(M_{\min}), \sigma_{\log M}, \log(M_1), \alpha \right\}, \left\{ \gamma_{M_{\min}}, \gamma_{\sigma_{\log M}}, \gamma_{M_1}, \gamma_\alpha \right\} \right\}, \quad (5.18)$$

where the power law indices γ_a 's are defined as,

$$p_a = p_a^{\text{fid}} \left(\frac{1+z}{1+z_{\text{med}}} \right)^{\gamma_a} \quad (5.19)$$

where, p_a^{fid} 's are the fiducial values of the HOD parameters (specified in Table 5.2) and γ_a 's are the corresponding power law indices. The fiducial values of γ_a 's are zero i.e. no redshift evolution.

The Fisher matrix can be calculated using,

$$F_{ab} = \Sigma_{ll'} \frac{\partial C_\ell}{\partial p_a} (M_{\ell\ell'})^{-1} \frac{\partial C_{\ell'}}{\partial p_b} \delta_{ll'} \quad (5.20)$$

where p_a 's are the model parameters and $M_{\ell\ell'}$ is the covariance matrix which incorporates the uncertainty in the C_l 's. $M_{\ell\ell'}$ is given by,

$$M_{\ell\ell'} = \frac{1}{f_{\text{sky}}} \left[\frac{(C_l + N_l)^2 \delta_{\ell\ell'}}{(l + \frac{1}{2}) \Delta l} \right] \quad (5.21)$$

where f_{sky} is the sky coverage of the survey, N_l is the noise in the power spectrum (we consider AGN shot noise only) and Δl is the l -bin size. For simplicity, we neglect the trispectrum contribution to $M_{\ell\ell'}$ and take $\Delta l = 100$.

We show the forecasted constraints on the parameters in Table 5.3. Note that the no priors, fixed HOD and no redshift evolution cases correspond to no priors on any of the Fisher parameters, no change in the fiducial values of the HOD parameters and no redshift evolution of the HOD parameters, respectively. Using this method we find that the redshift evolution of the HOD parameters can be constrained to $\Delta \gamma_{M_{\min}} \sim 0.2$, $\Delta \gamma_{\sigma_{\log M}} \sim 3$, $\Delta \gamma_{M_1} \sim 0.02$ and $\Delta \gamma_\alpha \sim 0.03$, with eROSITA and fixed HOD parameters. Since, the AGN power spectrum is more sensitive to the satellite AGNs compared to the central AGN, γ_{M_1} and γ_α are better constrained than $\gamma_{M_{\min}}$, $\gamma_{\sigma_{\log M}}$. Similarly, in the absence of any redshift evolution, the HOD parameters can be constrained to $\Delta \log M_{\min} \sim 1.1$, $\Delta \sigma_{\log M} \sim 0.9$, $\Delta \log M_1 \sim 0.16$ and $\Delta \alpha \sim 0.015$. However, the uncertainties on these parameters crucially depend on the prior information of the model parameters. These constraints degrade significantly if the priors on other parameters are removed as shown in Table 5.3 and one cannot obtain any strong constraint in such a situation.

The poor constraints obtained from auto-correlation in the absence of strong priors can be improved by combining the information from different probes of the same parameters. Hence, we compute the cross-correlation power spectrum of X-ray emission from the AGN and the galaxy weak lensing to investigate how this combination can be used to improve the constraints on the HOD parameters.

5.4 Cross-correlating X-ray AGN with lensing

When the light from a background galaxy is bent by a structure along the line-of-sight, the resulting lensing is known as weak gravitational lensing. There are two effects of lensing on the image of a background galaxy: convergence (κ), which represents the isotropic stretch-

ing of the image, and shear (γ), which represents the anisotropic stretching thus distorting a circular image into an elliptical one. In the weak lensing regime both the convergence and shear are small i.e. $\kappa \ll 1$, $\gamma \ll 1$. The convergence field is a direct probe of the gravitational potential of the lens mass and it can be obtained from the measurement of the shear field. For the detailed procedure of measurement of the shear field and construction of convergence maps see eg. Refregier (2003); Kilbinger (2015) and references therein.

Cross-correlation of galaxy lensing with other probes such as SZ effect (Ma et al., 2015; Battaglia, Hill & Murray, 2015), CMB lensing (Hand et al., 2015), has been used to understand baryonic physics as well as to put constraints on the cosmological parameters. Since, the motivation of the HOD formalism is to establish a connection between the AGNs and the host halo, cross-correlating X-ray emission from the AGNs and the lensing signal can provide an additional tool to constrain the HOD model. Therefore, in this section, we estimate the cross-correlation power spectrum of the lensing convergence field with the X-ray emission from AGNs.

5.4.1 X-ray-lensing cross-correlation power spectrum

Analogous to the X-ray auto-correlation power spectrum, the AGN X-ray-lensing cross-correlation power spectrum in the thin lens limit (i.e. the thickness of the lens is much smaller than the distance between the lens and observer as well as the distance between the lens and source) is given by,

$$C_l^{\text{AGN},\kappa} = \int dz \frac{dV}{dzd\Omega} W_{\text{AGN}}(z) W_{\kappa}(z) P_{\text{AGN},\kappa} \left(k = \frac{l}{\chi(z)} \right) \quad (5.22)$$

where $W_{\text{AGN}}(z)$ is given by Equation 5.10. The lensing kernel $W_{\kappa}(z)$ for a flat Universe (Van Waerbeke, Hinshaw & Murray, 2014) is given by,

$$W_{\kappa}(z) = \frac{3}{2} \Omega_M^0 \left(\frac{H_0}{c} \right)^2 g(z) (1+z) / \chi(z) \quad (5.23)$$

Here $g(z)$ is defined as,

$$g(z) = \int_{\chi}^{\chi_H} d\chi' p_s(\chi') \frac{\chi' - \chi}{\chi'} = \int_z^{z_H} dz' p_s(z') \frac{\chi' - \chi}{\chi'} \quad (5.24)$$

where $p_s(z) = n(z)/n(z=0)$ is the normalized source redshift distribution function. Again, the power spectrum can be decomposed into 1-halo and 2-halo terms.

$$P_{\text{AGN},\kappa}(k) = P_{\text{AGN},\kappa}^{1h}(k) + P_{\text{AGN},\kappa}^{2h}(k) \quad (5.25)$$

where,

$$P_{\text{AGN},\kappa}^{1h}(k) = \int dM \frac{dn}{dM} f_{\kappa}(k, M, z) \left[\frac{\langle N_c(M) \rangle + \langle N_s(M) \rangle f_{\text{AGN}}(k, M, z)}{\bar{n}_{\text{AGN}}} \right] \quad (5.26)$$

and

$$P_{\text{AGN},\kappa}^{2h}(k) \approx P_{\text{lin}}(k) \left[\int dM \frac{dn}{dM} b_h(M, Z) f_{\kappa}(k, M, z) \right] \times \left[\int dM \frac{dn}{dM} b_h(M, Z) \frac{\langle N_c(M) \rangle + \langle N_s(M) \rangle f_{\text{AGN}}(k, M, z)}{\bar{n}_{\text{AGN}}} \right] \quad (5.27)$$

where, $f_{\kappa}(k, M, z)$ is the Fourier transform of the dark matter density profile and its given by,

$$f_{\kappa}(k, M, z) = \int 4\pi r^2 dr \frac{\rho_{\text{DM}}(r)}{\bar{\rho}_M} \frac{\sin(kr)}{kr} \quad (5.28)$$

where $\rho_{\text{DM}}(r)$ is the NFW density profile and $\bar{\rho}_M$ is the comoving matter density of the universe.

We choose the combination of eROSITA and LSST surveys to forecast the constraints on the HOD model that can be obtained from such a study. The reason of this choice is the high sky coverage of the overlapping region of the two surveys. LSST is a ground based optical telescope, presently under construction. We take the sky coverage of the overlapping region between eROSITA and LSST, $f_{\text{sky}} \sim 0.5$, for the calculation of the covariance matrix. In order to calculate the lensing part, we take the source redshift distribution function, $p_s(z) = (z^3/2z_0^3)e^{-z/z_0}$ (Battaglia, Hill & Murray, 2015), where $z_0 = 1/3$ for the LSST survey.

In Figure 5.8, we show the 1-halo, 2-halo and total X-ray AGN-lensing cross-correlation power spectrum. There is an interesting difference between the X-ray auto-correlation power spectrum and the X-ray-lensing cross-correlation power spectrum. In the case of X-ray auto-correlation power spectrum, 2-halo term is always smaller than the 1-halo term. But for the cross-correlation power spectrum, on large scales ($l \lesssim 100$), the 2-halo term is larger than the 1-halo term. This behavior is due to the reason that in the case of galaxy weak lensing auto-correlation power spectrum, the 1-halo term becomes larger than the 2-halo term at comparatively larger multipoles ($l > 100$, see for example Takada & Bridle 2007). As a result, the X-ray-lensing cross-correlation power spectrum shows the transition from 2-halo to 1-halo dominance at intermediate multipoles.

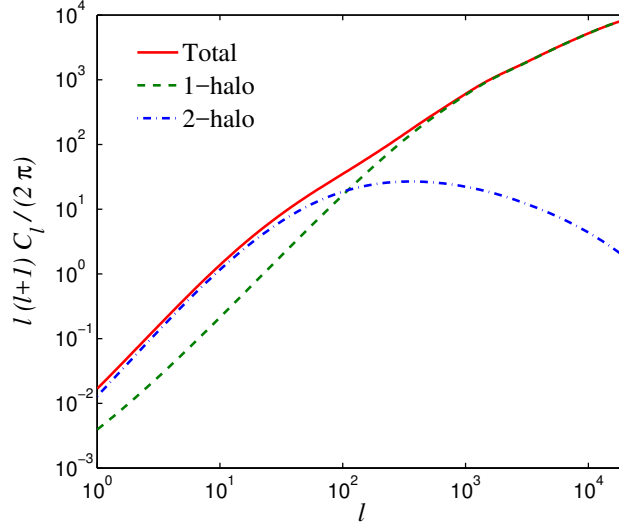


Fig. 5.8 The cross-correlation power spectrum of soft X-ray emission from the AGNs and weak lensing. The total power spectrum, 1-halo and 2-halo terms are indicated by solid red, dashed green and dot-dashed blue lines, respectively.

5.4.2 Forecast using the cross-correlation power spectrum

The uncertainty in the X-ray-lensing cross-correlation power spectrum is given by,

$$M_{ll'}^{\text{AGN},\kappa} = \frac{\delta_{ll'}}{f_{\text{sky}}(2l+1)\Delta l} \times \left[\hat{C}_l^{\text{AGN},\text{AGN}} \hat{C}_l^{\kappa\kappa} + \hat{C}_l^{\text{AGN},\kappa} \hat{C}_l^{\text{AGN},\kappa} \right] \quad (5.29)$$

where, \hat{C}_l^{ij} 's are the auto ($i = j$) or cross ($i \neq j$) power spectra including noise. We consider only the shot noise term to calculate the noise in the X-ray auto-correlation power spectrum, as mentioned in Section 5.3. Noise in the lensing auto-correlation power spectrum is, $N_l^{\kappa\kappa} = \sigma_\gamma^2/n_s$ (Battaglia, Hill & Murray, 2015), where, σ_γ and n_s are the intrinsic ellipticity dispersion per component and the 2-dimensional angular number density of the source galaxies, respectively. For LSST, $\sigma_\gamma^2 = 0.28$ and $n_s = 40 \text{ arcmin}^{-2}$. Assuming that the noise in X-ray and lensing surveys are independent of each other, $N_l^{\text{AGN},\kappa} = 0$.

We choose $\gamma_{M_{\min}}$ and γ_α which represent the central and satellite AGNs, respectively, and show the individual as well as the joint constraints on $\gamma_{M_{\min}}$ and γ_α coming from the auto and cross-correlation power spectra in Figure 5.9. Note that, to examine how well these spectra combinations can constrain the model parameters, we do not put any priors on any of the Fisher parameters. The X-ray-lensing cross-correlation analysis can alone constrain $\gamma_{M_{\min}}$ and γ_α to approximately, 0.5 and 0.9, respectively. The uncertainty on $\gamma_{M_{\min}}$ is much better for the cross correlation signal compared to the auto-correlation signal, whereas, the uncertainty on γ_α is similar for the two cases. The reason of the loose constraint on $\gamma_{M_{\min}}$ as

Table 5.3 Forecasted constraints on the HOD parameters with eROSITA and eROSITA-LSST combination.

	Power spectrum	$\Delta \log(M_{\min})$	$\Delta \sigma_{\log M}$	$\Delta \log(M_1)$	$\Delta \alpha$	$\Delta \gamma_{M_{\min}}$	$\Delta \gamma_{\sigma_{\log M}}$	$\Delta \gamma_{M_1}$	$\Delta \gamma_{\alpha}$
No priors {	X-ray auto	35	23	6	3	6	75	1	1
	X-ray-lensing cross	2.5	1.5	1	1.2	0.5	5.7	0.16	0.9
	Auto+Cross	0.6	0.3	0.17	0.13	0.1	0.9	0.02	0.07
Fixed HOD {	X-ray auto	-	-	-	-	0.2	3	0.02	0.03
	X-ray-lensing cross	-	-	-	-	0.1	1	0.03	0.11
	Auto+Cross	-	-	-	-	0.02	0.2	0.004	0.008
No redshift evolution {	X-ray auto	1.1	0.9	0.16	0.015	-	-	-	-
	X-ray-lensing cross	0.4	0.2	0.13	0.13	-	-	-	-
	Auto+Cross	0.1	0.06	0.02	0.01	-	-	-	-

compared to γ_{α} coming from the X-ray auto-correlation power spectrum is that the X-ray auto-correlation power spectrum is much more sensitive to the satellite AGN MOF, hence γ_{α} in comparison to the central AGN MOF, hence $\gamma_{M_{\min}}$ (see Equation 5.16 and 5.17). On the contrary, the X-ray-lensing cross-correlation power spectrum has similar dependence on the central as well as satellite AGN MOF (see Equation 5.26), resulting in similar constraints on the corresponding Fisher parameters. In addition, this difference in dependence of the auto and cross-correlation power spectra on the central and satellite terms give rise to distinct directions of degeneracy in $\gamma_{M_{\min}}$ and γ_{α} uncertainty contours, as shown in Figure 5.9. Consequently, the constraints obtained by combining the X-ray auto and X-ray-lensing cross-correlation power spectra Fisher matrices are much better than their individual constraints. The constraints obtained from the combined as well as individual Fisher matrices are shown in Table 5.3.

5.5 Unresolved AGNs

Depending on the flux limit of the X-ray survey, a fraction of AGNs may remain unresolved in the X-ray map. These unresolved X-ray AGNs are the prime source of contamination while studying the diffuse X-ray emission from the hot gas in the ICM and CGM. Therefore, modelling the unresolved AGNs appropriately is essential to extract the X-ray emission from the hot gas and hence the gas physics. In this section, we estimate the flux weighted angular power spectrum, the redshift and halo mass dependence of the power spectrum for the unresolved AGNs, assuming that these AGNs are also described by the same luminosity

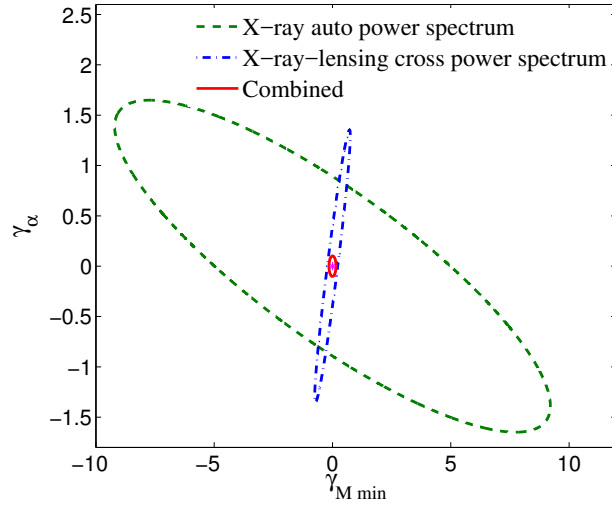


Fig. 5.9 The forecasted 68% confidence limit contours for the redshift evolution parameters of the HOD model, $\gamma_{M \min}$ and γ_{α} . The dashed green and dot-dashed blue contours correspond to the constraints due to the X-ray AGN auto and X-ray AGN-galaxy lensing cross-correlation power spectra in the soft band, respectively, whereas, the solid red contour corresponds to the combined auto and cross-correlation power spectra constraints.

function and the HOD model. The reason for the choice of flux weighted power spectrum is that it is not possible to identify the source of these X-ray photons as their hosts are not resolved by the X-ray telescope which rules out the number weighted power spectrum.

5.5.1 Flux weighted angular auto-correlation power spectrum

As mentioned in Section 5.2, the estimator of unresolved AGN power spectrum is given by Equation 5.1, where, the signal $x(\theta, \phi)$ is the unresolved X-ray flux. Analogous to the resolved AGNs, the flux weighted power spectrum of the unresolved AGNs is the sum of Poisson and clustering terms. The Poisson term is given by,

$$C_P^{\text{AGN}} = \int dz \frac{dV}{dz d\Omega} \int d \log L_X \phi_{\text{AGN}}(L_X, z) S_X^2 \quad (5.30)$$

In contrast to the resolved AGN, the lower luminosity limit in the above integral is set to zero and the upper luminosity limit is fixed by the sensitivity limit of the X-ray telescope for the unresolved AGN.

Again, the clustering term is composed of 1-halo and 2-halo terms given by Equation 5.14 and 5.9, respectively, with $W^{\text{AGN}}(z)$ replaced by,

$$W^{\text{AGN}}(z) = \int d \log L_X \phi_{\text{AGN}}(L_X) S_X \quad (5.31)$$

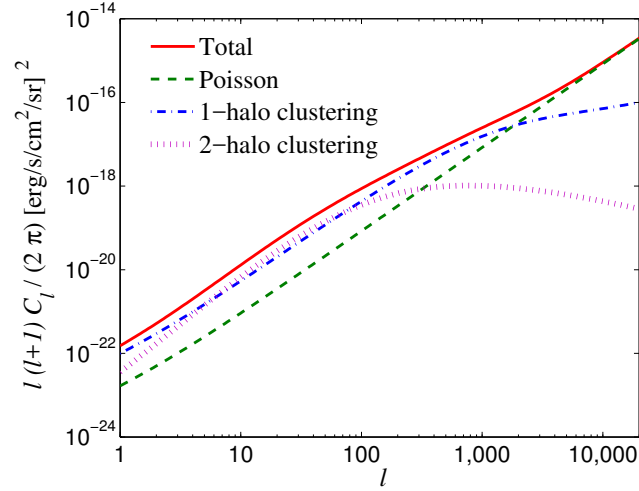


Fig. 5.10 Same as Figure 5.5 but for the unresolved AGNs.

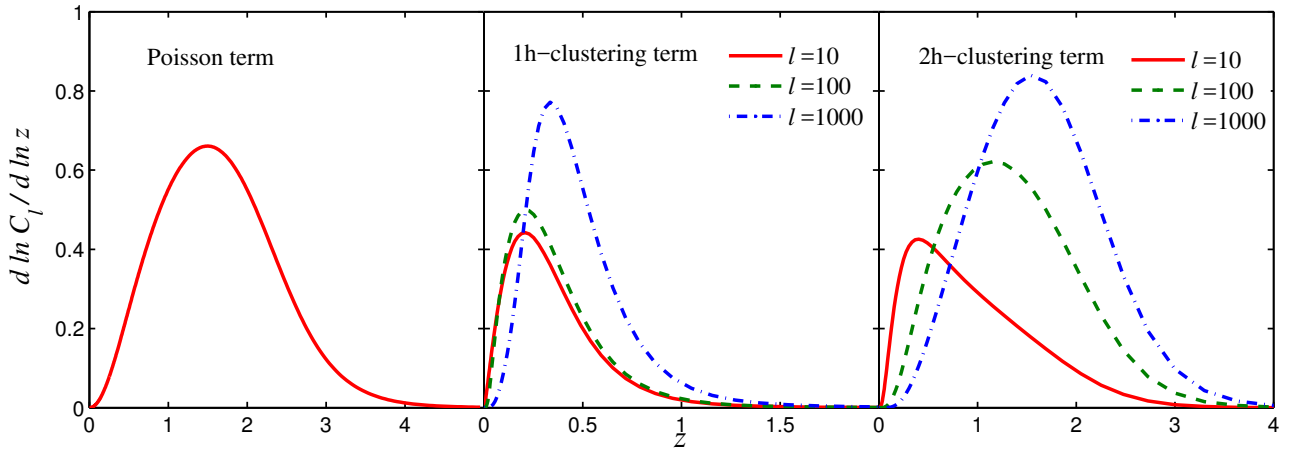


Fig. 5.11 Same as Figure 5.6 but for the unresolved AGNs.

In Figure 5.10, we show the flux weighted auto-correlation power spectrum for AGNs lying below the flux resolution limit of eROSITA. Similar to the resolved AGNs, at lower multipoles, the clustering term is dominant whereas at large multipoles, the Poisson term takes over the total power spectrum. However, this takes place near $l \sim 2000$ in the case of unresolved AGNs, compared to $l \sim 1000$ for the resolved AGNs. Another visible difference between the resolved and the unresolved AGN power spectrum is that the 2-halo clustering term is always smaller than the 1-halo clustering term for the resolved AGN, whereas, the 2-halo term is slightly larger than 1-halo term in the l -range 10-100 for the unresolved AGNs.

5.5.2 Redshift and mass dependence

In Figure 5.11, we show the redshift dependence of the Poisson, 1-halo clustering and 2-halo clustering power spectra of the unresolved AGNs. The redshift distribution of the unresolved AGN power spectra have small but non-negligible contribution from the higher redshift AGNs compared to the resolved AGNs, with similar shape of the overall distribution. The Poisson term peaks at $z \sim 1.5$. This peak is at slightly higher redshift compared to the redshift distribution of the resolved AGNs (see Figure 5.2) which peaks near $z \sim 1.2$, due to the simple fact that a high redshift AGNs with the same luminosity as a low redshift AGNs, corresponds to a lower flux and hence may remain unresolved depending on the telescope's resolution. For the 1-halo clustering term, the power spectrum peaks near $z \sim 0.2$, for $l \sim 10$ and the peak shifts only slightly to higher redshifts with increasing value of l .

The 2-halo clustering term peaks at $z \sim 0.5$, for $l \sim 10$ and the peak shifts significantly with increasing value of l . For $l \sim 1000$, the 2-halo clustering power spectrum is dominated by $z \sim 1.5$ AGNs. Since, the total power spectrum is controlled by clustering term at $l < 2000$ and Poisson term at $l > 2000$, the overall power spectrum is governed by low to intermediate redshift AGNs ($z \sim 0.2-1.5$).

The mass dependence of the unresolved AGN power spectrum is shown in Figure 5.12. The 1-halo clustering term of the unresolved and resolved AGNs (Figure 5.7) have almost identical halo mass dependence, with a peak near $10^{15}h^{-1}M_{\odot}$ due to the highly biased MOF of the satellite AGNs towards massive haloes.

The 2-halo clustering power spectrum also show a double peaked mass distribution similar to the one observed in case of resolved AGNs. However, the low mass peak ($\sim 10^{13}h^{-1}M_{\odot}$) is more prominent than the high mass peak ($\sim 10^{15}h^{-1}M_{\odot}$), even at $l = 10$. At higher l values, most of the contribution to the 2-halo term comes from $10^{12} - 10^{14}h^{-1}M_{\odot}$ haloes.

5.6 Conclusions

In this work, we divided the AGNs into two categories: 1) resolved AGNs, which lie above the flux resolution limit of eROSITA, and 2) unresolved AGNs, lying below this limit. We computed the number weighted and flux weighted angular power spectra for the resolved and unresolved AGNs, respectively, in the soft X-ray band. We used the LADE model for the X-ray AGN luminosity function described in A15 (which matches well with the observed AGN number counts) and the HOD model for the X-ray AGNs by R13, which describe the luminosity distribution and halo mass dependence of the AGNs, respectively. We also calculated the luminosity and redshift dependence of the resolved AGNs finding

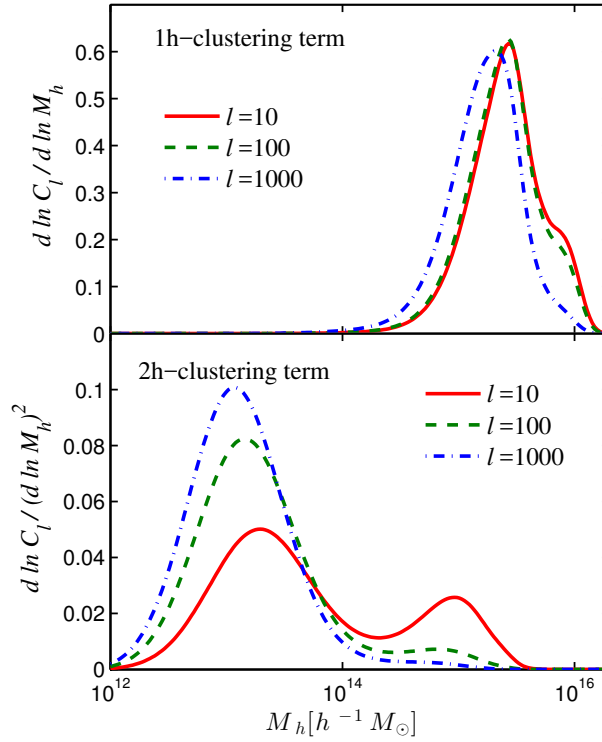


Fig. 5.12 Same as Figure 5.7 but for the unresolved AGNs.

that the maximum contribution to the AGN luminosity and redshift distribution comes from $L_X \sim 2 - 3 \times 10^{44} \text{ erg s}^{-1}$ and $z \sim 1.2$, respectively. We computed the number density of the X-ray AGNs using the XLF as well as the HOD formalism and found that the two approaches are in good agreement with each other in a wide range of redshift (especially at $0.5 \lesssim z \lesssim 3.5$). The X-ray auto-correlation power spectrum has the following features.

1. The power spectrum of the resolved AGNs is dominated by low redshift AGNs ($z \sim 0.1 - 0.2$) at low multipoles ($l < 1000$) due to the dominant contribution from the 1-halo clustering term at these multipoles. However, at large multipoles ($l > 1000$), where the Poisson term controls the total power spectrum, the redshift dependence of the power spectrum peaks at intermediate redshifts ($z \sim 1.2$). The 1-halo term is larger than the 2-halo term down to $l = 1$, though at low multipoles these two terms have similar amplitudes.
2. For the unresolved AGNs, the power spectrum is dominated by Poisson term and hence $z \sim 1.5$ AGNs at $l > 2000$. In the range $l \sim 100 - 2000$, where the 1-halo clustering term is dominant, the total power spectrum is governed by $z \sim 0.2 - 0.3$ AGNs. At $l < 100$, the power spectrum has major contribution from $z < 1$ AGNs due to significant contribution from 2-halo as well as the 1-halo clustering terms.

3. The HOD model that we use in this work predicts a large number of satellite AGNs in massive haloes. This mass dependence shows up in the mass dependence of the AGN power spectrum (resolved as well as unresolved). Both the 1-halo and 2-halo terms show peaks at the high mass end ($M_h \sim 10^{15} h^{-1} M_\odot$) of the DMH. Interestingly, the 2-halo term shows an additional peak at lower halo mass ($M_h \sim 10^{13} h^{-1} M_\odot$), which is due to the contribution from the central AGN. The low mass peak becomes more prominent than the high mass peak at large multipoles i.e. small angular scales, especially in the case of unresolved AGNs.

We also investigated the role of eROSITA in constraining the redshift evolution of the HOD parameters, which play a crucial role in determining the AGN power spectrum, using the Fisher matrix analysis. We assumed a simple power law dependence of the HOD parameters on the redshift and found that the uncertainties in the determination of these power law indices vary significantly with and without any priors on other HOD parameters. Without any priors, the X-ray auto-correlation power spectrum poorly constrains these parameters (shown in Table 5.3). To improve upon this, we included X-ray-lensing cross-correlation power spectrum, which is motivated by the fact that lensing traces the total halo mass and that the HOD model describes the relation between the host halo mass and AGNs. The cross-correlation power spectrum can alone put much better constraints on the model parameters (except for the satellite AGN parameters in some situations) and combining the auto and cross-correlation power spectra improves the uncertainties further. For example, γ_{M_1} , which describes the redshift evolution of the relation between the satellite AGN MOF and the host halo mass, can be constrained to $\Delta\gamma_{M_1} \sim 1$ and 0.16, using the X-ray auto and X-ray-lensing cross-correlation power spectra, respectively, and the constraint improves to $\Delta\gamma_{M_1} \sim 0.02$ with the auto and cross-correlation power spectra combination, without any prior information on any other parameter. Adding prior information on the Fisher parameters can significantly reduce their uncertainties. The uncertainty on γ_{M_1} coming from the X-ray auto-correlation power spectrum only, reduces to $\Delta\gamma_{M_1} \sim 0.03$, if the uncertainties on the fiducial values of the HOD model parameters are reduced to zero. Other parameters also follow the same trend depending on the sensitivity of the power spectrum considered, with respect to the parameter.

Our power spectrum analysis suggest that the present constraints on the AGN HOD parameters will improve significantly with the availability of eROSITA and LSST. At the same time, due to the potential of eROSITA to probe the hot gas in galaxies, such an analysis is expected to play a crucial role in separating the contribution from the AGNs and the hot gas.

Chapter 6

Conclusion

In this thesis, we have focused on different potential probes of the CGM to constrain its properties such as the baryon fraction locked up in the CGM, its density, temperature and redshift evolution. The probes we have considered are the tSZ effect, the kSZ effect and X-ray emission. We have explored the cross-correlation of tSZ and X-ray emission with the distribution of galaxies and showed them to be powerful tracers of the CGM. One of the main foci of this thesis is forecasting the detectability of these probes for presently operational state-of-the-art surveys and upcoming missions. We have considered SPT in radio, eROSITA in X-ray and DES and LSST surveys in optical for our work. We have also investigated the role of the CGM in the suppression of galactic outflows. We compared the relative importance of infall and CGM in suppressing outflows which is crucial to determine the fate of metal enrichment history of the Universe. Additionally, we have worked on the theoretical modelling of the X-ray AGN power spectrum, the prime source of contamination in X-ray maps, examining the main ingredients of the halo model and various components of the power spectra. We summarize the main results of this thesis below and conclude with a brief overview of future research plans.

Circumgalactic contribution to the CMB distortion

In chapter-2, we have computed the thermal and kinetic SZ effect from hot CGM hosted by massive haloes. The driving force behind this study is the detection of a significant amount of warm-hot gaseous corona occupying the galactic halo in massive spiral galaxies. To identify the haloes retaining their hot CGM, we have compared the gas cooling time-scale (t_{cool}) with the halo destruction time-scale (t_{dest}), finding that galaxies with mass $\gtrsim 10^{12.5} M_{\odot}$ have $t_{\text{cool}} > t_{\text{dest}}$, thus contributing to the SZ effect.

We have estimated the tSZ and kSZ auto power spectra from these massive galaxies. To calculate these power spectra, we assumed that the CGM contains $\sim 10\%$ of the total halo mass, is at the virial temperature of the galactic halo and is moving with the peculiar velocity of the halo. Our results suggest that the kSZ power spectrum is larger than the tSZ power spectrum for the CGM. We have shown that the kSZ power spectrum due to the CGM can be larger than the tSZ power spectrum for galaxy clusters at large multipoles, $l > 10^4$. We have compared our estimates of the integrated Comptonization parameter Y_{500} with the measurements by Planck Collaboration et al. (2013) finding that the two are consistent with each other in the mass range of interest. Our prediction of the integrated tSZ distortion from warm CGM is above the detection limit of near future mission, *PIXIE*. We have found that the tSZ and kSZ power spectra can be easily detected by a cosmic variance limited survey, whereas, marginal detection is possible with a simple extension of the SPT survey. Using the Fisher matrix analysis, we have shown that a cosmic variance limited survey can constrain the gas fraction to percent level, whereas, the extended version of the SPT survey can constrain the gas fraction to $\sim 33\%$. Our results indicate that if the CGM contains approximately $\sim 10\%$ of the total halo mass, then the power spectra considered in our work can be detected with sufficient precision.

Probing the circumgalactic baryons through cross-correlation of tSZ/X-ray signals with the distribution of galaxies

In Chapter 3, we have investigated the cross-correlation prospects of the tSZ effect, soft (0.5-2 keV) X-ray emission from the CGM, and the distribution of galaxies. Both, the tSZ-galaxy distribution and X-ray-galaxy distribution cross power spectra are significant at small l values ($\gtrsim 3000$). To probe the effect of variation in the gas density profile on the cross power spectra, we parameterized the CGM density as $\rho \propto [1 + (r/R_s)^{\gamma_{\text{gas}}}]$, and found that the tSZ-galaxy distribution cross power spectrum increases at $l > 3000$ with increasing value of γ_{gas} (i.e. steepening of the density profile). The increase in the X-ray-galaxy distribution cross power spectrum is much more (than the tSZ-galaxy cross power spectra) even at low l values which is due the difference in sensitivity of X-ray emission ($\propto \rho^2$) and the tSZ effect ($\propto \rho$) on the gas density.

We have forecasted the detectability of these cross-power spectra from the survey combinations, SPT-DES for tSZ-galaxy, eROSITA-DES/LSST for X-ray-galaxy and SPT-eROSITA for tSZ-X-ray cross power spectra. The forecasted detectabilities of tSZ-galaxy and X-ray-galaxy cross power spectra are sufficient ($\text{SNR} > 3$), whereas, its low ($\text{SNR} < 1$) tSZ-X-ray cross power spectrum. The cumulative SNR peaks for massive, intermediate redshift galax-

ies. We then performed Fisher matrix analysis to constrain the CGM fraction, temperature, slope of gas density profile, finding that the X-ray-galaxy cross power spectrum is more useful in this regard than the tSZ-galaxy cross power spectrum. Comparison of these constraints with the predictions of the CGM density profile by recent hydrodynamical simulations (Le Brun, McCarthy & Melin, 2015; Suresh et al., 2015) indicates that the cross-correlation of tSZ/X-ray with galaxy distribution has the potential to differentiate between different feedback scenarios as the resultant CGM distribution varies significantly for different feedback mechanisms.

Suppression of galactic outflows by cosmological infall versus CGM

In Chapter 4, we have followed a simplified approach to combine the results of N-body, gravity-only simulations and analytical formalism for galactic outflows, neglecting the complexities involved in the distribution and energetics of the CGM, to study the relative importance of hot CGM and cosmological infall in suppressing outflows as well as their role in the enrichment of the galaxy and IGM. To compute the infall velocity, we have considered radial motions only. We have found that, in the absence of the CGM, the infall reduces the net speed of the outflowing gas and even halts it, especially for massive galaxies at higher redshifts. The upper mass limit beyond which outflows cannot escape the gravitational field of the galaxy decreases by a factor of two due to cosmological infall in star forming galaxies. We have already shown in Chapter 2 that massive galaxies ($\gtrsim \text{few} \times 10^{11} - 10^{12} M_{\odot}$) can retain their hot circumgalactic environment. The existence of hot CGM also suppresses outflows. At the same time, it also interferes with infalling gas thus forming a barrier between ISM and IGM. This mass limit is also in agreement with the mass range ($10^{11} - 10^{12} M_{\odot}$) estimated by Gabor & Davé (2015), above which infall is quenched. There are other observations and simulations as well (Mathes et al., 2014; Goerdt & Ceverino, 2015), where the difference in behaviour of outflows as well as infall in low mass ($M_h \lesssim 10^{12} M_{\odot}$) and massive galaxies ($M_h \gtrsim 10^{12} M_{\odot}$) can be explained by the presence of hot CGM in massive galaxies. Further, we have shown that infall is more effective in suppressing outflows at high redshifts ($z \gtrsim 3.5$), whereas, hot CGM dominates the suppression at low redshifts ($z \lesssim 3.5$).

Since, galactic outflows are responsible for the carrying metals from the innermost regions of galaxies to the IGM, understanding their suppression is important to understand the metal enrichment history of the Universe. Comparing our prediction of upper mass limit (beyond which outflows are suppressed) with the characteristic mass, we have shown that the fraction of galaxies with unsuppressed outflows decreases $\sim 90\%$ to 50% from redshift ~ 5 to 0. It is interesting to note that this fraction is close to $60\text{-}70\%$ in redshift range $z \sim 1 - 2$,

which coincides with the era of high star formation, and hence high metal production and feedback activities. Therefore, the suppression mechanisms discussed in this chapter are crucial to a complete picture of galaxy formation and evolution.

Constraints on the X-ray AGN HOD and the potential role of eROSITA

In Chapter 3, we have demonstrated the potential role of the X-ray-galaxy cross power spectra in understanding CGM properties, especially the density profile of the gas. However, AGNs dominate the extragalactic X-ray sky, making it difficult to extract X-ray signals from other components. Therefore, it is essential to model the AGN component of the power spectrum to obtain the hot gas component. In Chapter 5, we have constructed a detailed halo model dealing with various components of resolved as well as unresolved X-ray AGNs. For this, we combined the XLF and HOD model of the X-ray AGNs, which are the two prime inputs to calculate AGN power spectrum. We have focused on the soft band (0.5-2 keV) of eROSITA. We have shown that AGN XLF and HOD are in agreement with each other, especially in the redshift range $\sim 0.5 - 3.5$. In the case of resolved AGNs, the power spectrum is dominated by the Poisson term at $l > 1000$, and by the one-halo term at $l < 1000$, whereas, for unresolved AGNs, the two-halo term dominates at $l < 100$, with the one-halo and Poisson terms dominating at $l \sim 100 - 2000$ and $l > 2000$, respectively. We have presented the redshift and mass dependence of all these components in detail.

The knowledge of HOD model parameters is crucial to determine the AGN power spectrum. However, the uncertainty estimates at present do not constrain the power spectrum well, mostly due to the small sample size of X-ray AGNs. Therefore, we investigated the potential of eROSITA to improve these constraints. The results of our Fisher matrix analysis suggest that the AGN X-ray auto power spectrum cannot put meaningful constraints on these parameters without any priors on the HOD model parameters. Fortunately, the inclusion of weak lensing in the power spectrum analysis improves the situation considerably. The forecasted uncertainties in the HOD model parameters decrease by an order of magnitude by including the X-ray-lensing cross power spectrum for eROSITA-LSST survey combination.

Future prospects

Our work on different probes (kSZ, tSZ, X-ray emission and galaxy distribution) of the CGM shows that ongoing and upcoming surveys such as SPT, DES, eROSITA have the capability to uncover the nature of the CGM, which is essential to galaxy evolution. The combination of different probes is helpful in breaking degeneracies in model parameters, giving strong constraints on the underlying system. Therefore, one of the main future direc-

tions for me is to bring in other observables (eg. weak lensing, measurements of hot halo properties of the MilkyWay) in the cross-correlation picture to improve our understanding of the CGM.

I am also planning to work on the measurement of these cross-correlation signals with currently available datasets. I am especially interested in working on the measurement of the X-ray-galaxy cross power spectrum using ROSAT (which was the last all-sky X-ray survey with mean point spread function 3 arcmin) and SDSS survey combination. This survey combination provides a large overlapping region in the sky ($f_{\text{sky}} \sim 25\%$). ROSAT-SDSS survey combination is an attractive choice as it has not been used to examine the X-ray-galaxy cross power spectrum. This survey combination will allow us to explore smaller systems such as galaxies as well as one of the largest astrophysical systems such as clusters of galaxies. Therefore, it can provide new insights into the current understanding of the properties of hot gas.

A byproduct of my work on the CGM is the detailed halo model for X-ray AGNs. Since I have already worked on the theoretical analysis of cross-correlation of X-ray-optical signals for galaxies, I also plan to conduct a similar study for X-ray AGNs, keeping eROSITA in mind. Currently, the small sky coverage of ongoing X-ray surveys limits the clustering measurements of X-ray AGNs to their 2PCF. eROSITA will open up a new window to work with the AGNs in Fourier space with sufficient angular resolution (~ 30 arcseconds whereas the angular resolution of ROSAT is ~ 3 arcminutes). Since, I am planning to work on the X-ray-optical cross-correlation, the next natural step should be using the same survey combination to constrain the AGN HOD. There are a large number of optical surveys scanning different parts of the sky. The data from these surveys will complement the eROSITA catalogue of AGNs. Therefore, to prepare myself for this opportunity, I plan to extend my work on the X-ray AGN power spectrum with the ROSAT-SDSS survey combination.

References

- Abbott T. et al., 2016, *Phys. Rev. D*, 94, 022001
- Addison G. E., Dunkley J., Spergel D. N., 2012, *MNRAS*, 427, 1741
- Aird J., Coil A. L., Georgakakis A., Nandra K., Barro G., Pérez-González P. G., 2015, *MNRAS*, 451, 1892
- Allevato V. et al., 2011, *ApJ*, 736, 99
- Allevato V. et al., 2014, *ApJ*, 796, 4
- Allevato V. et al., 2012, *ApJ*, 758, 47
- Anderson M. E., Bregman J. N., 2010, *ApJ*, 714, 320
- Anderson M. E., Bregman J. N., 2011, *ApJ*, 737, 22
- Anderson M. E., Bregman J. N., Dai X., 2013, *ApJ*, 762, 106
- Anderson M. E., Gaspari M., White S. D. M., Wang W., Dai X., 2015, *MNRAS*, 449, 3806
- Bagla J. S., 2002, *Journal of Astrophysics and Astronomy*, 23, 185
- Bagla J. S., Prasad J., 2006, *MNRAS*, 370, 993
- Barai P. et al., 2013, *MNRAS*, 430, 3213
- Battaglia N., Bond J. R., Pfrommer C., Sievers J. L., Sijacki D., 2010, *ApJ*, 725, 91
- Battaglia N., Hill J. C., Murray N., 2015, *ApJ*, 812, 154
- Behroozi P. S., Wechsler R. H., Conroy C., 2013, *ApJ*, 770, 57
- Bell E. F., McIntosh D. H., Katz N., Weinberg M. D., 2003, *ApJ*, 585, L117
- Benson A. J., Bower R. G., Frenk C. S., White S. D. M., 2000, *MNRAS*, 314, 557
- Bhattacharya S., Kosowsky A., 2008, *Phys. Rev. D*, 77, 083004
- Birnboim Y., Dekel A., 2003, *MNRAS*, 345, 349
- Bogdán Á., Forman W. R., Kraft R. P., Jones C., 2013a, *ApJ*, 772, 98
- Bogdán Á. et al., 2013b, *ApJ*, 772, 97

- Bouché N. et al., 2010, *ApJ*, 718, 1001
- Bower R. G., Benson A. J., Lacey C. G., Baugh C. M., Cole S., Frenk C. S., 2001, *MNRAS*, 325, 497
- Cappelluti N., Ajello M., Burlon D., Krumpke M., Miyaji T., Bonoli S., Greiner J., 2010, *ApJ*, 716, L209
- Cavaliere A., Lapi A., Menci N., 2002, *ApJ*, 581, L1
- Cen R., 2013, *ApJ*, 770, 139
- Cen R., Ostriker J. P., 1999, *ApJ*, 519, L109
- Chaudhuri A., Majumdar S., Nath B. B., 2013, *ApJ*, 776, 84
- Chaudhuri A., Nath B. B., Majumdar S., 2012, *ApJ*, 759, 87
- Chen H.-W., Helsby J. E., Gauthier J.-R., Shectman S. A., Thompson I. B., Tinker J. L., 2010, *ApJ*, 714, 1521
- Cheng L.-M., Wu X.-P., Cooray A., 2004, *A&A*, 413, 65
- Coil A. L. et al., 2009, *ApJ*, 701, 1484
- Cole S., Aragon-Salamanca A., Frenk C. S., Navarro J. F., Zepf S. E., 1994, *MNRAS*, 271, 781
- Cole S., Lacey C. G., Baugh C. M., Frenk C. S., 2000, *MNRAS*, 319, 168
- Copi C. J., Schramm D. N., Turner M. S., 1995, *Science*, 267, 192
- Crain R. A., McCarthy I. G., Frenk C. S., Theuns T., Schaye J., 2010, *MNRAS*, 407, 1403
- Croom S. et al., 2004, in *Astronomical Society of the Pacific Conference Series*, Vol. 311, *AGN Physics with the Sloan Digital Sky Survey*, Richards G. T., Hall P. B., eds., p. 457
- Croton D. J. et al., 2006, *MNRAS*, 365, 11
- Dai X., Anderson M. E., Bregman J. N., Miller J. M., 2012, *ApJ*, 755, 107
- Danforth C. W., Shull J. M., 2005, *ApJ*, 624, 555
- Danovich M., Dekel A., Hahn O., Ceverino D., Primack J., 2015, *MNRAS*, 449, 2087
- Danovich M., Dekel A., Hahn O., Teyssier R., 2012, *MNRAS*, 422, 1732
- Davé R., 2009, in *Astronomical Society of the Pacific Conference Series*, Vol. 419, *Galaxy Evolution: Emerging Insights and Future Challenges*, Jogee S., Marinova I., Hao L., Blanc G. A., eds., p. 347
- Davé R. et al., 2001, *ApJ*, 552, 473
- Davé R., Finlator K., Oppenheimer B. D., 2011, *MNRAS*, 416, 1354

- Davé R., Oppenheimer B. D., 2007, MNRAS, 374, 427
- Davé R., Oppenheimer B. D., Finlator K., 2011, MNRAS, 415, 11
- Davis M., Efstathiou G., Frenk C. S., White S. D. M., 1985, ApJ, 292, 371
- Dekel A., Birnboim Y., 2006, MNRAS, 368, 2
- Dekel A. et al., 2009, Nature, 457, 451
- Dekel A., Sari R., Ceverino D., 2009, ApJ, 703, 785
- Dekel A., Silk J., 1986, ApJ, 303, 39
- Dekel A., Woo J., 2003, MNRAS, 344, 1131
- Diego J. M., Silk J., Sliwa W., 2003, MNRAS, 346, 940
- Duffy A. R., Battye R. A., Davies R. D., Moss A., Wilkinson P. N., 2008, MNRAS, 383, 150
- Durier F., de Freitas Pacheco J. A., 2011, International Journal of Modern Physics E, 20, 44
- Dutton A. A., Conroy C., van den Bosch F. C., Prada F., More S., 2010, MNRAS, 407, 2
- Ebrero J. et al., 2009, A&A, 493, 55
- Efstathiou G., Migliaccio M., 2012, MNRAS, 423, 2492
- Evoli C., Ferrara A., 2011, MNRAS, 413, 2721
- Faerman Y., Sternberg A., McKee C. F., 2017, ApJ, 835, 52
- Fang T., Bullock J., Boylan-Kolchin M., 2013, ApJ, 762, 20
- Fang W., Kadota K., Takada M., 2012, Phys. Rev. D, 85, 023007
- Ferrarese L., Merritt D., 2000, ApJ, 539, L9
- Fielding D., Quataert E., McCourt M., Thompson T. A., 2017, MNRAS, 466, 3810
- Flynn C., Holmberg J., Portinari L., Fuchs B., Jahreiß H., 2006, MNRAS, 372, 1149
- Ford A. B., Oppenheimer B. D., Davé R., Katz N., Kollmeier J. A., Weinberg D. H., 2013, MNRAS, 432, 89
- Ford A. B. et al., 2016, MNRAS, 459, 1745
- Fukugita M., Hogan C. J., Peebles P. J. E., 1998, ApJ, 503, 518
- Fukugita M., Peebles P. J. E., 2004, ApJ, 616, 643
- Fukugita M., Peebles P. J. E., 2006, ApJ, 639, 590
- Gabor J. M., Bournaud F., 2014, MNRAS, 437, L56

- Gabor J. M., Davé R., 2015, MNRAS, 447, 374
- Gatti M., Shankar F., Bouillot V., Menci N., Lamastra A., Hirschmann M., Fiore F., 2016, MNRAS, 456, 1073
- Gatto A., Fraternali F., Read J. I., Marinacci F., Lux H., Walch S., 2013, MNRAS, 433, 2749
- Gilli R. et al., 2005, A&A, 430, 811
- Goerdt T., Ceverino D., 2015, MNRAS, 450, 3359
- Gradshteyn I. S., Ryzhik I. M., 1980, Academic Press, New York
- Greevich J., Putman M. E., 2009, ApJ, 696, 385
- Gunn J. E., Peterson B. A., 1965, ApJ, 142, 1633
- Gupta A., Mathur S., Krongold Y., Nicastro F., Galeazzi M., 2012, ApJ, 756, L8
- Hagihara T., Yao Y., Yamasaki N. Y., Mitsuda K., Wang Q. D., Takei Y., Yoshino T., McCammon D., 2010, PASJ, 62, 723
- Haider M., Steinhauser D., Vogelsberger M., Genel S., Springel V., Torrey P., Hernquist L., 2016, MNRAS, 457, 3024
- Hajian A., Battaglia N., Spergel D. N., Bond J. R., Pfrommer C., Sievers J. L., 2013, J. Cosmology Astropart. Phys., 11, 64
- Hamana T., Kayo I., Yoshida N., Suto Y., Jing Y. P., 2003, MNRAS, 343, 1312
- Hand N. et al., 2012, Physical Review Letters, 109, 041101
- Hand N. et al., 2015, Phys. Rev. D, 91, 062001
- Helgason K., Cappelluti N., Hasinger G., Kashlinsky A., Ricotti M., 2014, ApJ, 785, 38
- Hernández-Monteagudo C., Genova-Santos R., Atrio-Barandela F., 2004, ApJ, 613, L89
- Hernández-Monteagudo C., Macías-Pérez J. F., Tristram M., Désert F.-X., 2006, A&A, 449, 41
- Hinshaw G. et al., 2007, ApJS, 170, 288
- Hivon E., Górski K. M., Netterfield C. B., Crill B. P., Prunet S., Hansen F., 2002, ApJ, 567, 2
- Hurier G., Aghanim N., Douspis M., 2014, A&A, 568, A57
- Hurier G., Douspis M., Aghanim N., Pointecouteau E., Diego J. M., Macias-Perez J. F., 2015, A&A, 576, A90
- Iqbal A., Majumdar S., Nath B. B., Etori S., Eckert D., Malik M. A., 2016, ArXiv e-prints

- Jing Y. P., 1999, *ApJ*, 515, L45
- Johnson S. D., Chen H.-W., Mulchaey J. S., 2015, *MNRAS*, 449, 3263
- Kaasra J. S., Werner N., Herder J. W. A. d., Paerels F. B. S., de Plaa J., Rasmussen A. P., de Vries C. P., 2006, *ApJ*, 652, 189
- Kereš D., Katz N., Weinberg D. H., Davé R., 2005, *MNRAS*, 363, 2
- Khandai N., Bagla J. S., 2009, *Research in Astronomy and Astrophysics*, 9, 861
- Khedekar S., Majumdar S., 2013, *J. Cosmology Astropart. Phys.*, 2, 030
- Khedekar S., Majumdar S., Das S., 2010, *Phys. Rev. D*, 82, 041301
- Kilbinger M., 2015, *Reports on Progress in Physics*, 78, 086901
- Klypin A., Zhao H., Somerville R. S., 2002, *ApJ*, 573, 597
- Kogut A. et al., 2011, *J. Cosmology Astropart. Phys.*, 7, 025
- Kolodzig A., Gilfanov M., Hütsi G., Sunyaev R., 2013a, *A&A*, 558, A90
- Kolodzig A., Gilfanov M., Sunyaev R., Sazonov S., Brusa M., 2013b, *A&A*, 558, A89
- Komatsu E. et al., 2009, *ApJS*, 180, 330
- Komatsu E., Kitayama T., 1999, *ApJ*, 526, L1
- Komatsu E., Seljak U., 2002, *MNRAS*, 336, 1256
- Komatsu E. et al., 2011, *ApJS*, 192, 18
- Kormendy J., Richstone D., 1995, *ARA&A*, 33, 581
- Koutoulidis L., Plionis M., Georgantopoulos I., Fanidakis N., 2013, *MNRAS*, 428, 1382
- Krumpe M., Miyaji T., Coil A. L., Aceves H., 2012, *ApJ*, 746, 1
- La Barbera F., de Carvalho R. R., de la Rosa I. G., Sorrentino G., Gal R. R., Kohl-Moreira J. L., 2009, *AJ*, 137, 3942
- Lacey C., Cole S., 1993, *MNRAS*, 262, 627
- Lacey C., Cole S., 1994, *MNRAS*, 271, 676
- Lan T.-W., Ménard B., Zhu G., 2014, *ApJ*, 795, 31
- Le Brun A. M. C., McCarthy I. G., Melin J.-B., 2015, *MNRAS*, 451, 3868
- Leauthaud A. et al., 2015, in *American Astronomical Society Meeting Abstracts*, Vol. 225, *American Astronomical Society Meeting Abstracts*, p. 221.06
- Leauthaud A. et al., 2012, *ApJ*, 744, 159

- Lehner N. et al., 2013, *ApJ*, 770, 138
- LSST Science Collaboration et al., 2009, ArXiv e-prints
- Ma Y.-Z., Van Waerbeke L., Hinshaw G., Hojjati A., Scott D., Zuntz J., 2015, *J. Cosmology Astropart. Phys.*, 9, 46
- Majumdar S., 2001, *ApJ*, 555, L7
- Majumdar S., Mohr J. J., 2003, *ApJ*, 585, 603
- Majumdar S., Mohr J. J., 2004, *ApJ*, 613, 41
- Maller A. H., Bullock J. S., 2004, *MNRAS*, 355, 694
- Marinacci F., Binney J., Fraternali F., Nipoti C., Ciotti L., Londrillo P., 2010, *MNRAS*, 404, 1464
- Mateos S. et al., 2008, *A&A*, 492, 51
- Mathes N. L., Churchill C. W., Kacprzak G. G., Nielsen N. M., Trujillo-Gomez S., Charlton J., Muzahid S., 2014, *ApJ*, 792, 128
- McCarthy I. G., Schaye J., Font A. S., Theuns T., Frenk C. S., Crain R. A., Dalla Vecchia C., 2012, *MNRAS*, 427, 379
- McCarthy I. G. et al., 2010, *MNRAS*, 406, 822
- McNamara B. R., Nulsen P. E. J., 2007, *ARA&A*, 45, 117
- McQuinn M., Werk J. K., 2017, ArXiv e-prints
- Meiksin A., Bolton J. S., Puchwein E., 2017, *MNRAS*, 468, 1893
- Merloni A. et al., 2012, arxiv:1209.3114
- Miller M. J., Bregman J. N., 2015, *ApJ*, 800, 14
- Mitra S., Kulkarni G., Bagla J. S., Yadav J. K., 2011, *Bulletin of the Astronomical Society of India*, 39, 563
- Miyaji T., Hasinger G., Schmidt M., 2000, *A&A*, 353, 25
- Miyaji T., Krumpke M., Coil A. L., Aceves H., 2011, *ApJ*, 726, 83
- Mo H., van den Bosch F. C., White S., 2010, *Galaxy Formation and Evolution*
- Mo H. J., Mao S., White S. D. M., 1998, *MNRAS*, 295, 319
- Molinari D., Gruppuso A., Polenta G., Burigana C., De Rosa A., Natoli P., Finelli F., Paci F., 2014, *MNRAS*, 440, 957
- Moster B. P., Macciò A. V., Somerville R. S., Johansson P. H., Naab T., 2010, *MNRAS*, 403, 1009

- Mountrichas G. et al., 2013, MNRAS, 430, 661
- Muñoz-Cuertas J. C., Macciò A. V., Gottlöber S., Dutton A. A., 2011, MNRAS, 411, 584
- Mulchaey J. S., 2000, ARA&A, 38, 289
- Mulchaey J. S., Mushotzky R. F., Burstein D., Davis D. S., 1996, ApJ, 456, L5
- Navarro J. F., Frenk C. S., White S. D. M., 1997, ApJ, 490, 493
- Nelson D., Genel S., Pillepich A., Vogelsberger M., Springel V., Hernquist L., 2015a, arXiv:1503.02665
- Nelson D., Genel S., Vogelsberger M., Springel V., Sijacki D., Torrey P., Hernquist L., 2015b, MNRAS, 448, 59
- Nelson D., Vogelsberger M., Genel S., Sijacki D., Kereš D., Springel V., Hernquist L., 2013, MNRAS, 429, 3353
- Nicastro F. et al., 2005a, Nature, 433, 495
- Nicastro F. et al., 2005b, ApJ, 629, 700
- Oguri M., Takada M., 2011, Phys. Rev. D, 83, 023008
- Omma H., Binney J., Bryan G., Slyz A., 2004, MNRAS, 348, 1105
- Oppenheimer B. D., Davé R., Kereš D., Fardal M., Katz N., Kollmeier J. A., Weinberg D. H., 2010, MNRAS, 406, 2325
- Planck Collaboration et al., 2014, A&A, 571, A16
- Planck Collaboration et al., 2013, A&A, 557, A52
- Planck Collaboration et al., 2016, A&A, 586, A140
- Planck Collaboration et al., 2015a, arXiv:1502.01589
- Planck Collaboration et al., 2015b, arXiv:1502.01597
- Prochaska J. X. et al., 2017, ApJ, 837, 169
- Puchwein E., Sijacki D., Springel V., 2008, ApJ, 687, L53
- Putman M. E., Peek J. E. G., Joungh M. R., 2012, ARA&A, 50, 491
- Rasmussen A. P., Kahn S. M., Paerels F., Herder J. W. d., Kaastra J., de Vries C., 2007, ApJ, 656, 129
- Rasmussen J., Sommer-Larsen J., Pedersen K., Toft S., Benson A., Bower R. G., Grove L. F., 2009, ApJ, 697, 79
- Read J. I., Trentham N., 2005, Philosophical Transactions of the Royal Society of London Series A, 363

- Rees M. J., Ostriker J. P., 1977, MNRAS, 179, 541
- Refregier A., 2003, ARA&A, 41, 645
- Richardson J., Chatterjee S., Zheng Z., Myers A. D., Hickox R., 2013, ApJ, 774, 143
- Rines K. J., Geller M. J., Diaferio A., Hwang H. S., 2015, arXiv:1507.08289
- Salucci P., Persic M., 1999, MNRAS, 309, 923
- Sarkar K. C., Nath B. B., Sharma P., Shchekinov Y., 2015, MNRAS, 448, 328
- Sharma M., Nath B. B., 2013a, ApJ, 763, 17
- Sharma M., Nath B. B., 2013b, ApJ, 763, 17
- Sharma M., Nath B. B., Chattopadhyay I., Shchekinov Y., 2014a, MNRAS, 441, 431
- Sharma P., McCourt M., Parrish I. J., Quataert E., 2012, MNRAS, 427, 1219
- Sharma P., Roy A., Nath B. B., Shchekinov Y., 2014b, MNRAS, 443, 3463
- Sheth R. K., Diaferio A., 2001, MNRAS, 322, 901
- Sheth R. K., Mo H. J., Tormen G., 2001, MNRAS, 323, 1
- Sheth R. K., Tormen G., 1999, MNRAS, 308, 119
- Shull J. M., 2003, in *Astrophysics and Space Science Library*, Vol. 281, *The IGM/Galaxy Connection. The Distribution of Baryons at z=0*, Rosenberg J. L., Putman M. E., eds., p. 1
- Shull J. M., Danforth C. W., Tilton E. M., 2014, ApJ, 796, 49
- Shull J. M., Smith B. D., Danforth C. W., 2012, ApJ, 759, 23
- Silk J., 1977, ApJ, 211, 638
- Silk J., Mamon G. A., 2012, *Research in Astronomy and Astrophysics*, 12, 917
- Singh P., Nath B. B., Majumdar S., Silk J., 2015, MNRAS, 448, 2384
- Smith B. D., Hallman E. J., Shull J. M., O'Shea B. W., 2011, ApJ, 731, 6
- Sołtan A. M., 2007, A&A, 475, 837
- Somerville R. S., Hopkins P. F., Cox T. J., Robertson B. E., Hernquist L., 2008, MNRAS, 391, 481
- Springel V., Di Matteo T., Hernquist L., 2005, MNRAS, 361, 776
- Stern J., Hennawi J. F., Prochaska J. X., Werk J. K., 2016, ApJ, 830, 87
- Stoche J. T., Keeney B. A., Danforth C. W., Oppenheimer B. D., Pratt C. T., Berlind A. A., 2017, ApJ, 838, 37

- Strickland D. K., Heckman T. M., 2009, *ApJ*, 697, 2030
- Sunyaev R. A., Zeldovich Y. B., 1969, *Nature*, 223, 721
- Suresh J., Bird S., Vogelsberger M., Genel S., Torrey P., Sijacki D., Springel V., Hernquist L., 2015, *MNRAS*, 448, 895
- Sutherland R. S., Dopita M. A., 1993, *ApJS*, 88, 253
- Takada M., Bridle S., 2007, *New Journal of Physics*, 9, 446
- Thom C. et al., 2012, *ApJ*, 758, L41
- Tinker J. L., Weinberg D. H., Zheng Z., Zehavi I., 2005, *ApJ*, 631, 41
- Tripp T. M., Sembach K. R., Bowen D. V., Savage B. D., Jenkins E. B., Lehner N., Richter P., 2008, *ApJS*, 177, 39
- Tumlinson J. et al., 2011, *Science*, 334, 948
- Valageas P., Silk J., 1999, *A&A*, 350, 725
- van den Bosch F. C., More S., Cacciato M., Mo H., Yang X., 2013, *MNRAS*, 430, 725
- Van Waerbeke L., Hinshaw G., Murray N., 2014, *Phys. Rev. D*, 89, 023508
- Vasiliev E. O., Nath B. B., Shchekinov Y., 2015, *MNRAS*, 446, 1703
- Vogelsberger M., Genel S., Sijacki D., Torrey P., Springel V., Hernquist L., 2013, *MNRAS*, 436, 3031
- Walker S. A., Bagchi J., Fabian A. C., 2015, *MNRAS*, 449, 3527
- Wang Q. D. et al., 2005, *ApJ*, 635, 386
- Wang X., Loeb A., 2015, *MNRAS*, 453, 837
- Weinberg D. H., Miralda-Escudé J., Hernquist L., Katz N., 1997, *ApJ*, 490, 564
- Werk J. K. et al., 2014, *ApJ*, 792, 8
- White M. et al., 2012, *MNRAS*, 424, 933
- White S. D. M., Frenk C. S., 1991, *ApJ*, 379, 52
- White S. D. M., Rees M. J., 1978, *MNRAS*, 183, 341
- Yao Y., Shull J. M., Wang Q. D., Cash W., 2012, *ApJ*, 746, 166
- Yao Y., Tripp T. M., Wang Q. D., Danforth C. W., Canizares C. R., Shull J. M., Marshall H. L., Song L., 2009, *ApJ*, 697, 1784
- Zheng Z., Zehavi I., Eisenstein D. J., Weinberg D. H., Jing Y. P., 2009, *ApJ*, 707, 554

